



University of  
Massachusetts  
Amherst

## Computational Analysis of Structural Transformations in Carbon Nanostructures Induced by Hydrogenation

Item Type	dissertation
Authors	Muniz, Andre R
DOI	<a href="https://doi.org/10.7275/2176834">10.7275/2176834</a>
Download date	2024-12-23 15:23:09
Link to Item	<a href="https://hdl.handle.net/20.500.14394/38863">https://hdl.handle.net/20.500.14394/38863</a>

**COMPUTATIONAL ANALYSIS OF STRUCTURAL TRANSFORMATIONS IN  
CARBON NANOSTRUCTURES INDUCED BY HYDROGENATION**

A Dissertation Presented

by

ANDRE R. MUNIZ

Submitted to the Graduate School of the  
University of Massachusetts Amherst in partial fulfillment  
of the requirements for the degree of

DOCTOR OF PHILOSOPHY

May 2011

Department of Chemical Engineering

© Copyright by Andre R. Muniz 2011

All Rights Reserved

**COMPUTATIONAL ANALYSIS OF STRUCTURAL TRANSFORMATIONS IN  
CARBON NANOSTRUCTURES INDUCED BY HYDROGENATION**

A Dissertation Presented

by

ANDRE R. MUNIZ

Approved as to style and content by:

---

Dimitrios Maroudas, Chair

---

David M. Ford, Member

---

Scott M. Auerbach, Member

---

T. J. Mountziaris, Member

---

T. J. Mountziaris, Department Head  
Department of Chemical Engineering

*To Olivia, Jackie and Terezinha*

## ACKNOWLEDGMENTS

I would like to express my gratitude to my advisor Dimitrios Maroudas, for his support and friendship throughout these years at UMass; his continuous guidance was not only of fundamental importance for the development of this thesis, but also for my professional growth. Thanks also to Professors T.J. Mountziaris, David Ford and Scott Auerbach for serving in my committee, and for offering some of the best graduate courses I have had the privilege to attend at UMass. Thanks to colleague Tejinder Singh for the DFT calculations presented in Chapter 5 of this thesis.

Thanks to all the friends I made in Amherst, for making my stay there much more enjoyable and pleasant. I will never forget the good moments we have gone through, and I strongly hope that our paths cross again in the future.

I am deeply grateful to my whole family, in particular to my mother Terezinha, for always supporting me and giving me their love.

Last but not least, I would like to especially thank the ones who bring joy and happiness every day of my life: my wife Jackie, and my daughter Olivia, who was born during the grad school years, and taught me the true meaning of happiness.

Thanks to the Brazilian Federal Agency for the Support and Evaluation of Graduate Education (CAPES), Fulbright Program, and University of Massachusetts for the granted fellowships. The research presented in this thesis was supported by the National Science Foundation under grants No. CBET-0613501 and CMMI-0531171.

## **ABSTRACT**

### COMPUTATIONAL ANALYSIS OF STRUCTURAL TRANSFORMATIONS IN CARBON NANOSTRUCTURES INDUCED BY HYDROGENATION

MAY 2011

ANDRE RODRIGUES MUNIZ

B.E., FEDERAL UNIVERSITY OF RIO GRANDE DO SUL, BRAZIL

M.Sc., FEDERAL UNIVERSITY OF RIO GRANDE DO SUL, BRAZIL

Ph.D., UNIVERSITY OF MASSACHUSETTS AMHERST

Directed by: Professor Dimitrios Maroudas

Carbon nanomaterials, such as carbon nanotubes and graphene, have attracted significant interest over the past several years due to their outstanding and unusual combination of physical properties. These properties can be modified in a controllable way by chemical functionalization in order to enable specific technological applications. One example is hydrogenation, achieved by the exposure of these materials to a source of atomic hydrogen. This process has been considered for hydrogen storage purposes and for the control of the band gap of these materials for applications in carbon-based electronics. Hydrogen atoms are chemisorbed onto the surface of these materials, introducing  $sp^3$ -hybridized C–C bonds in a structure originally formed by delocalized  $sp^2$  C–C bonding. This bonding transition causes severe structural and morphological changes to the graphene layers/walls. Also, it has been demonstrated that the exposure of multi-walled carbon nanotubes (MWCNTs) to a  $H_2$  plasma leads to the formation of diamond nanocrystals embedded within the nanotube walls.

This thesis presents a computational analysis of the effects of hydrogen chemisorption on the structure and morphology of graphene and single-walled carbon nanotubes (SWCNTs), as well as of the different nanostructures that can be generated upon formation of inter-shell and inter-layer  $sp^3$  C–C bonds in MWCNTs and few-layer graphene (FLG), respectively. The analysis is based on a synergistic combination of atomic-scale modeling tools, including first-principles density functional theory (DFT) calculations and classical molecular-dynamics (MD) and Monte Carlo (MC) simulations.

The results demonstrate that SWCNTs and graphene swell upon hydrogenation and provide interpretations to experiments reported in the literature; this swelling depends strongly on the hydrogen surface coverage. A MC/MD-based compositional relaxation procedure generates configurations whose arrangements of H atoms are in excellent agreement with experimental observations. Detailed structural analysis of the hydrogenated surfaces is carried out, providing information which cannot be extracted easily from conventional experimental techniques. The findings of the analysis are used to explain the limitations on the maximum H storage capacity of SWCNT bundles upon their exposure to an atomic H flux. Furthermore, it is demonstrated that the structures resulting from formation of inter-shell or inter-layer C-C bonds are stable and provide seeds for the nucleation of crystalline carbon phases embedded into the shells and layers of the MWCNT and FLG structures, respectively. The key parameter that determines the type and size of the generated nanocrystals is the chiral-angle difference between adjacent layers/walls in the original structure. A novel type of carbon structure, consisting of fullerene-like caged configurations embedded within adjacent graphene layers, has been discovered for the case where the graphene layers are rotated with

respect to each other; interestingly, one class of these structures retains the unique and desired electronic properties of single-layer graphene.

## TABLE OF CONTENTS

	Page
ACKNOWLEDGMENTS .....	v
ABSTRACT .....	vi
LIST OF TABLES .....	xi
LIST OF FIGURES .....	xii
1. INTRODUCTION .....	1
1.1 Motivation and Background .....	1
1.2 Thesis Objectives and Outline .....	10
2. COMPUTATIONAL METHODS.....	16
2.1 Introduction.....	16
2.2 Molecular-Dynamics Simulations .....	16
2.3 Monte Carlo Simulations .....	22
2.4 Density Functional Theory Calculations .....	24
2.5 Summary .....	28
3. HYDROGENATION EFFECTS ON THE STRUCTURE AND MORPHOLOGY OF SINGLE-WALLED CARBON NANOTUBES AND GRAPHENE ...	30
3.1 Introduction.....	30
3.2 Methodology.....	37
3.2.1 Structural Relaxation .....	37
3.2.2 Distribution on the Surface of Chemisorbed H Atoms.....	39
3.3 Distribution of Chemisorbed Hydrogen on Graphene and SWCNTs.....	40
3.4 Structural and Morphological Analysis of Hydrogenated Graphene and SWCNTs.....	49
3.5 Summary and Conclusions .....	61
4. EFFECTS OF STRUCTURAL CHANGES INDUCED BY HYDROGENATION ON THE HYDROGEN STORAGE CAPACITY OF CARBON NANOTUBES BUNDLES .....	63
4.1 Introduction.....	63
4.2 Development of a Mathematical Model for Predicting the Onset of Mass Transfer Limitations in SWCNT Bundles.....	65
4.3 Summary and Conclusions .....	73

5. ANALYSIS OF DIAMOND NANOCRYSTAL FORMATION ON MULTI-WALLED CARBON NANOTUBES FROM INTER-SHELL BONDING .....	74
5.1 Introduction.....	74
5.2 Computational Methods.....	77
5.3 Geometrical Parameters Controlling C-C Bonding Between Adjacent Graphene Walls of MWCNTs .....	79
5.4 DFT Analysis of Inter-shell C-C Bonding in MWCNTs.....	93
5.5 MD-generated Structurally Relaxed Inter-shell Bonded Nanocrystalline Structures Embedded in MWCNTs.....	98
5.6 Summary and Conclusions .....	104
6. INTERLAYER COVALENT BONDING IN TWISTED BILAYER GRAPHENE: ATOMIC AND ELECTRONIC STRUCTURE .....	107
6.1 Introduction.....	107
6.2 Computational Methods.....	110
6.2.1 Density Functional Theory Calculations .....	110
6.2.2 AIREBO-based Molecular-Dynamics Simulations .....	113
6.2.3 Structural Relaxation of Interlayer Bonded Configurations .....	113
6.2.4 Band Structure Calculations .....	115
6.3 Geometrical Considerations and DFT Analysis of Interlayer-Bonded Configurations in Twisted Bilayer Graphene .....	117
6.4 Electronic Structure of Interlayer-bonded Configurations .....	126
6.5 Larger Embedded Caged Configurations.....	131
6.6 Summary and Conclusions .....	133
7. SUMMARY, CONCLUSIONS AND FUTURE DIRECTIONS.....	136
7.1 Summary and Conclusions .....	136
7.2 Future Directions .....	139
7.2.1 Hydrogenation of Single-layered Carbon Nanomaterials. Practical Consequences of Structural/Morphological Changes.....	139
7.2.2 Modeling of Mass Transfer Limitations in SWCNT Bundles.....	141
7.2.3 Investigation of Mechanisms for Inter-shell/interlayer C-C Bonding in Multi-layered Materials .....	142
7.2.4 Investigation of Properties of Interlayer-bonded Structures in Twisted Bilayer Graphene .....	144
APPENDIX: AIREBO POTENTIAL AND EVALUATION OF ITS PREDICTIVE CAPABILITIES .....	146
BIBLIOGRAPHY.....	156

## LIST OF TABLES

Table	Page
<p><b>Table 6.1.</b> Lattice parameters and bulk moduli <math>B_0</math> for different carbon phases, calculated by DFT/LDA and compared to values previously reported in the literature. The <math>B_0</math> values computed for graphite correspond to uniform compression, except for the ones marked with “*”, which correspond to uniaxial compression along the direction perpendicular to the planes. Numbering of the corresponding references follows the sequence: [1] Yin, 1984; Yin and Cohen, 1984; [2] Fahy et al., 1986; Fahy and Louie, 1987; [3] Jansen and Freeman, 1987; [4] Furthmüller et al., 1994; [5] Janotti et al., 2001; [6] Kim and Chen, 2004; [7] Aoki and Amawashi, 2007; [8] Campanera et al., 2007; [9] Shallcross et al., 2008b. ....</p>	112
<p><b>Table 6.2.</b> Binding energies for interlayer bonded (<math>E_{bb}</math>) and non-bonded (<math>E_{bn}</math>) structures of <math>\theta = 30^\circ</math> and <math>30 \pm 2.204^\circ</math> twisted bilayers for different numbers of chemisorbed H atoms, <math>N_H</math>, and different hydrogenation patterns (A)-(G). ....</p>	121
<p><b>Table 6.3.</b> Values for the characteristic bond lengths as defined in Figure 6.4 for hydrogenation patterns (A), (B), and (F), for the <math>\theta = 30^\circ</math> twisted bilayer and hydrogenation patterns (A) and (F) for the <math>\theta = 30 \pm 2.204^\circ</math> twisted bilayer. For each entry (<math>d_k, k &gt; 2</math>), two values are given, corresponding to the bond lengths at the top and bottom layer of the bilayer. ....</p>	125
<p><b>Table A.1.</b> Comparison between AIREBO and first-principles DFT predictions of the equilibrium lattice parameters and cohesive energies of the cubic-diamond, hexagonal-diamond (lonsdaleite), and graphite crystalline phases. The cohesive energy differences given in parentheses are expressed with respect to the cohesive energy of graphite. Comparisons of the lattice parameter predictions and predictions of the cohesive energy ordering (relative stability between phases) confirms good agreement between AIREBO and DFT in describing bulk crystalline carbon phases. ....</p>	148
<p><b>Table A.2.</b> Average bond lengths and bond angles predicted by AIREBO and DFT calculations for (6,6) and (9,0) SWCNTs with different numbers of adsorbed H atoms onto the nanotube wall. ....</p>	151

## LIST OF FIGURES

Figure	Page
<b>Figure 1.1.</b> (a) Cubic diamond and (b) graphite crystalline structures. (c) Individual graphene plane (carbon atoms in a honeycomb lattice). .....	2
<b>Figure 1.2.</b> (a) Fullerene C <sub>60</sub> structure; (b) regular soccer ball. Hexagons and pentagons on the ball correspond to the white and black patches respectively. ....	3
<b>Figure 1.3.</b> Definition of the chiral vector $\underline{OA} = n\underline{a}_1 + m\underline{a}_2$ on the honeycomb lattice of carbon atoms in a graphene sheet (Dresselhaus, 1997); in this notation, $\underline{a}_1$ and $\underline{a}_2$ represent the unit vectors of the 2D graphene lattice. ....	5
<b>Figure 1.4.</b> Bottom: Configurations of (a) zigzag (12,0), (b) armchair (7,7), and (c) chiral (10,4) carbon nanotubes. Top: Top view of the graphene planes which generated the nanotubes. ....	5
<b>Figure 1.5.</b> Multi-walled carbon nanotube formed by three concentric graphene layers (10,0)@(19,0)@(28,0). (a) Top view. (b) front view on the $(r, z)$ plane of a cylindrical-coordinate system, where the $z$ -direction is along the nanotube axis. ....	6
<b>Figure 3.1.</b> (a) C-C radial distribution function, $\rho g(r)$ , in hydrogenated (14,14) SWCNTs at different H surface coverages, $\Theta$ . (b) Example of a hydrogenated graphene layer, depicting the three typical types of C-C bonds (shown in magnification) that have been classified as $sp^2$ , $sp^3$ -A, and $sp^3$ -B bonds; these types of bonds correspond to the three peaks in the $\rho g(r)$ distributions in (a) that have been marked accordingly. ....	42

**Figure 3.2.** (a) Fraction,  $\phi$ , of  $sp^2$  and  $sp^3$  C-C bonds in the structure of hydrogenated graphene as a function of H surface coverage,  $\Theta$ . The fractions of  $sp^2$ ,  $sp^3$ -A, and  $sp^3$ -B bonds are denoted by squares, diamonds, and circles, respectively. The inset shows the dependence on  $\Theta$  of the chemisorbed H binding energy,  $E_b$ . (b) Average size of clusters of hydrogenated (diamonds) and non-hydrogenated (circles) carbon atoms in the structure of hydrogenated graphene as a function of  $\Theta$ ; the cluster size is measured in number of carbon atoms. In all the plots shown, open and filled symbols are used to denote random distributions (initial states) and MC-relaxed distributions of chemisorbed H atoms, respectively.....44

**Figure 3.3.** Top views (maps) of representative distributions of H atoms chemisorbed onto graphene layers with H surface coverages of (a)  $\Theta = 0.25$ , (b)  $\Theta = 0.40$ , (c)  $\Theta = 0.50$ , and (d)  $\Theta = 0.60$ . The first and second columns show simulation-generated maps based on random and MC-optimized distributions, respectively. Only carbon atoms are shown for clarity. Carbon atoms shaded dark gray and light gray are used to denote hydrogenated and non-hydrogenated surface sites, respectively. The third column shows STM images of hydrogenated graphite surfaces at surface coverages that are similar to those of the simulation-generated maps on each corresponding row, reproduced from Hornekær et al., 2006b. In these STM images, the bright spots correspond to the hydrogenated surface sites. ....48

**Figure 3.4.** Relaxed configurations of hydrogenated graphene with H surface coverages of (a)  $\Theta = 0.25$ , (b)  $\Theta = 0.40$ , and (c)  $\Theta = 0.55$ . The top row shows three-dimensional views of the configurations, highlighting the graphene surface morphology. Carbon atoms shaded dark gray (colored blue online) and light gray (colored orange online) are used to denote hydrogenated and non-hydrogenated sites, respectively. The middle row shows contour plots of the corresponding surface morphologies, in terms of the distribution on the graphene plane of the vertical displacements of the carbon atoms with respect to the planar morphology at  $\Theta = 0$ . The color/shade is darkest at the deepest valleys and lightest at the highest hills of the surface morphology. The bottom row depicts top views (maps) of the distributions of the H atoms chemisorbed onto the graphene layers; carbon atoms shaded dark gray and light gray are used to denote hydrogenated and non-hydrogenated sites, respectively. ....50

- Figure 3.5.** Relaxed configurations of a hydrogenated (24,0) SWCNT (shown on the left) with (a)  $\Theta = 0.25$ , (b)  $\Theta = 0.40$ , (c)  $\Theta = 0.55$ , and (d)  $\Theta = 0.75$ , with the corresponding top views (maps) of the chemisorbed hydrogen distributions on the unrolled surface of the zigzag nanotube (shown on the right). The horizontal lines crossing the H distribution maps represent the top and bottom tangent planes depicted in the corresponding three-dimensional configurations. In all of the atomic configurations and H distribution maps shown, the dot-dashed vertical lines are perpendicular to the nanotube axis. ....52
- Figure 3.6.** Surface roughness,  $\eta_z$  and  $\eta_r$ , as a function of H surface coverage,  $\Theta$ , for hydrogenated graphene sheets (triangles) and SWCNTs (squares, diamonds, and circles). The different symbols for the SWCNT results represent values for different average diameters of the pristine nanotubes, with  $D_{\text{avg}} = 1.18$  nm, 1.57 nm, and 1.86 nm for the data sets labeled D1, D2, and D3, respectively. ....53
- Figure 3.7.** (a) Chemisorbed H binding energy,  $E_b$  (circles), axial strain  $\Delta L/L_0$  (squares), and radial strain  $\Delta R/R_0$  (diamonds) for a (24,0) SWCNT and (b)  $E_b$  (circles) and strains along the two principal directions  $x$  and  $y$ ,  $\Delta L_x/\Delta L_{x0}$  (squares) and  $\Delta L_y/\Delta L_{y0}$  (diamonds), for a hydrogenated planar graphene sheet as functions of H surface coverage,  $\Theta$ . Open and filled symbols are used to denote random distributions (initial states) and MC-relaxed distributions of chemisorbed H atoms, respectively. ....57
- Figure 3.8.** (a) Axial strain,  $\Delta L/L_0$ , and (b) radial strain,  $\Delta R/R_0$ , as functions of H surface coverage,  $\Theta$ , for relaxed hydrogenated SWCNTs of different diameters and chiralities. ....58
- Figure 3.9.** Chemisorbed H binding energy,  $E_b$ , as a function of H surface coverage,  $\Theta$ , for hydrogenated SWCNTs of different diameters and chiralities and for a graphene sheet. ....59
- Figure 3.10.** Volumetric ( $\overline{\Delta V/V_0}$ ) and areal ( $\overline{\Delta A/A_0}$ ) deformation parameters as functions of H surface coverage,  $\Theta$ , for relaxed hydrogenated SWCNTs of different diameters and chiralities and for graphene, respectively. ....59
- Figure 3.11.** Dependence of the ratio  $f$  of  $sp^2$ - to  $sp^3$ -bonded C atoms on the H coverage  $\Theta$  for a (12,0) and a (15,0) SWCNT denoted by diamonds and squares, respectively. Filled and open symbols are used to denote AIREBO-MD results and DFT/GGA results, respectively. The inset shows AIREBO-MD results for the dependence on  $\Theta$  of the axial strain  $\Delta L/L$  (triangles) and the ratio  $f$  (circles) for a (14,14) SWCNT at  $T = 0.1$  K (filled symbols) and 300 K (open symbols); there is almost complete overlap between the two sets of  $f(\Theta)$  results at the two different temperatures. ....60

- Figure 4.1.** (a) Schematic of a SWCNT bundle exposed to an atomic H flux; the bundle is represented by a regular array of SWCNTs forming a hexagonal lattice on the plane normal to the SWCNT axes. The bundle is shown before (top) and after (bottom) its partial hydrogenation; the decrease in inter-tube spacing (bottom) is due to SWCNT swelling. (b) Characteristic dimensions of the bundle, namely SWCNT radius,  $R$ , SWCNT center-to-center distance,  $a$ , and inter-tube spacing,  $d$ . The dashed lines are used to indicate deformation due to SWCNT swelling upon hydrogenation.....66
- Figure 4.2.** (a) Dependence on the H coverage  $\Theta$  of the radial strain  $\Delta R/R_0$  for the (24,0) (solid diamonds), (20,0) (gray diamonds), (15,0) (open diamonds), (9,9) (open squares), and (13,4) (open circles) SWCNTs. The inset shows the dependence of  $\Delta R/R_0$  on the pristine-SWCNT diameter for fully hydrogenated ( $\Theta = 1$ ) zigzag (solid diamonds), chiral (solid circles), and armchair (solid squares) nanotubes; the chiral SWCNTs examined have chiral angles ranging from  $13.0^\circ$  to  $18.3^\circ$ . (b) Least-squares fitting of the swelling function  $f(\Theta) = \kappa(\Theta - \Theta_c) H(\Theta - \Theta_c)$  (solid line) to the atomistic-simulation results (discrete symbols) for the (9,9) SWCNT.....68
- Figure 4.3.** Estimated parameters  $\kappa$  and  $\Theta_c$  in the parameterization of the nanotube swelling function for SWCNTs of different diameters and chiralities.....70
- Figure 4.4.** (a) Dimensionless inter-tube spacing  $\delta$  as a function of  $\Theta$  and its variation with the bundle density, as expressed by the dimensionless lattice parameter  $\alpha$ . The lines shown correspond to  $\alpha = 9.1, 9.4, 9.7, 10.0,$  and  $10.3$ . The inset shows the decrease of the bundle density as the lattice parameter increases; both quantities are made dimensionless with their values at the pristine state,  $\Theta = 0$ . (b)  $\delta$  as a function of  $\Theta$  for two bundle densities and its dependence on nanotube diameter or chirality, as expressed by the dimensionless parameter  $\kappa$ . The different lines in the two sets correspond to  $\kappa = 0.22, 0.24,$  and  $0.26$ . .....72
- Figure 5.1.** Three possible alignments, (a), (b), and (c), between two adjacent graphene planes and respective local structures generated by the formation of inter-planar C–C bonds. In each case, different planar views are displayed in a Cartesian frame of reference. Blue and black spheres are used to denote C atoms on the two adjacent graphene planes, respectively, that are bonded to each other. ....81

- Figure 5.2.** (a) Top view of relative alignment maps for two pairs of armchair nanotubes,  $(30,30)@(35,35)$  and  $(50,50)@(55,55)$ , arranged concentrically. The dotted lines are used to mark the regions (a total of ten) where a certain alignment, type I or type II, is favored. (b, c) Front views of the  $(50,50)@(55,55)$  DWCNT in (b) a region where type-II alignment is favorable and (c) a region where type-I alignment is favorable. (d, e) Top views of the  $(50,50)@(55,55)$  DWCNT with close views of the local structures generated by inter-shell C-C bond formation in (d) one of the regions colored blue in (a) where type-II alignment is favorable and (e) one of the regions colored black in (a) where type-I alignment is favorable. (f) Angle  $\alpha$  used for determining the possible alignment type according to the criteria described in the text. (g) Misalignment angle between nearest-neighbor atoms in different adjacent concentric nanotube graphene walls as a function of the polar angle  $\theta$  in a cylindrical frame of reference for the sections marked in (a). .....83
- Figure 5.3.** Moiré patterns for pairs of graphene planes rotated by different angles. For the case  $\phi = 3.89^\circ$ , the regions characterized by alignments of types I (Figure 5.1(a)) and II (Figure 5.1(b)) are marked with dotted circles in black and blue respectively; the interstitials between these domains are characterized by the alignment observed in Figure 1(c). .....87
- Figure 5.4.** Relative alignment maps for DWCNTs formed by two chiral nanotubes with a difference in the chiral angles,  $\Delta\chi$ , varying from  $3.88^\circ$  to  $16.8^\circ$  and an average diameter,  $D$ , of approximately 8.9 nm. The blue and black colored regions correspond to atoms with inter-shell alignments as depicted in Figures 5.1(b) and 5.1(a), respectively, which favor the formation of hexagonal-diamond and cubic-diamond seeds, respectively. Only the outer nanotubes are shown for clarity. The DWCNTs have indices (a)  $(87,29)@(88,40)$  with  $D = 8.88$  nm and  $\Delta\chi = 3.89^\circ$ ; (b)  $(80,40)@(98,28)$  with  $D = 8.97$  nm and  $\Delta\chi = 6.89^\circ$ ; (c)  $(85,34)@(77,55)$  with  $D = 8.99$  nm and  $\Delta\chi = 8.40^\circ$ ; (d)  $(99,9)@(90,36)$  with  $D = 8.80$  nm and  $\Delta\chi = 11.80^\circ$ ; (e)  $(99,11)@(86,43)$  with  $D = 8.91$  nm and  $\Delta\chi = 13.90^\circ$ ; and (f)  $(72,48)@(105,15)$  with  $D = 8.87$  nm and  $\Delta\chi = 16.83^\circ$ . .....90

- Figure 5.5.** Relative alignment maps for DWCNTs with indices (a) (58,58)@(70,56) with  $D = 8.56$  nm and  $\Delta\chi = 3.67^\circ$ ; (b) (94,94)@(110,88) with  $D = 13.45$  nm and  $\Delta\chi = 3.67^\circ$ ; (c) (112,0)@(112,16) with  $D = 9.46$  nm and  $\Delta\chi = 6.59^\circ$ ; and (d) (165,0)@(161,23) with  $D = 13.59$  nm and  $\Delta\chi = 6.59^\circ$ . Only the outer nanotubes are shown for clarity and the coloring scheme is consistent with that of Figure 5.4. Comparing (a) with (b) and (c) with (d) shows that the sizes of the colored regions are independent of the DWCNT average diameter and depend only on the difference in the chiral angle,  $\Delta\chi$ , of the two nanotubes in each DWCNT. ....91
- Figure 5.6.** Relative alignment maps for DWCNTs with indices (a) (56,0)@(54,18) with  $D = 5.08$  nm and  $\Delta\chi = 13.9^\circ$ ; (b) (31,31)@(50,20) with  $D = 4.89$  nm and  $\Delta\chi = 13.9^\circ$ ; and (c) (54,6)@(50,25) with  $D = 5.18$  nm and  $\Delta\chi = 13.9^\circ$ . Only the outer nanotubes are shown for clarity and the coloring scheme is consistent with that of Figure 5.4. Comparing (a), (b), and (c) with each other shows that the sizes of the colored regions are independent of the chirality of the individual nanotubes and depend only on the difference in the chiral angle,  $\Delta\chi$ , of the two nanotubes in each DWCNT. ....92
- Figure 5.7.** Maximum number of hexagonal cells in an individual patch of a relative alignment map in DWCNTs as a function of the difference in the chiral angles,  $\Delta\chi$ , between the individual nanotubes of the DWCNTs and for various DWCNT average diameters. Black, gray, and open symbols are used to represent combinations of zigzag (Z) and chiral (C) walls (Z@C), armchair (A) and chiral walls (A@C), and two chiral walls (C@C), respectively. Diamonds, squares, and triangles correspond to DWCNTs with average external diameters  $D_1 = 5.20$  nm,  $D_2 = 9.01$  nm, and  $D_3 = 13.64$  nm, respectively. ....92

**Figure 5.8.** Structure resulting from inter-shell C-C bonding in a MWCNT according to first-principles DFT calculations. (a-d) Optimized atomic configuration of MWCNT with indices (6,0)@(15,0)@(24,0), i.e., with (6,0), (15,0), and (24,0) concentric inner (colored in blue), middle (colored in green), and outer (colored in gray) nanotubes, respectively, depicting inter-shell C-C bonding. (a) Top view along the axial direction. (b) Cross-sectional view on the symmetry plane. Blue, green, gray, and yellow spheres denote C atoms. The yellow colored C atoms highlight the seed unit for the nucleation of a bulk phase of hexagonal diamond. (c) Valence electron density (VED) distribution on a plane perpendicular to the axial direction of the MWCNT. (d) VED distribution on a plane parallel to the axial direction of the MWCNT, containing the atoms labeled C1, C2, and C3 in (a) and (b). The VED distributions in (c) and (d) highlight the inter-tube interactions and reveal the inter-shell C-C bonding and the accompanying shell distortions and structural relaxations [e.g., region enclosed by the triangle in (c)]. (e) Lonsdaleite lattice. (f) VED distribution for the lonsdaleite phase on the plane of C atoms labeled C4, C5, and C6 in (e). In (b) and (e), the numbers shown indicate interatomic distances or lattice parameters in Å. In (c), (d), and (f), the VED increases as the color changes from red (zero VED) to blue. ....96

**Figure 5.9.** Structure resulting from inter-shell C-C bonding in a MWCNT according to first-principles DFT calculations. (a-e) Optimized atomic configuration of a (6,0)@(15,0)@(24,0) MWCNT with (6,0), (15,0), and (24,0) concentric inner (colored in blue), middle (colored in green), and outer (colored in gray) nanotubes, respectively, depicting inter-shell C-C bonding. (a) Top view along the axial direction. (b) Only a small region from the original supercell in (a) is shown highlighting the seed unit for the nucleation of a cubic-diamond crystal. Blue, green, and gray spheres denote C atoms. (c) VED distribution on a plane perpendicular to the axial direction of the MWCNT. (d) VED distribution on another plane perpendicular to the axial direction of the MWCNT. (e) VED distribution on a plane containing the atoms labeled C7, C8, and C9 in (a) and (b). The VED distributions in (c), (d), and (e) highlight the inter-tube interactions and reveal the inter-shell C-C bonding and the accompanying shell distortions and structural relaxations. (e) Cubic-diamond lattice. (f) VED distribution for the cubic-diamond phase on the plane of C atoms labeled C12, C13, and C14 in (f). In (b) and (f), the numbers shown indicate interatomic distances or lattice parameters in Å. In (c), (d), (e), and (g), the VED increases as the color changes from red (zero VED) to blue. ....97

**Figure 5.10.** Representative MD-relaxed local structures formed by the creation of inter-shell C-C bonds in a DWCNT with indices (63,63)@(81,54) and  $\Delta\chi = 6.6^\circ$ . (a) Regions of the DWCNT where these relaxed structures are created, marked with black and blue circles, and local coordinate vectors used for structural analysis and visualization. Only the outer nanotube of the DWCNT is shown for clarity and the coloring scheme is consistent with that of Figure 5.4. (b, c) Local structures that can act as seeds for the nucleation of (b) the cubic-diamond phase and (c) the hexagonal-diamond phase, extracted from the DWCNT. (d, e) Different planar views, (i), (ii), (iii), and (iv), of the structures given in (b) and (c), respectively, using the local coordinates defined in (a). In (b)-(e), orange and green spheres are used to represent carbon atoms belonging to the outer and inner nanotube of the DWCNT, respectively.....100

**Figure 5.11.** Representative MD-relaxed local structures formed by the creation of inter-shell C-C bonds in a DWCNT with indices (99,9)@(90,36) and  $\Delta\chi = 11.8^\circ$ . (a) Regions of the DWCNT where these relaxed structures are created, marked with black and blue circles, and local coordinate vectors used for structural analysis and visualization. Only the outer nanotube of the DWCNT is shown for clarity and the coloring scheme is consistent with that of Figure 5.4. (b, c) Local structures that can act as seeds for the nucleation of (b) the cubic-diamond phase and (c) the hexagonal-diamond phase, extracted from the DWCNT. (d, e) Different planar views, (i), (ii), (iii), and (iv), of the structures given in (b) and (c), respectively, using the local coordinates defined in (a). In (b)-(e), orange and green spheres are used to represent carbon atoms belonging to the outer and inner nanotube of the DWCNT, respectively.....101

**Figure 5.12.** Representative MD-relaxed local structures formed by the creation of inter-shell C-C bonds in a DWCNT with indices (110,0)@(95,38) and  $\Delta\chi = 16.1^\circ$ . (a) Regions of the DWCNT where these relaxed structures are created, marked with black and blue circles, and local coordinate vectors used for structural analysis and visualization. Only the outer nanotube of the DWCNT is shown for clarity and the coloring scheme is consistent with that of Figure 5.4. (b, c) Local structures that can act as seeds for the nucleation of (b) the cubic-diamond phase and (c) the hexagonal-diamond phase, extracted from the DWCNT. (d, e) Different planar views, (i), (ii), (iii), and (iv), of the structures given in (b) and (c), respectively, using the local coordinates defined in (a). In (b)-(e), orange and green spheres are used to represent carbon atoms belonging to the outer and inner nanotube of the DWCNT, respectively.....102

- Figure 5.13.** Crystalline structures embedded locally in a (50,50)@(55,55)@(60,60) MWCNT due to inter-shell C-C bonding that provide seeds for the nucleation of (a) cubic diamond and (b) hexagonal diamond. In both (a) and (b), a top view of the MWCNT with the embedded nanocrystal is shown on the left and three different close planar views of the nanocrystalline regions are shown on the right, corresponding from top to bottom to the planes  $(\theta,z)$ ,  $(r,\theta)$ , and  $(r,z)$  in a cylindrical-coordinate system. ....104
- Figure 6.1.** Computed binding energies,  $\Delta E$ , as a function of cutoff energy for plane waves,  $E_c$ , for interlayer-bonded structures with  $\theta = 30^\circ$  and hydrogenation patterns A, B, C, and D (defined in Section 6.3). Results are presented in terms of the ratio of the energy for a given cutoff over the energy computed at  $E_c = 60$  Ry. ....115
- Figure 6.2.** Band structures for single-layer graphene computed using (a)  $1 \times 1$  and (b)  $2 \times 2$  supercells and bilayer graphene using a  $2 \times 2$  supercell for (c) *AB* and (d) *AA* stacking. ....116
- Figure 6.3.** (a, b) Moiré patterns generated by a pair of graphene layers rotated by angles of  $\theta = 30^\circ$  and  $\theta = 30 \pm 2.204^\circ$  with respect to each other, respectively. The dark shaded atoms (colored blue online) correspond to those involved in the creation of the embedded caged structures; dotted lines are used to visualize the superlattices. (c) Supercell for a  $\theta = 30^\circ$  twisted bilayer and top and side views of the interlayer-bonded configurations generated. Open squares, open diamonds, and X marks are used to denote either interlayer bonded or hydrogenated C atoms. The shaded (colored online) atoms are removed from the structure and relaxed, generating the  $C_{48}$  and  $C_{72}$  fullerenes, different views of which are depicted in (d). For each panel in (d), caged structures removed from the bilayers (left side) and relaxed further (right side) are presented. (e) Valence electron density (VED) distributions on planes normal to the surface of the pristine and bonded bilayers (top and bottom, respectively, in the image on the left), and on planes  $P_1$ ,  $P_2$ , and  $P_3$  parallel to the graphene layers at different positions, as defined in (c). The VED increases as the color changes from red (zero VED) to blue. For interpretation of the references to color in the VED distributions, the reader is referred to the online version of this thesis. ....119

<b>Figure 6.4.</b> Characteristic bond lengths for (a) $C_{48}$ and (b) $C_{72}$ embedded caged structures generated by interlayer bonding in the $\theta = 30^\circ$ twisted bilayer; for the $\theta = 30 \pm 2.204^\circ$ twisted bilayer, the supercell is different, but the internal caged structure has the same geometry. Chemisorbed H atoms have been removed from the configurations for clarity.....	124
<b>Figure 6.5.</b> Electronic band structures for pristine (dotted blue curves), hydrogenated interlayer-bonded (solid green curves), and hydrogenated non-bonded (dashed red curves) twisted bilayer graphene for rotation angles of (a,b) $\theta = 30^\circ$ and (c,d) $\theta = 30 \pm 2.204^\circ$ . Band diagrams correspond to configurations (a,c) with hydrogenation pattern (A) and (b,d) with hydrogenation pattern (F), generating embedded $C_{48}$ and $C_{72}$ caged structures, respectively. The energies are plotted along the path in the Brillouin zone illustrated in the inset. ....	128
<b>Figure 6.6.</b> Supercells (top) and corresponding band structures (bottom) of (a) armchair-oriented layer ( $4\sqrt{3} \times 4\sqrt{3}$ $R30^\circ$ supercell); (b) zigzag-oriented layer ( $7 \times 7$ supercell); and (c) layer ( $2\sqrt{13} \times 2\sqrt{13}$ $R46.1^\circ$ supercell) rotated by $16.1^\circ$ with respect to layer in (b).....	129
<b>Figure 6.7.</b> (a-c) Embedded caged structures formed by interlayer C-C bonding in a $\theta = 30^\circ$ twisted bilayer, containing different numbers of atoms ( $N_{AT}$ ) and interlayer bonds ( $N_{IB}$ ). In each case, the atoms involved in the creation of the interlayer-bonded configurations are marked on the left side of each panel, and different views of the removed/relaxed fullerenes are displayed on the right. ....	132
<b>Figure 6.8.</b> Additional embedded caged configurations formed by interlayer bonding in a $\theta = 30^\circ$ twisted bilayer containing different numbers of atoms ( $N_{AT}$ ) and interlayer bonds ( $N_{IB}$ ). The atoms involved in the creation of the interlayer-bonded configurations are marked at the top of each panel, and different views of the removed/relaxed fullerenes are displayed at the bottom. ....	133
<b>Figure A.1.</b> (a) Curvature energy as function of (a) CNT radius R and (b) $1/R^2$ .....	148
<b>Figure A.2.</b> Curvature energy as function of CNT radius R. Comparison between AIREBO predictions with DFT results for zigzag nanotubes (Gulseren et al., 2002a).....	150
<b>Figure A.3.</b> Relaxed structures for a (6,6) CNT with three H atoms chemisorbed onto the CNT surface, obtained by AIREBO and DFT calculations (Barnard et al., 2005).....	150

<b>Figure A.4.</b> Dependence on CNT radius, $R$ , of the binding energies for the chemisorption of a single H atom onto the outer surface of SWCNTs of various diameters, as predicted by the AIREBO potential. The blue line marks the limit $R \rightarrow \infty$ , corresponding to a planar graphene sheet.....	152
<b>Figure A.5.</b> Dependence on CNT radius, $R$ , of binding energies for the chemisorption of a single H atom onto the outer surface of SWCNTs of various diameters. Comparison of AIREBO predictions with our DFT results and DFT results from the literature (Barnard et al., 2005; Gulseren et al., 2001). .....	153
<b>Figure A.6.</b> Dependence on CNT radius, $R$ , of binding energies for chemisorption of H atoms onto the surface of SWCNTs of different diameters and chiralities at a uniform coverage of 50%. The blue line marks the $R \rightarrow \infty$ limit, corresponding to a planar graphene sheet.....	153
<b>Figure A.7.</b> Dependence on CNT radius, $R$ , of binding energies for chemisorption of H atoms onto the surface of SWCNTs of different diameters and chiralities at a coverage of 100%. .....	154
<b>Figure A.8.</b> Axial and radial strains resulting from chemisorption of H atoms onto SWCNTs of different diameters and chiralities at a surface coverage of 100%, as obtained by AIREBO-based relaxation simulations (see Chapter 3). Results from DFT calculations (Yildirim et al., 2001) also are included, and denoted by light-filled symbols. ....	155

# CHAPTER 1

## INTRODUCTION

### 1.1 Motivation and Background

Over the past two decades, the field of nano-scale science and technology has experienced remarkable advances, as demonstrated by the exponential increase in the number of scientific publications and patents in the area. Nanostructured materials exhibit unusual combinations of properties, which make their function unique and enable a broad range of technological applications. Carbon-based nanomaterials, such as fullerenes, carbon nanotubes, and graphene, hold a prominent position among this relatively new class of materials.

Hybridization between  $s$  and  $p$  orbitals in carbon atoms allows them to form a great variety of bonding configurations, which gives origin to a series of carbon allotropes with very distinct physical properties. Graphite, formed by stacked graphene planes, i.e., planes of  $sp^2$ -hybridized C atoms arranged in a honeycomb lattice, is the ground state of carbon under ambient conditions; at high pressures and temperatures,  $sp^3$ -bonded cubic diamond is the most stable phase (Dresselhaus et al., 1996, 2001). The lattice structures of graphite and cubic diamond are illustrated in Figure 1.1. These two carbon allotropes are the most common in nature and, for a long time, they had been the only ones known to exist (Hirsch, 2010). Over the past five decades, a series of new carbon allotropes have been identified in nature (e.g., in rocks and meteorite fragments) and/or synthesized in the laboratory, such as the hexagonal diamond phase, also called

lonsdaleite (Bundy and Kasper, 1967; Frondel and Marvin, 1967; Hanneman et al., 1967), carbynes (Kasatochkin et al., 1973; Whittaker et al., 1980), and the fascinating family of carbon nanostructures comprised of fullerenes (Kroto et al., 1985), carbon nanotubes (Iijima, 1991), and single-layer graphene (Novoselov et al., 2004, 2005). In addition to these familiar allotropes, carbon has been reported to exist in two yet unsolved but presumably cubic structures, commonly referred to as *i*-carbon and *n*-diamond (Vora and Moravec, 1981; Hirai and Kondo, 1991). Other metastable phases have been predicted theoretically, such as the body-centered tetragonal C<sub>4</sub> (BCT-C4) (Schultz et al., 1999; Umemoto et al., 2010), and a monoclinic phase called M-carbon (Li et al., 2009); these theoretical studies also present evidence of formation of BCT-C4 and M-carbon during experiments of cold compression of graphite, previously reported in the literature (Mao et al., 2003).

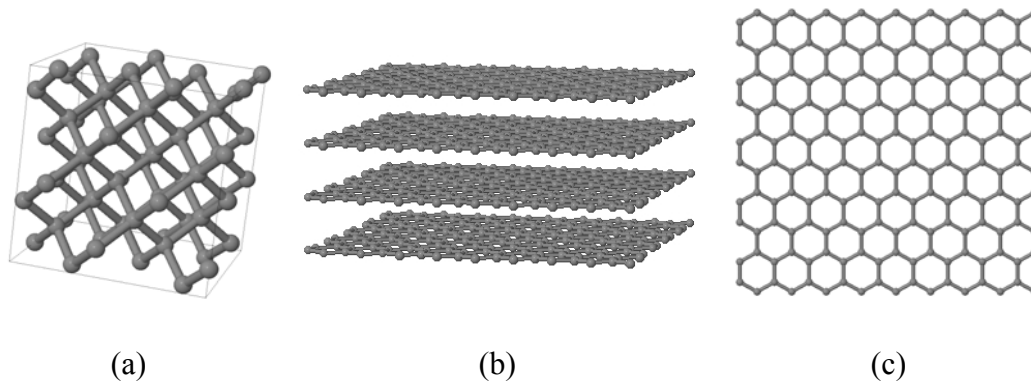


**Figure 1.1.** (a) Cubic diamond and (b) graphite crystalline structures. (c) Individual graphene plane (carbon atoms in a honeycomb lattice).

In the mid-1980s, Harold W. Kroto, Richard E. Smalley, Robert F. Curl Jr., and their coworkers, were carrying out experiments with laser vaporization of graphite, aimed at understanding the mechanisms by which carbon-based long-chain molecules and clusters are formed in interstellar space. In these experiments, they discovered a

remarkably stable cluster formed by 60 atoms (Kroto et al., 1985), which was proposed to have a regular truncated icosahedron structure (a polyhedron with 60 vertices and 32 faces – 12 pentagonal and 20 hexagonal), resembling a regular soccer ball, as illustrated in Figure 1.2; this nanosized cluster was named buckminsterfullerene (after the architect Richard Buckminster Fuller, famous for designing geodesic domes), or simply fullerene. Fullerene is presently used as the generic name for a whole class of small clusters of carbon atoms (tens to hundreds of atoms) in a closed-cage structure; the most common and famous member of this class is the original  $C_{60}$ , also known as buckyball.



**Figure 1.2.** (a) Fullerene  $C_{60}$  structure; (b) regular soccer ball. Hexagons and pentagons on the ball correspond to the white and black patches respectively.

Fullerene  $C_{60}$  is formed essentially by  $sp^2$ -hybridized C-C bonds with two characteristic bond lengths (in pentagons, they C-C bonds are longer than in hexagons); this indicates that electron delocalization over the structure is not complete and, consequently,  $C_{60}$  fullerenes are not “superaromatic” molecules as one would expect.  $C_{60}$  behaves as an electron-deficient alkene that is able to react easily with electron-donor species (Dresselhaus et al., 1996; Hirsch, 2010). A comprehensive discussion of its unique chemical, electronic, and optical properties has been presented elsewhere

(Dresselhaus et al., 1996; Dresselhaus, 1997). Fullerenes have found applications in diverse areas, such as electronics, organic photovoltaics (fullerene/polymer junctions), and medical treatment and diagnosis (Dresselhaus et al., 1996; Hirsch, 2010); however, more than 25 years after their discovery, they have not found their place in the market (van Noorden, 2011).

The discovery of fullerenes stimulated strongly the search for new possible carbon-based nanostructured materials. In 1991, Sumio Iijima of NEC Laboratories in Japan (Iijima, 1991) reported the synthesis of a new class of materials, which he first called “graphitic carbon needles” or “helical microtubules of graphitic carbon” and they are now widely known as carbon nanotubes (CNTs). Since this discovery, an extremely large body of theoretical and experimental work has been carried out on the synthesis, characterization, properties, and applications of CNTs.

Carbon nanotubes are hollow cylinders formed exclusively by  $sp^2$ -hybridized carbon atoms. Their fundamental structure consists of a graphene sheet rolled up into a cylinder. The CNT structure is classified according to the so-called chiral vector that defines the direction along which the graphene plane is rolled up (Dresselhaus, 1997). Figure 1.3 gives the definition of the chiral vector,  $\underline{OA} = n\underline{a}_1 + m\underline{a}_2$ , which can be represented by the pair of indices  $(n,m)$ , where  $\underline{a}_1$  and  $\underline{a}_2$  are the two unit vectors of the 2D honeycomb lattice of the graphene sheet.

When  $m \neq n \neq 0$ , the resulting CNT configuration is simply called “*chiral*”, and the angle  $\theta$  defined in Figure 1.3 is given by  $\theta = \arctan(\sqrt{3}m/(m+2n))$ . When  $m = n$ , the resulting CNT configuration is called “*armchair*” ( $\theta = 30^\circ$ ). When  $m = 0$ , the resulting

CNT configuration is called “zigzag” ( $\theta = 0^\circ$ ). The diameter of the nanotube is given by

$$d = \sqrt{3}a_{C-C} \left( m^2 + mn + n^2 \right)^{\frac{1}{2}} / \pi, \text{ where } a_{C-C} \text{ is the length of the } sp^2 \text{ C-C bond. Figure 1.4}$$

shows representative configurations of zigzag, armchair, and chiral nanotubes.

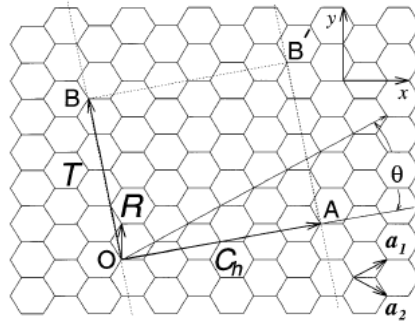


**Figure 1.3.** Definition of the chiral vector  $\underline{OA} = n\underline{a}_1 + m\underline{a}_2$  on the honeycomb lattice of carbon atoms in a graphene sheet (Dresselhaus, 1997); in this notation,  $\underline{a}_1$  and  $\underline{a}_2$  represent the unit vectors of the 2D graphene lattice.

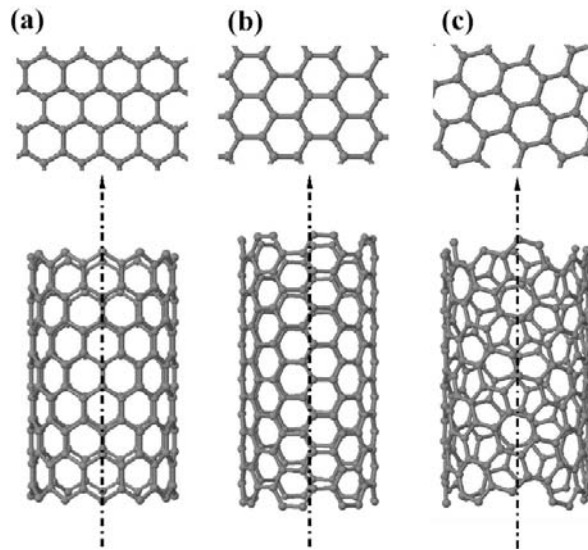


**Figure 1.4.** Bottom: Configurations of (a) zigzag (12,0), (b) armchair (7,7), and (c) chiral (10,4) carbon nanotubes. Top: Top view of the graphene planes which generated the nanotubes.

Carbon nanotubes may consist of a single graphene wall, such as those depicted in Figure 1.4; in this case, they are called single-walled carbon nanotubes (SWCNTs). Typically, SWCNTs have diameters on the order of nanometers, and lengths up to centimeters (Dai, 2002). In addition, CNTs may consist of two or more graphene walls arranged as concentric tubes, such as that illustrated in Figure 1.5; in such a case, they are called multi-walled carbon nanotubes (MWCNTs). Typically, MWCNT diameters lie within the range of 5-100 nm, most commonly from 10 to 20 nm (Dai, 2002; Grobert, 2007) with an average inter-shell spacing of 0.34 nm, a value close to the interlayer spacing in graphite. The CNTs discovered in the original experiments reported by Iijima were MWCNTs (Iijima, 1991); the synthesis of SWCNTs was reported for the first time a couple of years later (Iijima and Ichihashi, 1993; Bethune et al., 1993).

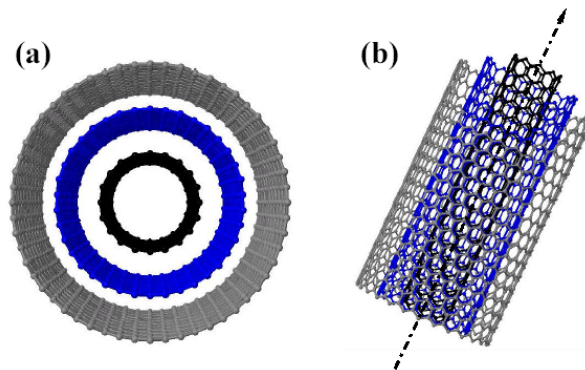


**Figure 1.5.** Multi-walled carbon nanotube formed by three concentric graphene layers (10,0)@(19,0)@(28,0). (a) Top view. (b) front view on the  $(r, z)$  plane of a cylindrical-coordinate system, where the  $z$ -direction is along the nanotube axis.

Carbon nanotubes are endowed with a wide variety of intriguing properties. They are among the strongest and most resilient materials known to exist (Dai, 2002). They have a very high Young modulus (on the order of 1 TPa) and tensile strength (on the order of 1 GPa) (Dai, 2002; Meyyapan et al., 2003; Grobert, 2007). They can be either

metallic or semiconducting, depending on their chirality (Dresselhaus, 1997): armchair CNTs are always metallic, while one third of all possible CNTs with zigzag and chiral configurations can be metallic, with the remaining ones being semiconducting. Furthermore, CNTs have a high thermal conductivity and a low density. This outstanding combination of mechanical and electronic properties makes CNTs suitable for a variety of potential and current applications, including biological and chemical sensors, scanning probes, nanoelectronics, reinforced composites, field-emitters, heat sinks, hydrogen storage media, and low-resistance interconnects among others. A comprehensive list of references related to applications of CNTs can be found in the review articles by Dai (Dai, 2002) and by Grobert (Grobert, 2007).

The “youngest” member of the “nano-carbon family” is single-layer graphene (SLG), which consists of one-atom-thick layer of  $sp^2$  carbon atoms – the “building block” of graphite, as illustrated in Figure 1.1; graphene has been the subject of particularly intensive research over the past few years. For a long time, the existence of such stable two-dimensional materials had been considered unlikely (Peierls, 1935; Landau, 1937; Mermin, 1968). In 2004, Andre Geim and Konstantin Novoselov of the University of Manchester (Novoselov et al., 2004, 2005) reported for the first time the synthesis and electronic properties of isolated single-layer graphene sheets, obtained by mechanical exfoliation using scotch tape (a simple, naïve, and efficient procedure). Single-layer graphene (or just graphene, from now on) is the thinnest known material, it is optically transparent, it has the highest strength ever measured in any material (Lee et al., 2008), and it has a thermal conductivity even higher than that of carbon nanotubes at room temperature (Balandin et al., 2008). But even more remarkable are the unique electronic

properties of this material. Graphene is a zero-band-gap semiconductor (or semi-metal), with valence and conduction bands crossing at the Fermi level on the special  $K$  point in the Brillouin zone; around this point, electrons have a linear dispersion and, as a result, they behave like relativistic particles as described by the Dirac equation, moving at speeds about 300 times slower than the speed of light (Avouris et al., 2007; Geim and Novoselov, 2007; Zhu et al., 2010). Graphene also possesses very high carrier mobilities; electrons can travel sub-micrometer-long distances without scattering (Geim and Novoselov, 2007; Zhu et al., 2010). These features endow graphene with exotic properties due to quantum effects, observable even at room temperature, such as the anomalous quantum Hall effect and Klein tunneling (Geim and Novoselov, 2007; Geim, 2009). A comprehensive discussion of these properties can be found in a series of reviews published recently (Avouris et al., 2007; Geim, 2009; Castro Neto et al., 2009; Zhu et al., 2010). Also, it has been demonstrated that epitaxial few-layer graphene (FLG) samples, containing from two up to tens of graphene layers grown on the C-face of SiC retain some of the outstanding electronic properties of single-layer graphene (Hass et al., 2008; Sprinkle et al., 2009). These properties usually vanish when the C layers are stacked as the typical  $AA$  or  $AB$  planes (Latil and Henrard, 2006); this phenomenon is a consequence of the turbostratic stacking of planes observed in the samples, which result in an effective electronic decoupling of layers (Latil et al., 2007; Lopes dos Santos et al., 2007; Hass et al., 2008a; Shallcross et al., 2008; Varchon et al., 2008).

This outstanding combination of physical properties makes graphene a candidate for a series of potential applications, such as thermally and electrically conductive reinforced composites, sensors, supercapacitors, conductive inks, transparent electrodes

for displays and solar cells, and, especially, as the pillar for the next generation of electronics in high-speed logic and radio frequency devices (Allen et al., 2010; Schwierz, 2010; Zhu et al., 2010).

Chemical modification and functionalization of CNTs and graphene has been used to tailor their interactions with other materials (solvents, polymers, biomolecules), as well as to change their electronic and mechanical properties in a controllable way, opening new horizons for practical applications (Ciraci et al., 2004; Hirsch and Vostrowsky, 2005; Boukhvalov and Katsnelson, 2009a). One example of functionalization that leads to significant potential applications is hydrogenation, carried out by the exposure of the surface of these materials to a source of atomic hydrogen (e.g., from a H<sub>2</sub> plasma). As a result of this exposure, hydrogen atoms are chemisorbed onto the surface, leading to the formation of stable  $sp^3$  hybridized C–H and C–C bonds in a structure that is originally formed by delocalized  $sp^2$  C–C bonding.

Hydrogenation has been used to modify and control the band gap of SWCNTs (Zhang et al., 2006; Zheng et al., 2007) and graphene (Elias et al., 2009; Guisinger et al., 2009; Sessi et al., 2009; Balog et al., 2010), creating new possibilities for their use in future-generation electronics technologies. In the case of CNTs, their surface curvature leads to a partial tetrahedrization of the local bonding configuration, reducing the energy barrier for H adsorption when compared to that onto planar graphite (Ruffieux et al., 2002, 2004). As a result, large amounts of hydrogen can be chemisorbed onto the SWCNT surface, making SWCNTs potential candidates for hydrogen storage media; the storage capacity of SWCNTs is as high as 7 wt% (Nikitin et al., 2008), which is larger than the U.S. DOE 2010 target for on-board H storage systems (6 wt%). This process has

been shown to be reversible (Nikitin et al., 2005); by heating the hydrogenated SWCNTs to a temperature of 200-300°C, the hydrogen is released and the initial properties of the pristine SWCNTs are recovered.

In addition to the applications mentioned above, it has been demonstrated that processing of MWCNTs with a hydrogen plasma at a temperature of 1000 K induces their structural transformation and results in the formation of diamond nanocrystals and nanorods embedded in the walls of the MWCNTs (Sun et al., 2004a, b). The experiments suggest strongly that the atomic hydrogen generated in the H<sub>2</sub> plasma is responsible for this transition; exposing the same material to H<sub>2</sub> and subjecting it to thermal annealing does not lead to any similar structural transition. However, the physicochemical mechanisms responsible for this transition are not yet understood. This hydrogen plasma process provides a promising alternative to producing high-quality diamond films in a controllable way; preliminary experimental results suggest that such diamond synthesis may be possible at temperatures as low as room temperature (Behr and Aydil, 2009). It is well known that diamond has extraordinary properties and it has been considered as “the ultimate engineering material” (May, 2000). Diamond thin films have a broad range of existing and potential technological applications, such as in chemical sensing, nanoelectronics, optics, and field emission displays, among many others, which have been reviewed extensively (May, 2000).

## **1.2 Thesis Objectives and Outline**

This Ph.D. thesis presents an atomic-scale computational analysis of the structural transformations induced by hydrogenation in carbon nanotubes and graphene. The study

addresses two interrelated topics. The first is the structural and morphological transformations undergone by single-walled carbon nanotubes and graphene layers as a result of their exposure to atomic hydrogen and the  $sp^2$ - $sp^3$  bonding transition associated with it. The second is the formation of carbon nanostructures due to inter-shell/interlayer C-C bonding in multi-walled/layered materials, a process in which atomic hydrogen plays a key role in both the synthesis and the stability of the formed structures. The outcomes of this study explain observed phenomena in the body of experiments that have been reported in the literature and generate a series of experimentally testable hypotheses, which can guide future experiments in the field. The findings reported in the present thesis are expected to be of fundamental importance toward designing efficient processes for transforming MWCNTs, few-layer graphene, and amorphous carbon films into carbon-based nanocrystalline structures, as well as for hydrogenating SWCNTs and graphene with a desired and tailored hydrogen surface coverage.

In summary, the specific objectives of the thesis are:

- A fundamental understanding of the structural and morphological changes on SWCNTs and graphene induced by atomic hydrogen chemisorption;
- Analysis of the effect of these structural and morphological changes on the hydrogen storage capacity of SWCNT bundles;
- Investigation of the formation of nanostructures upon creation of inter-shell C-C bonds between adjacent graphene walls in MWCNTs as a function of the relative orientation between individual layers, and its relation to the process of nanodiamond formation upon exposure of MWCNTs to  $H_2$  plasmas; and

- Identification of carbon nanostructures that can be generated by interlayer C-C bonding in twisted bilayer graphene and investigation of the effect of the resulting  $sp^3$  C-C bonding on the electronic structure of this material.

The remaining of this dissertation aims at achieving the above objectives in a consistent and coherent sequence. Toward this end, the rest of this thesis is structured as follows.

A description of the computational techniques employed in the thesis is presented in Chapter 2. A synergistic combination of atomic-scale computational methods, namely, classical Molecular-Dynamics (MD) simulations, Monte Carlo (MC) simulations, and first-principles Density Functional Theory (DFT) calculations were carried out in this study, aiming to obtain detailed information toward a fundamental and quantitative understanding of the material systems under investigation. A general overview of these methods is presented, as well as the implementation details for each method applied to the problems addressed in the thesis.

In Chapter 3, a systematic computational study of the effects of atomic hydrogen chemisorption on the structure and morphology of graphene layers and single-walled carbon nanotubes is presented. The study is based on a combination of classical molecular-dynamics and Monte Carlo simulations of structural and compositional relaxation of the hydrogenated surfaces, employing hydrogen distributions consistent with experimental observations and first-principles calculations. Results are reported for the strains induced on the graphene and the SWCNTs, as a result of  $sp^2$ - $sp^3$  bonding transitions due to atomic H chemisorption, and their dependence on the H surface

coverage,  $\Theta$ , over the entire range  $0 \leq \Theta \leq 1$  and on nanotube diameters and chiralities. Upon hydrogenation, the nanotubes and graphene layers expand and the degree of expansion depends on the hydrogen coverage. There is a critical hydrogen coverage that marks the onset of a structural transition associated with the  $sp^2$ -to- $sp^3$  bonding transition: at lower-than-critical coverage,  $sp^2$  C-C bonding dominates and nanotube swelling/graphene sheet expansion is negligible; at higher-than-critical coverage, however,  $sp^3$  C-C bonding dominates and strains increase monotonically with coverage. Detailed structural analysis of the relaxed hydrogenated surfaces demonstrates a tendency for clustering of hydrogenated and of non-hydrogenated sites; this leads to surface morphologies characterized by ripples, which consist of hills that form due to clustering of hydrogenated sites and are surrounded by valleys appearing through the formation of long chains of non-hydrogenated sites. These features introduce surface roughness that depends on the degree of hydrogenation and reaches its maximum levels at intermediate levels of H coverage. The results reported in this chapter have been published in *Applied Physics Letters* (Muniz et al., 2009a) and in the *Journal of Applied Physics* (Muniz and Maroudas, 2010).

Chapter 4 introduces an analytical model to describe the effect of carbon nanotube swelling upon hydrogenation on the hydrogen storage capacity of single-walled CNT bundles; the model is properly parameterized using atomistic calculations for the relationship between CNT swelling and the degree of hydrogenation as discussed in Chapter 3. The model generates experimentally testable hypotheses, which can be used to explain the inconsistency of hydrogen storage capacities reported for CNTs and the experimentally observed non-uniformity of hydrogenation of CNT bundles (Khare et al.,

2002a,b; Ruffieux et al., 2002, 2004; Nikitin et al., 2005, 2008; Tokura et al., 2008). The results reported in this chapter have been published in *Applied Physics Letters* (Muniz et al., 2009b).

In Chapter 5, a systematic analysis is presented of the nanocrystalline structures generated due to inter-shell C-C bonding between adjacent concentric graphene walls of multi-walled carbon nanotubes. The analysis combines a comprehensive exploration of the entire parameter space determined by the geometrical characteristics of the individual graphene walls comprising the MWCNT with first-principles density functional theory calculations of inter-shell C-C bonding and structural relaxation by molecular-dynamics simulation of the resulting nanocrystalline structures. We find that these structures can provide seeds for the nucleation of the cubic-diamond and hexagonal-diamond phase in the form of nanocrystals embedded in the MWCNTs. The resulting lattice structure is determined by the chirality and relative alignment of adjacent graphene walls in the MWCNT. These crystalline phases are formed over the broadest range of nanotube diameters and for any possible combination of zigzag, armchair, or chiral configurations of graphene walls. The key parameter that determines the size of the generated nanocrystals is the chiral-angle difference between adjacent graphene walls in the MWCNT. The results reported in this chapter have been published in *Physical Review B* (Muniz et al., 2009c).

In Chapter 6, it is demonstrated that a class of novel interlayer-bonded structures can be generated starting from twisted bilayer graphene in the limit of twist rotation angles  $\theta \rightarrow 30^\circ$ ; these structures are stabilized by chemisorbed H atoms and consist of caged fullerene-like configurations embedded within the graphene bilayers. For small

deviations of this angle  $\theta$ , leading to commensurate bilayers, analogous nanostructures can be generated. The electronic structure of these novel nanomaterials reveals that some of the unique electronic properties of pristine single-layer graphene are partially retained after creation of the interlayer C-C bonds, in spite of the introduction of  $sp^3$  bonding. A manuscript reporting the results of this chapter is in preparation to be submitted for publication in a leading physics journal.

A summary of the most important results and conclusions of this thesis, as well as suggestions for future research in the field, are presented in Chapter 7. Finally, Appendix A gives a detailed description of the interatomic potential employed in the classical MD and MC calculations reported in the thesis, as well as results of several tests conducted to validate the quantitative accuracy of the potential for the specific purposes of the thesis.

## CHAPTER 2

### COMPUTATIONAL METHODS

#### 2.1 Introduction

Computational simulation is an extremely useful tool for predicting materials response and understanding the underlying mechanisms occurring at the atomic scale; nowadays, computer simulation is considered as an important and essential complement to experimental and theoretical studies. A broad suite of methods has been used traditionally in molecular simulation, capturing different ranges of time and length scales and being able to describe a variety of physical phenomena. In the present thesis, three classes of computational methods have been employed: classical molecular-dynamics (MD) and Monte Carlo (MC) simulations (Allen and Tildesley, 1989; Leach, 2001; Frenkel and Smit, 2002; Rapaport, 2004), and first-principles density functional theory (DFT) calculations (Koch and Holthausen, 2001; Martin, 2004). A brief review of these methods is presented in the following sections, including some details of their implementation to address the problems of relevance in this thesis; the purpose of this review is not to present a full treatise of the methods, but simply to introduce the basic concepts involved in each one of these techniques.

#### 2.2 Molecular-Dynamics Simulations

Molecular-Dynamics (MD) simulation is a powerful and versatile tool, used to obtain dynamical information about the structure of individual molecules and condensed

phases at atomic scale. Traditionally, it is used for monitoring short-term (ns-scale) and predicting structural parameters of molecules and bulk phases, measuring mechanical and transport properties in solids, liquids and gases, predicting phase equilibria and phase transitions, studying fluid flow in narrow channels, investigating reaction/diffusion mechanisms, among many others possible applications. In this thesis, MD simulations are employed for the computation of optimized structures of SWCNTs, MWCNTs, graphene planes, few-layer graphene and crystalline carbon phases, in both pristine and hydrogenated states.

The MD method consists of integrating the classical equations of motion for a  $N$ -body system of interacting particles (Newton's 2<sup>nd</sup> law),

$$m_i \frac{d^2 \mathbf{r}_i}{dt^2} = \sum_{\substack{j=1 \\ j \neq i}}^N \mathbf{F}_{ij}, \quad \text{for } i = 1, 2, 3, \dots, N \quad (2.1)$$

where  $m_i$  and  $\mathbf{r}_i$  are the mass and position vector for each particle  $i$ ,  $t$  is the time, and  $\mathbf{F}_{ij}$  is the force acting on particle  $i$  by particle  $j$  (being  $\mathbf{F}_{ij} = \mathbf{F}_{ji}$ ), which is given by the derivative of the interatomic potential energy  $U(r_{ij})$ ,

$$\mathbf{F}_{ij} = -\frac{\partial U(r_{ij})}{\partial r_{ij}}. \quad (2.2)$$

where  $r_{ij}$  is the distance between atoms  $i$  and  $j$ . The integration of the above system of  $3N$  2<sup>nd</sup>-order nonlinear ordinary differential equations, starting from an specified initial configuration  $\mathbf{r}_i(t=0)$ , gives the trajectories  $\mathbf{r}_i(t)$  for each particle, and detailed dynamics can be monitored directly; thermodynamic, transport, and mechanical properties can be obtained by time-averaging over the generated trajectories. Various numerical methods are available for integrating such systems of ordinary differential equations; typically, MD simulations employ explicit second-order methods, such as the Verlet and leapfrog-

Verlet algorithms, or higher-order predictor-corrector methods (Rapaport, 2004). For the present work, the widely used leapfrog-Verlet method was chosen, due to its simplicity of implementation, computational efficiency, and accuracy.

In the implementation of classical molecular-dynamics simulations, it is of crucial importance to choose an appropriate and reliable interatomic potential function, which is capable of describing accurately the interactions in the material system under consideration. A wide variety of interatomic potentials is available in the literature, several of which have been implemented in available computational packages; these potentials can be used to describe interatomic interactions in a broad class of material systems. These potentials are empirical or semi-empirical, containing a set of parameters that are usually estimated by fitting experimental data and/or results from accurate *ab initio* quantum mechanical calculations.

A suitable interatomic potential for the problems on carbon nanostructures addressed in this thesis is the Adaptive Intermolecular Reactive Empirical Bonding Order (AIREBO) potential developed by Stuart and coworkers (Stuart et al., 2000). This potential has been used extensively for describing the interactions in solid carbon and hydrocarbon molecules. This potential is an improvement over the original Reactive Empirical Bonding Order (REBO) potential developed by Brenner (Brenner, 1990; Brenner et al., 2002), which was based on the concept of the bond-order function that was introduced by Tersoff and includes many-body effects into an effectively two-body (pair) potential (Tersoff, 1988).

AIREBO generates a typical reactive force field: it treats the formation and dissociation of covalent bonds, as well as the resulting changes in the atomic

hybridization and coordination number in an empirical manner. This version of the potential also accounts for the treatment of long-range interactions (van der Waals forces), which is of fundamental importance in the study of graphite, graphene bilayers, MWCNTs and SWCNT bundles.

The AIREBO potential has the functional form

$$U = \sum_i \sum_{j \neq i} \left[ V_R(r_{ij}) - b_{ij} V_A(r_{ij}) + V_{vdw}(r_{ij}) + \sum_{k \neq i, j, l \neq i, j, k} V_{ijkl}^{tors} \right], \quad (2.3)$$

where  $r_{ij}$  is the distance between atoms  $i$  and  $j$ ,  $V_R(r_{ij})$  and  $V_A(r_{ij})$  denote pair-additive repulsive and attractive interactions, respectively, and  $b_{ij}$  is the bond-order function. These two terms alone constitute the original REBO potential. The terms  $V_{vdw}(r_{ij})$  and  $V^{tors}$  correspond to the long-range interactions and torsional potential, respectively, introduced by Stuart and coworkers in the AIREBO version of the force field (Stuart et al., 2000).

Many-body effects are introduced by the bond-order function  $b_{ij}$ , which depends on the local atomic coordination, bond angles, and conjugation effects. Quantum mechanical effects are not accounted for explicitly in the description: hybridized states and conjugation are described implicitly by the geometry of the atomic configurations (Stuart et al. 2000; Brenner et al., 2002). A comprehensive description of the functional forms of each term in Eq. (2.3), the procedure employed in the parametrization of the potential, as well as the numerical values for all the parameters involved have been given in the original articles (Stuart et al., 2000; Brenner et al., 2002).

In this thesis, the AIREBO potential was tested for its quantitative accuracy through systematic comparisons with first-principles DFT calculations for the structure

and properties of bulk crystalline carbon phases and carbon nanotubes, as well as for the chemisorption of H atoms onto CNTs. Some of the DFT results that were used in these comparisons have been taken from the literature, while others have been obtained by our own DFT calculations. This systematic study is presented in Appendix A of this thesis.

Equation (2.1) corresponds to the conventional MD simulation that represents a system of constant number of atoms at constant volume and total energy (i.e., in the microcanonical ensemble, NVE). In practical situations, it is commonly desired to carry out simulations in other ensembles, for example, at constant temperature and/or pressure, which is typical of laboratory experiments. The MD method can be extended easily to simulate systems in different ensembles, such as the NVT (isochoric-isothermal), NPT (isobaric-isothermal), and NPH (isobaric-isoenthalpic) ensembles. There is a series of different approaches used to simulate systems in such ensembles; some of them are quite simple, such as implementing a velocity rescaling procedure for controlling the temperature, and others are more elaborate, using extended equations of motion (in Lagrangian form) to emulate the coupling of the system to a heat/pressure bath. A comprehensive discussion of different approaches to perform MD simulations at NVT, NPT, and NPH ensembles can be found in standard simulation textbooks (Allen and Tildesley, 1989; Frenkel and Smit, 2002; Rapaport, 2004).

In the problems addressed in this thesis, the MD simulations were performed in the isothermal-isobaric (NPT) ensemble. For temperature and pressure control in the simulations, the Berendsen thermostat/barostat (Berendsen et al., 1984) was employed. This thermostat/barostat is based on a weak coupling of the system to an external bath at constant temperature  $T_0$  and pressure  $P_0$ . The equations of motion are modified in order to accomplish this coupling, such that the rate of change of temperature is given by

$$\frac{dT}{dt} = \frac{1}{\tau_T}(T_0 - T), \quad (2.4)$$

where  $\tau_T$  is a time constant, which represents the strength of the coupling between the system and the thermal bath, and  $T$  is the temperature of the system. The values for this parameter can be optimized; the larger the value of the parameter the weaker the coupling. In the computations presented in the thesis, a value of  $\tau_T = 0.1 \text{ ps}^{-1}$  proved to be adequate. Berendsen and coworkers (Berendsen et al., 1984) showed that in order to accomplish this coupling, velocities must be rescaled at each time step  $k$ :  $\mathbf{v}_k = \lambda \cdot \mathbf{v}_{k-1}$ , where the parameter  $\lambda$  is evaluated according to the expression

$$\lambda = \left[ 1 + \frac{\Delta t}{\tau_T} \left( \frac{T_0}{T} - 1 \right) \right]^{1/2}, \quad (2.5)$$

where  $\Delta t$  is the time step used in the integration of the equations of motion. In an analogous manner, for the coupling of the system to a pressure bath, the equations of motion are modified such that the rate of change of pressure is given by

$$\frac{dP}{dt} = \frac{1}{\tau_P}(P_0 - P), \quad (2.6)$$

where  $\tau_P$  is the coupling parameter for pressure control, analogous to  $\tau_T$  for temperature control. Similarly, the particle coordinates  $\mathbf{x}$  and the cell dimensions  $\ell$  are rescaled at each time step:  $\mathbf{x} = \mu \mathbf{x}$  and  $\ell = \mu \ell$  respectively, where the parameter  $\mu$  is calculated as:

$$\mu = \left[ 1 - \beta \frac{\Delta t}{\tau_P} (P_0 - P) \right]^{1/3} \quad (2.7)$$

with  $\beta$  being the isothermal compressibility. Usually,  $\tau_P$  and  $\beta$  are combined to a single constant, and optimized as discussed for  $\tau_T$ . This procedure can be applied either isotropically (where the scaling parameter  $\mu$  is the same in all directions) or anisotropically.

## 2.3 Monte Carlo Simulations

Monte Carlo (MC) simulation is the generic term used for a class of stochastic computational methods, named after the famous European casino. This method has been used extensively not only for modeling molecular systems but also in other areas of physics, as well as in statistics, biology, finance and business, among other fields.

In atomic-scale simulations, the basic idea behind this method is to sample the configurational space for a system stochastically; positions and/or orientation and/or conformation of particles/molecules are changed randomly throughout the system in an iterative scheme, contrary to the deterministic nature of molecular-dynamics simulations, as discussed in Section 2.2. Consequently, the MC method does not give a true dynamical description of the system; however, it is very efficient in the computation of equilibrium properties and equilibrium states reached through slow kinetic processes. Optimally, this type of sampling should generate a larger number of states that are more likely to occur, spending less time on exploring low-probability states; this is the essence of the so called “importance sampling” schemes. The first such scheme to be devised and also the most commonly used in molecular simulations is the Metropolis scheme, developed by Metropolis and coworkers in the 1950’s (Metropolis et al., 1953). In this scheme, the probability of visiting a state  $\mathbf{r}^N$  is proportional to the Boltzmann factor  $\exp(-\beta U(\mathbf{r}^N))$ , where  $\beta = (k_B T)^{-1}$ , where  $k_B$  is the Boltzmann constant and  $T$  is the temperature.

The Metropolis MC method consists of taking the system at a state  $\mathbf{r}_k^N$ , computing its energy  $U(\mathbf{r}_k^N)$ , and selecting an event/move randomly, toward a subsequent state  $\mathbf{r}_{k+1}^N$ ; the energy for this new state  $U(\mathbf{r}_{k+1}^N)$  is evaluated and the move is accepted or rejected

based on the energy difference between the current and subsequent states. The probability of acceptance  $p(k \rightarrow k+1)$  is given by

$$p(k \rightarrow k+1) = \min(1, \exp\{-\beta[U(\mathbf{r}_{k+1}^N) - U(\mathbf{r}_k^N)]\}). \quad (2.8)$$

At each step, at least two random numbers are generated from a uniform distribution in the interval  $[0,1]$ : one (or more) is used to select a move and the other one to implement the Metropolis criterion, Eq. (2.8); if the random number is larger than the probability, the move is accepted, otherwise it is rejected. The procedure is applied iteratively until equilibration is achieved, when the desired properties of the system can be computed.

The Metropolis algorithm is the most commonly used one for sampling states in configurational space, generating states in the canonical ensemble, and generating states in different ensembles after simple modifications (Leach, 2001; Frenkel and Smit, 2002). Additional sampling techniques exist (called biased Monte Carlo methods), in which the moves and probabilities of acceptance are biased according to additional rules; in general, such techniques are used to enhance the performance and efficiency of MC simulations in certain applications (Leach, 2001; Frenkel and Smit, 2002).

In Chapter 3 of the thesis, the MC method is employed in conjunction with MD simulations, as part of a more general procedure termed “compositional relaxation”, in order to determine the energetically most favorable arrangements of H atoms chemisorbed onto graphene and SWCNT surfaces. The corresponding methodological details are described properly in Chapter 3.

## 2.4 Density Functional Theory Calculations

Density Functional Theory is a well established method for solving interacting many-body problems, and it is used widely for electronic structure calculations in condensed phases. It can be employed to predict structural, electronic, magnetic, and mechanical properties of molecules, nanoclusters, and periodic solids, such as optimized configurations, formation energies, activation barriers for kinetic processes, electronic band structures, and phonon dispersion curves for solids, among many others.

The DFT method is based on the concept of energy as a functional of the electron density distribution (Kohn, 1999); this is fundamentally different from the Hartree-Fock approach that is used traditionally in electronic structure calculations and aims at solving the Schrödinger equation for the many-electron wavefunctions. The development of the DFT method started with the demonstration by P. Hohenberg and W. Kohn (Hohenberg and Kohn, 1964) that for a given system of interacting particles under the influence of an external potential  $V_{ext}(\mathbf{r})$ , the potential is a unique functional of the electron density distribution  $n(\mathbf{r})$ ; consequently, since  $V_{ext}(\mathbf{r})$  contributes to the Hamiltonian, all the properties of the system can be expressed as functionals of  $n(\mathbf{r})$ . One year later, W. Kohn and L. J. Sham (Kohn and Sham, 1965) proposed a feasible way to apply this concept to the determination of electronic structure; this was done by the introduction of a non-interacting auxiliary system (easier to solve) to predict the properties of the true interacting system. According to this approach, the ground state energy  $E$  of the system can be written as a functional of the electron density distribution  $n(\mathbf{r})$ ,

$$E[n(\mathbf{r})] = \frac{1}{2} \sum_i^N \int d^3r |\nabla \psi_i(\mathbf{r})|^2 + \int d^3r V_{ext}(\mathbf{r})n(\mathbf{r}) + \frac{1}{2} \int d^3r d^3r' \frac{n(\mathbf{r})n(\mathbf{r}')}{|\mathbf{r} - \mathbf{r}'|} + E_{XC}[n(\mathbf{r})]. \quad (2.9)$$

Atomic units are used in this equation ( $\hbar = m_e = e = 1$ ). The first term accounts for the kinetic energy of a non-interacting particle system; the second term represents the interaction of electrons with the external potential  $V_{ext}(\mathbf{r})$  due to the atomic nuclei and other external fields; the third term, which can be defined as  $E_H[n(\mathbf{r})]$ , arises from the electron-electron classical Coulombic interactions; the last term,  $E_{XC}[n(\mathbf{r})]$ , defined as the exchange-correlation functional, accounts for all the non-classical effects not described by the previous terms. The family of functions  $\psi_i(\mathbf{r})$  are called Kohn-Sham orbitals for  $i = 1, \dots, N$  electrons, which correspond to the eigenfunctions of the auxiliary system of non-interacting electrons under an average effective potential, as described by the eigenvalue problem

$$\left[ -\frac{1}{2}\nabla^2 + V_{ext}(\mathbf{r}) + V_H[n(\mathbf{r})] + V_{XC}[n(\mathbf{r})] \right] \psi_i(\mathbf{r}) = \varepsilon_i \psi_i(\mathbf{r}), \quad (2.10)$$

where  $V_m[n(\mathbf{r})]$ , for  $m = \{H, XC\}$ , are potentials of the corresponding functionals  $E_m[n(\mathbf{r})]$ , defined as

$$V_m[n(\mathbf{r})] = \frac{\delta E_m[n(\mathbf{r})]}{\delta n(\mathbf{r})}. \quad (2.11)$$

The electronic density  $n(\mathbf{r})$  is then expressed in terms of Kohn-Sham eigenstates  $\psi_i(\mathbf{r})$  according to

$$n(\mathbf{r}) = \sum_i^N |\psi_i(\mathbf{r})|^2. \quad (2.12)$$

Spin polarization is not taken into account in equations (2.9)-(2.12), but the methodology can be easily extended to account for this, by assigning electron density distributions for electrons with spins up  $n^\uparrow(\mathbf{r})$  and down  $n^\downarrow(\mathbf{r})$  instead of a single electron density distribution  $n(\mathbf{r})$ .

The minimization of the energy functional given by Eq. (2.9) gives the ground-state energy for the system; in summary, the problem consists of finding the electron density distribution  $n(\mathbf{r})$  that minimizes  $E[n(\mathbf{r})]$ . The minimization problem needs to be solved self-consistently, since neither  $\psi_i(\mathbf{r})$  nor  $n(\mathbf{r})$  is known *a priori*; this scheme forms the basis for most of the modern DFT software packages (Kresse and Furthmuller, 1996; Giannozzi et al., 2009), and algorithms for solving the problem are discussed in detail in the literature (Payne et al., 1992; Nogueira et al., 2003; Martin, 2004).

This approach would give the exact solution to the problem if an exact expression for the exchange-correlation functional were available; the accuracy of the results is strongly linked to the quality of the approximations made for this term. Different approximations have been proposed for  $E_{XC}[n(\mathbf{r})]$  with different degrees of accuracy and simplicity. The simplest approach that has been used successfully in condensed-matter problems is the so called Local Density Approximation (LDA); the corresponding expression for the exchange-correlation functional is

$$E_{XC}^{LDA}[n(\mathbf{r})] = \int d^3r n(\mathbf{r}) \varepsilon_{XC}^{HEG}(n), \quad (2.13)$$

where  $\varepsilon_{XC}^{HEG}(n) = \varepsilon_X^{HEG}(n) + \varepsilon_C^{HEG}(n)$  is the exchange-correlation energy density for a homogeneous electron gas. For a uniform electron gas, the exchange energy,  $\varepsilon_X^{HEG}(n)$ , has an analytical form, while for the correlation energy  $\varepsilon_C^{HEG}(n)$ , different parameterizations have been proposed, such as the one by Perdew and Zunger (Perdew and Zunger, 1981), employed in some calculations in this thesis.

A further development attempting to correct deficiencies of the LDA, is the so called Generalized Gradient Approximation (GGA), which employs in the estimation of

exchange-correlation effects not only the electron density but also its gradient, in order to account for the non-homogeneity of electron density in real material systems:

$$E_{XC}^{GGA}[n(\mathbf{r})] = \int d^3r n(\mathbf{r}) \varepsilon_{XC}(n, |\nabla n|) \quad (2.14)$$

Different expressions and parameterizations have been proposed for  $\varepsilon_{XC}(n, |\nabla n|)$  within the GGA, such as the one by Perdew, Burke and Ernzerhof (Perdew, Burke and Ernzerhof, 1996), which is widely known as PBE and employed in some calculations presented in this thesis.

In spite of its simplicity, LDA performs reasonably well in the prediction of structures for solids and molecules in their ground state. The use of LDA leads systematically to overbinding in molecules, resulting in shorter bond lengths and higher binding energies than the actual ones (Koch and Holthausen, 2001; Nogueira et al., 2003; Staroverov et al., 2004). In general, GGA leads to a much better estimation of geometries and energies compared to LDA; the relative error in these parameters is not as systematic as in LDA, but binding is usually underestimated (Koch and Holthausen, 2001; Nogueira et al., 2003; Staroverov et al., 2004).

When dealing with periodic solids and supercells, the standard tool for faster and accurate electronic structure calculations is the use of plane-wave expansions for the Kohn-Sham eigenstates, in conjunction with the use of pseudopotentials to represent the ionic cores (Kresse and Furthmuller, 1996; Nogueira et al., 2003; Martin, 2004; Giannozzi et al., 2009). The use of plane waves takes advantage of the system periodicity, and simplifies the calculational procedure. However, when plane waves are employed, it is of practical importance to remove the core electrons of the atoms from the calculations; the reason is the large number of plane waves that would be required to

describe the wavefunction close to the nucleus, due to the presence of typically sharp oscillations in this region. This task can be achieved by using ultrasoft pseudopotentials (Vanderbilt, 1990): the basic idea is to generate an effective potential felt by the valence electrons, which includes both the nuclear attraction and core electron repulsion. This is a valid approach, considering that the inner electrons do not affect significantly the bonding of atoms; only the valence electrons atoms are used in the calculations, which is sufficient to describe chemical bonding and material properties. A series of approaches has been proposed to generate reliable and computationally efficient pseudopotentials, which has been reviewed in the literature (Nogueira et al., 2003; Martin, 2004).

In this thesis, all the calculations presented are based on either LDA or GGA exchange-correlation functionals and they employ ultrasoft pseudopotentials (Vanderbilt, 1990) and wavefunction expansion in plane waves, as implemented in the computational packages VASP (Kresse and Furthmuller, 1996) and QUANTUM ESPRESSO (Giannozzi et al., 2009). For the optimization of geometries, i.e., atomic configurations, DFT calculations are coupled to either a *quasi*-Newton optimization method or to a molecular-dynamics routine (Giannozzi et al., 2009), where convergence is sought according to energy, force, and stress criteria.

## **2.5 Summary**

In this chapter, the computational methods employed in this thesis were discussed briefly. The following chapters will provide additional details on the application of these methods to address the problems of interest. In Chapter 3, molecular-dynamics and Monte Carlo methods are used to obtain optimized structures of pristine and

hydrogenated carbon nanotubes and graphene layers. In Chapters 5 and 6, classical molecular-dynamics simulations and first-principles DFT calculations are used to predict the geometry (relaxed atomic configurations) and electronic structure of carbon phases generated upon interlayer bonding in multilayered carbon materials (MWCNT and FLG).

## CHAPTER 3

# HYDROGENATION EFFECTS ON THE STRUCTURE AND MORPHOLOGY OF SINGLE-WALLED CARBON NANOTUBES AND GRAPHENE

### 3.1 Introduction

As discussed in Chapter 1, carbon-based nanostructured materials, such as fullerenes, single-walled carbon nanotubes (SWCNTs), and graphene, have been studied extensively over the past two decades because the unique combination of their chemical and physical properties may enable numerous technological applications. These properties can be modified and controlled by chemical functionalization, such as hydrogenation, that can be achieved by exposure of the surface to a source of atomic hydrogen, e.g., a H<sub>2</sub> plasma. Hydrogen atoms are chemisorbed onto the carbon surfaces of these materials, introducing  $sp^3$  hybridized C-H and C-C bonds in a structure that is originally formed by delocalized  $sp^2$  C-C bonding. This locally induced  $sp^2$ -to- $sp^3$  bonding transition leads to the outward relaxation of carbon atoms from the surface, resulting in structural changes and defect formation, which affect the materials' electronic properties. A comprehensive body of experimental studies on hydrogenation (and/or deuteration) of (0001) graphite surfaces (Waqar et al., 2001; Zecho et al., 2002; Hornekær et al., 2006a,b, 2007; Andree et al., 2006), graphene layers (Ryu et al., 2008; Elias et al., 2009; Guisinger et al., 2009; Balog et al., 2009, 2010; Sessi et al., 2009; Luo et al., 2009), and SWCNTs (Khare et al., 2002a,b; Ruffieux et al., 2002, 2004; Nikitin et al., 2005, 2008; Zhang et al., 2006; Buchs et al., 2007a,b; Zheng et al., 2007; Tokura et

al., 2008) have been reported, as well as numerous theoretical and computational studies, which have helped to interpret the experimental findings and obtain a better fundamental understanding of the hydrogenation process (Jeloaica and Sidis, 1999; Bauschlicher, 2000; Bauschlicher, 2001; Yildirim et al., 2001; Bauschlicher and So, 2002; Ferro et al., 2002; Gülseren et al., 2002; Sha and Jackson, 2002; Sha et al., 2002; Volpe and Cleri, 2003; Allouche et al., 2005, 2006; Park et al., 2005; Rougeau et al., 2006; Roman et al., 2007, 2009; Sofo et al., 2007; Boukhvalov et al., 2008, 2009a,b; Cuppen and Hornekær, 2008; Ferro et al., 2008,2009; Casolo et al., 2009; Kerwin and Jackson, 2008; Khazaei et al., 2009; Nikitin et al., 2009; Muniz et al., 2009ab, 2010; Šljivančanin et al., 2009; Chernozatonskii and Sorokin, 2010;Wu et al., 2010).

Hydrogenation of SWCNTs and graphene has various potentially significant technological applications. It can be used to modify and control the band gap of SWCNTs (Zhang et al., 2006; Zheng et al., 2007) and graphene, (Elias et al., 2009; Guisinger et al., 2009; Sessi et al., 2009; Balog et al., 2010), creating new possibilities for their application in electronics. Another important application is the use of these materials as hydrogen storage media. Experimental studies (Ruffieux et al., 2002, 2004; Nikitin et al., 2005, 2008; Tokura et al., 2008; Yurum et al., 2009) have resulted in inconsistent values for the maximum storage capacity that can be achieved by exposure of SWCNTs to atomic H; surface coverages from ~ 20 % up to ~ 100 % have been reported (corresponding to a storage capacity of ~ 1.5 wt% up to ~ 7.7 wt%). Different explanations have been offered for these discrepancies, such as sample preparation, processing conditions, and presence of impurities. It is demonstrated in the Chapter 4 of this thesis, that the density of arranging SWCNTs into nanotube bundles, as well as the

SWCNTs' individual diameters and chiralities also can affect the total amount of H that can be stored as a result of the swelling of SWCNTs upon their hydrogenation – effect which by the way, is discussed in details in this chapter. However, saturation coverages much lower than 100% have been typically observed in the hydrogenation of the basal plane of graphite and of graphene. Zecho and coworkers (Zecho et al., 2002) have reported a maximum coverage of  $40\pm 20\%$  for graphite and various other experimental and computational studies have suggested consistently an upper limit of  $\sim 50\%$  (Hornekær et al., 2006b; Luo et al., 2009; Allouche et al., 2005, 2006).

Computational studies have demonstrated that the mechanical (Pei et al., 2010), electronic (Chernozatonskii and Sorokin, 2010; Gülseren et al., 2002; Park et al., 2005), and magnetic (Ferro et al., 2008; Casolo et al., 2009; Wu et al., 2010) properties of hydrogenated SWCNTs and graphene sheets are dependent on the patterns formed by the chemisorbed hydrogen atoms distributed on the surface. For the case of graphene and graphite (0001) surfaces, a fundamental understanding of the most likely hydrogen distribution patterns has been obtained by a synergistic combination of experiments and first-principles density functional theory (DFT) calculations (Zecho et al., 2002; Hornekær et al., 2006a,b, 2007; Andree et al., 2006; Rougeau et al., 2006; Roman et al., 2007; Casolo et al., 2009; Šljivančanin et al., 2009). Scanning tunneling microscopy (STM) images of these surfaces at low H surface coverages show the formation of preferred pairs and small clusters of hydrogenated atoms. The most abundant pairs observed consist of hydrogenated atoms in *ortho* and *para* positions within the same hexagonal ring, as well as other dimers extended to more distant neighbors, as identified by targeted DFT calculations in conjunction with the corresponding simulated STM

images (Hornekær et al., 2006a, 2007; Khazaei et al., 2009). At higher surface coverages, larger continuous clusters of hydrogenated atoms are observed in the STM images; continuous chains of non-hydrogenated atoms around the hydrogenated clusters also have been observed.

A comprehensive set of DFT calculations demonstrated that the formation of these favorable structures, i.e., pairs and clusters of hydrogenated atoms, is the result of a mechanism called preferential sticking (Hornekær et al., 2006a,b, 2007; Rougeau et al., 2006; Roman et al., 2007; Boukhvalov and Katsnelson, 2009a; Casolo et al., 2009; Šljivančanin et al., 2009). The approach used in these studies consisted of taking a structure with one chemisorbed H atom and determining the binding energies and energy barriers for the chemisorption onto the surface of additional H atoms in the vicinity of the original chemisorbed H atom. These calculations showed that the binding energies for chemisorption of a second H atom are site-dependent. This dependence arises from a combination of structural and electronic effects induced by the chemisorption of new atoms (Roman et al., 2007; Casolo et al., 2009; Boukhvalov and Katsnelson, 2009a; Šljivančanin et al., 2009). In summary, additional chemisorption events that preserve the existence of delocalized  $sp^2$  bonds and lead to minimal additional straining/deformation of the structure are the most likely to occur. In addition, the calculations showed that the presence of chemisorbed atoms onto the carbon surface also affects significantly the energy barriers for the adsorption of one or more additional H atoms. The favorable sites in terms of binding energies also are characterized by lower barriers for the chemisorption of an additional H atom than those for chemisorption onto a pristine surface. For graphite/graphene surfaces, adsorption at the *para* position within the same

ring is barrierless; adsorption at the *ortho* position has a barrier of  $\sim 0.1$  eV, which is lower than those for adsorption at a *meta* position or onto the pristine surface – this is the reason for the predominance of *para* dimers under low coverages, as observed in experiments (Hornekær et al., 2006a,b, 2007; Andree et al., 2006; Balog et al., 2009). Chemisorption also can occur at the other sites, since the difference in the energy barriers is not very high. However, these H atoms are very likely to move to a more favorable position on the surface; for example, the activation barrier for diffusion from a *meta* to an *ortho/para* position within the same ring is  $\sim 0.5$  eV (Hornekær et al., 2006a), and similar barrier heights have been calculated for diffusion from other energetically non-favorable to favorable sites (Cuppen and Hornekær, 2008; Šljivančanin et al., 2009). However, isolated H atoms on the surface do not tend to diffuse throughout the surface, since the activation barrier for surface diffusion is  $\sim 1.14$  eV in this case (Hornekær et al., 2006a), while the barrier for desorption is  $\sim 0.9$  eV; consequently, at high temperature, H atoms prefer to desorb instead of diffusing. The combination of these kinetic factors explains the formation and stability of the clusters of hydrogenated atoms observed in the experiments; the sticking probability of an incoming H atom is higher for adsorption onto certain specific sites and when an energetically favorable and stable pair/cluster is formed, further diffusion is not likely to occur.

It is expected that the above findings on the hydrogenation of graphite/graphene also hold for SWCNTs, considering the same nature of C-C bonding in both cases. DFT studies (Bauschlicher, 2000; Buchs et al., 2007; Chang et al., 2008; Nikitin et al., 2009) have shown that in the low-coverage limit, certain pairs of hydrogenated atoms have higher binding energies than others, and these pair configurations are completely

analogous with those observed for graphene. Surface curvature affects energy barriers and binding energies (Yildirim et al., 2001; Gülseren et al., 2002; Boukhvalov and Katsnelson, 2009b), but the qualitative trends remain the same. This preference for adsorption at specific sites in SWCNTs also has been observed for other functionalizing species, such as fluorine and silyl radicals (Bauschlicher, 2000; Chang et al., 2008). Hydrogenated SWCNTs at higher surface coverages also have been investigated by DFT (Bauschlicher, 2001; Bauschlicher and So, 2002; Gülseren et al., 2002; Volpe and Cleri, 2003; Park et al., 2005), mainly by using regular patterns for the H distribution on the surface. In summary, these calculations have shown that distributions where chains of hydrogenated atoms (and, consequently, chains of conjugated  $sp^2$  C-C bonds) are aligned with the SWCNT axis, maximizing the number of conjugated  $sp^2$  bonds, lead to more stable structures than distributions that result in a larger fraction of non-delocalized  $sp^2$  bonds. For SWCNTs of small radius, H distributions where the chains of hydrogenated atoms are aligned around the circular section of the tube (i.e., along the polar angular coordinate axis of a cylindrical-coordinate system) are not as stable as the ones mentioned above; this is because the larger surface curvature induces some distortion on the bonds, reducing the overlapping of  $p$  orbitals and weakening the conjugation effects (Bauschlicher, 2001; Bauschlicher and So, 2002). Bauschlicher and So (Bauschlicher and So, 2002) found that the energetically most favorable structures have the hydrogen atoms running along the tube axis rather than around the tube and are characterized by delocalized bonding also along the length of the tube.

However, no experimental results on the chemisorbed H distribution in hydrogenated SWCNTs are available that are as detailed as the computational results

discussed above. Buchs and collaborators (Buchs et al., 2007a, b) have reported STM images of hydrogenated SWCNTs at very low H coverages, showing the formation of small “hillocks” or bumps around each chemisorbed site, as expected due to the local  $sp^2$ - $sp^3$  bonding transition; however, the experimental resolution was not enough to identify the types of structures/pairs formed by hydrogenated carbon sites. Effects of hydrogenation at higher coverages on the overall structure of SWCNTs also have been reported. Experiments have demonstrated that SWCNTs swell upon hydrogenation (Zhang et al., 2006; Nikitin et al., 2008), as a result of the strain and deformation induced on their structure by the  $sp^2$ -to- $sp^3$  bonding transition; atomic force microscopy images of samples before and after their exposure to atomic H indicated an increase in the diameters of SWCNTs upon hydrogenation. Also, it was observed that when SWCNTs are exposed to atomic H for longer periods of time and/or under harsher processing conditions, they undergo decohesion through bond cleavage in the direction perpendicular to the nanotube axis, which leads to their decomposition under continuous treatment (Zhang et al., 2006).

The purpose of the computational study in this chapter is to contribute to a fundamental understanding of the structural and morphological changes resulting from the hydrogenation of graphene layers and SWCNTs over the entire range of surface coverages toward a comprehensive picture of these hydrogenation effects. Our computational approach is based on the calculation and detailed characterization of an ensemble of relaxed structures of hydrogenated graphene layers and SWCNTs using classical molecular-dynamics and Monte Carlo simulations and employing hydrogen distributions that are consistent with those observed experimentally and predicted by first-principles calculations. The use of a classical force field in this study enables the

investigation of hydrogenation effects on the structures and morphologies of SWCNTs and graphene over larger spatial domains than those that can be studied based on first-principles calculations; most of the theoretical studies in the literature have been based on first-principles DFT calculations, and, therefore, limited to the analysis of local effects and the study of small-scale domains or periodically repeated patterns. The computational methodology employed in the present study is described in Section 3.2. Our results for the distribution of chemisorbed hydrogen on the hydrogenated surfaces and for the structure and morphology of the hydrogenated graphene and SWCNTs are presented and discussed in Sections 3.3 and 3.4. The main conclusions are summarized in Section 3.5.

## **3.2 Methodology**

### **3.2.1 Structural Relaxation**

The present study places emphasis on the determination and detailed structural characterization of the relaxed structures of hydrogenated graphene and SWCNTs. The main parameter of the study is the H surface coverage,  $\Theta \equiv N_{\text{H}}/N_{\text{C}}$ , where  $N_{\text{H}}$  is the number of hydrogenated carbon atoms (assuming that only one H atom is chemisorbed onto each site) and  $N_{\text{C}}$  is the total number of carbon atoms on the surface, i.e.,  $0 \leq \Theta \leq 1$ ; the relaxed structure and morphology of graphene and SWCNTs are examined as functions of  $\Theta$  in order to explore the corresponding effects of the degree of hydrogenation. Also, only one-sided hydrogenation is considered due to the exposure of the external surface to an atomic H flux, which is consistent with most of the existing experimental studies. In the case of graphene, free-standing sheets are studied;

interactions of graphene layers with substrates are not taken into account in the present study.

The structural relaxation of the hydrogenated graphene and SWCNTs was carried out at a given  $\Theta$  by isothermal-isobaric ( $NPT$ ) molecular-dynamics (MD) simulations at low temperature and hydrostatic pressure. In the MD simulations, the interatomic interactions were described according to the Adaptive Interatomic Reactive Empirical Bond-Order (AIREBO) potential (Stuart et al., 2000; Brenner et al., 2002), which has been used widely for modeling solid carbon and hydrocarbon molecules, and discussed in details in Chapter 2 and Appendix A.

In our ( $NpT$ ) MD simulations, temperature and pressure were controlled by employing the Berendsen thermostat/barostat (Berendsen et al., 1984). Periodic boundary conditions were applied in the axial direction of the SWCNTs and in the two principal directions that define the plane of the pristine graphene sheet; the sizes of the supercells were chosen appropriately based on rigorous convergence tests, in order to give size-independent solutions. Due to the local disorder of the hydrogenated structures under investigation, which extends increasingly with increasing  $\Theta$ , a variant of simulated annealing was employed for structural relaxation in order to minimize the possibility of getting trapped into local energy minima during the relaxation process. This procedure involves equilibration through ( $NpT$ ) MD simulation at each temperature stage of a cooling schedule with a final temperature  $T = 0.1$  K.

### 3.2.2 Distribution on the Surface of Chemisorbed H Atoms

Theoretical studies (Gülseren et al., 2002; Park et al., 2005; Ferro et al., 2008; Casolo et al., 2009; Chernozatonskii and Sorokin, 2010; Pei et al., 2010; Wu et al., 2010) have demonstrated that the properties of hydrogenated SWCNTs and graphene depend on the patterns that the chemisorbed H atoms form on the surface on which they are distributed. In this study, the distributions on the surface of chemisorbed H atoms that are generated exhibit the essential features observed in experimental studies or predicted by first-principles DFT calculations, as outlined in Section 3.1 of this chapter.

For the generation of such representative hydrogenated graphene and SWCNT structures, we distributed the chemisorbed H atoms on the carbon surfaces by using two approaches. The first consists of simply distributing the H atoms randomly on the surface, while the second relies on an equilibrium Monte Carlo (MC) scheme to redistribute on the surface at given  $\Theta$  chemisorbed H atoms that were in a random arrangement initially: this is a compositional relaxation procedure that constitutes essentially a search for lower-energy configurations. The basis of this compositional relaxation approach is a conventional MC algorithm: in each MC step, an occupied (i.e., hydrogenated) site on the surface and a move from this site (initial state) to an unoccupied neighboring one (final state) are chosen randomly; the difference in energy,  $\Delta E$ , between the initial and final states is evaluated and the move is accepted or rejected according to the Metropolis criterion. In general, these moves induce structural changes; consequently, the hydrogenated structure needs to be relaxed locally after each such event. This local relaxation is accomplished by executing numerous Metropolis MC steps consisting of attempted displacements of the atoms in the neighborhood of the hydrogen

distribution event described above. Finally, the entire hydrogenated structure is relaxed following the methodology described in Section 3.2.1.

In Sections 3.3 and 3.4, the results obtained by using these two approaches for distribution on the surface of the chemisorbed H are confronted in order to examine whether the compositional relaxation procedure succeeded in obtaining lower-energy structures and to verify the difference that the MC sampling makes in the hydrogenated configurations and their properties. All of the results presented in the next sections correspond to ensemble averages over 12 and 10 different distributions for hydrogenated graphene and carbon nanotubes, respectively, for each sampling procedure employed.

### **3.3 Distribution of Chemisorbed Hydrogen on Graphene and SWCNTs**

This study focuses on the analysis of the morphological and structural changes undergone by graphene layers and carbon nanotubes upon their hydrogenation, by employing representative hydrogenated structures that exhibit the main features observed in such structures in experiments and first-principles calculations regarding the distribution of chemisorbed hydrogen on the surface. In order to evaluate the compositional relaxation procedure described in Sections 3.2.2 regarding its ability to generate representative distributions of chemisorbed H atoms, we need to evaluate parameters that characterize the detailed structure of the resulting hydrogenated graphene and SWCNTs.

One of these parameters gives the fraction of each type of C-C bonding present in the hydrogenated structure. Typically, two types of bonding are present in the structure

of hydrogenated graphene/SWCNTs:  $sp^2$  (C-C) and  $sp^3$  (C-C and C-H) hybridized bonds, each one with its characteristic bond lengths. A representative set of C-C radial distribution functions (RDFs),  $\rho g(r)$ , in a hydrogenated (14,14) SWCNT at various H surface coverages,  $\Theta$ , is given in Figure 3.1(a), spanning the range  $0 \leq \Theta \leq 1$ . Three peaks are observed over the relevant range of  $r$ . The first peak is exhibited at around  $r = 1.4 \text{ \AA}$ , which corresponds to  $sp^2$  C-C bonds, involving two non-hydrogenated carbon atoms, the second one at around  $r = 1.5 \text{ \AA}$ , and a third one at around  $r = 1.6 \text{ \AA}$ . The second and third peaks correspond to  $sp^3$  C-C bonds; the peak at  $r \sim 1.5 \text{ \AA}$  corresponds to a C-C bond between a hydrogenated and a non-hydrogenated carbon atom, while the peak at  $r \sim 1.6 \text{ \AA}$  corresponds to a C-C bond between two hydrogenated carbon atoms. Here, we denote these two types of  $sp^3$  C-C bonds as  $sp^3$ -A and  $sp^3$ -B, respectively. Figure 3.1(b) illustrates the three different types of C-C bonds that yielded the C-C RDF peaks of Figure 3.1(a). The fraction of each type of C-C bonds in the overall structure is defined as  $f_{spx} \equiv N_{spx}/N_{tb}$ , where  $N_{spx}$  is the number of bonds of each type ( $spx = \{sp^2, sp^3\text{-A}, sp^3\text{-B}\}$ ) and  $N_{tb}$  is the total number of C-C bonds in the structure; each  $f_{spx}$  parameter can be evaluated by evaluating the integrals of the C-C RDF curves associated with each peak (the number of atoms within a distance between  $r$  and  $r+\Delta r$  from a central atom is given by  $N(r, \Delta r) = 4\pi \int_r^{r+\Delta r} x^2 \rho g(x) dx$ ), or by simply checking the number and type of neighbors involved in every C-C bond formed in the hydrogenated structure. It must be mentioned that, even though the concept of bond hybridization is purely quantum mechanical, here it is treated merely in terms of chemical local environment (through the

geometry of the atomic configurations) and nature of neighbors; this is necessary for relaxed structures computed based on classical interatomic potentials such as AIREBO.

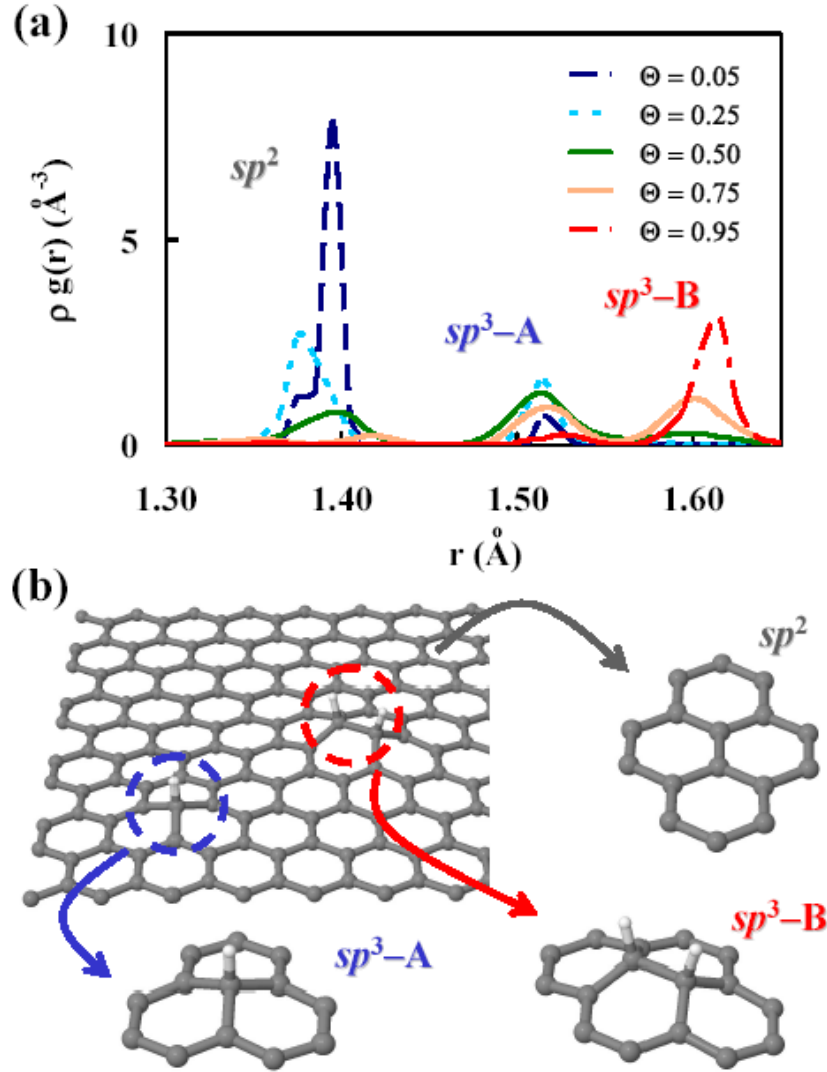


**Figure 3.1.** (a) C-C radial distribution function,  $\rho g(r)$ , in hydrogenated (14,14) SWCNTs at different H surface coverages,  $\Theta$ . (b) Example of a hydrogenated graphene layer, depicting the three typical types of C-C bonds (shown in magnification) that have been classified as  $sp^2$ ,  $sp^3-A$ , and  $sp^3-B$  bonds; these types of bonds correspond to the three peaks in the  $\rho g(r)$  distributions in (a) that have been marked accordingly.

Figure 3.2(a) shows the fraction of each type of C-C bonds in the structure,  $\phi = f_{sp^x}$ , as a function of the H surface coverage,  $\Theta$ , for hydrogenated graphene layers; for

SWCNTs of different diameters and chiralities, the computed curves are completely analogous with only slight quantitative differences. Two sets of data are shown, one for an ensemble of random H distributions and another one for an ensemble of distributions of chemisorbed H atoms obtained from the compositional relaxation procedure of Section 3.2.2. It is evident that the redistribution of H atoms according to the compositional relaxation procedure leads to an increase in the fractions of  $sp^2$  and  $sp^3$ -B C-C bonds at intermediate and higher H coverages compared to those for random distributions; consequently, there is a decrease in the fraction of  $sp^3$ -A C-C bonds within the same range of H coverages. These findings are consistent with previously reported experimental and first-principles computational results (Zecho et al., 2002; Hornekær et al., 2006a,b, 2007; Andree et al., 2006; Rougeau et al., 2006; Roman et al., 2007; Cuppen and Hornekær, 2008; Ferro et al., 2008, 2009; Kerwin and Jackson, 2008; Balog et al., 2009; Casolo et al., 2009; Šljivančanin et al., 2009; Sessi et al., 2009). At low H coverages, the chemisorbed H tends to be arranged in the form of the energetically favored pairs described in Section 3.1; there is a low percentage of hydrogenated-atom clusters with more than two C atoms and most of the pairs are arranged as ortho-dimers or other energetically favored ones, resulting in  $sp^2$  and  $sp^3$ -A as the dominant C-C bond types. With increasing  $\Theta$ , clusters of hydrogenated atoms larger than pairs start to form, leading to an increase in the number of  $sp^3$ -B and  $sp^2$  bonds. Interestingly, for random distributions, the ensemble averaged  $\phi(\Theta)$  curves for  $sp^2$  and  $sp^3$ -B C-C bond types are symmetric with respect to each other over the range  $0 \leq \Theta \leq 1$ , with  $\Theta = 0.50$  as the axis of symmetry; for  $sp^3$ -A C-C bonds, the  $\phi(\Theta)$  curve also is symmetric with respect to  $\Theta = 0.50$  and exhibits a maximum at  $\Theta = 0.50$ . Also, at  $\Theta = 0.50$ ,  $f_{sp^3B} = f_{sp^2}$  and  $f_{sp^3A} = f_{sp^3B} +$

$f_{sp^2} = 2f_{sp^3}$ . The compositional relaxation procedure “flattens” the  $\phi(\Theta)$  curve for the  $sp^3$ -A bonds by reducing its maximum value, while retaining the symmetry between the  $\phi(\Theta)$  curves for the other two types of C-C bonds.

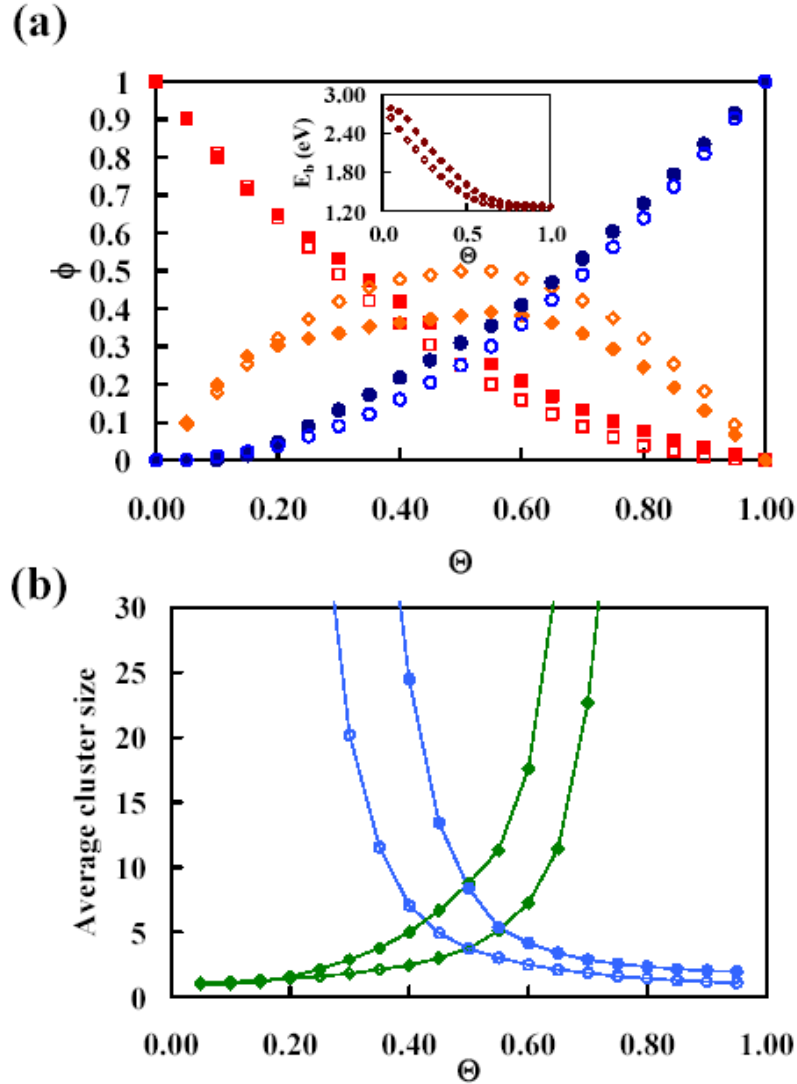


**Figure 3.2.** (a) Fraction,  $\phi$ , of  $sp^2$  and  $sp^3$  C-C bonds in the structure of hydrogenated graphene as a function of H surface coverage,  $\Theta$ . The fractions of  $sp^2$ ,  $sp^3$ -A, and  $sp^3$ -B bonds are denoted by squares, diamonds, and circles, respectively. The inset shows the dependence on  $\Theta$  of the chemisorbed H binding energy,  $E_b$ . (b) Average size of clusters of hydrogenated (diamonds) and non-hydrogenated (circles) carbon atoms in the structure of hydrogenated graphene as a function of  $\Theta$ ; the cluster size is measured in number of carbon atoms. In all the plots shown, open and filled symbols are used to denote random distributions (initial states) and MC-relaxed distributions of chemisorbed H atoms, respectively.

The inset of Figure 3.2(a) shows the binding energy of chemisorbed hydrogen,  $E_b$ , as a function of  $\Theta$  for the same hydrogenated graphene layers; the binding energy is defined as  $E_b(\Theta) \equiv (E_C - E_{\text{CH}}(\Theta))/N_{\text{H}}(\Theta)$ , where  $E_C$  and  $E_{\text{CH}}$  are the energy of pristine and hydrogenated graphene, respectively, and  $N_{\text{H}}$  is the number of chemisorbed H atoms.  $E_b$  is higher for the structures obtained by compositional relaxation, confirming that the MC relaxation procedure is effective in generating lower-energy structures. It should be mentioned that the quantity  $E_b$  defined above does not take into account the energy of the isolated H atoms prior to their chemisorption onto the graphene layer; consequently, the  $E_b(\Theta)$  curves depicted in the inset of Figure 3.2(a) are shifted vertically compared to the ones corresponding to the true binding energies. Despite this, however, the parameter  $E_b$  can be used directly for comparing the different hydrogenated structures in terms of their relative stability.

The tendency for clustering of hydrogenated atoms with increasing  $\Theta$  also can be analyzed by computing the average size of clusters of hydrogenated and non-hydrogenated C atoms in hydrogenated graphene as a function of  $\Theta$ . This is shown in Figure 3.2(b) for both types (random vs. MC-relaxed) of H distributions. The average cluster size is defined as the average size of chains of consecutive atoms of a specific type (hydrogenated vs. non-hydrogenated) on the graphene structure. The average size of clusters of hydrogenated atoms increases with increasing  $\Theta$ , while the opposite trend is observed for clusters of non-hydrogenated atoms. Comparing the  $\Theta$  dependences of the cluster sizes obtained by the two different methods of chemisorbed H distribution on the surface shows that for  $\Theta > 0.20$ , compositional relaxation leads to an increase in the average cluster size of hydrogenated atoms; the trend is qualitatively the same for clusters

of non-hydrogenated atoms (i.e., compositional relaxation leads to larger cluster sizes). These sequences of non-hydrogenated C atoms are characterized by the presence of delocalized  $sp^2$  bonds (which are more stable than localized  $sp^2$  bonds), since the structure is not very strained in these regions.

In summary, at intermediate and higher H coverages, we find a tendency for formation of large-size clusters of hydrogenated atoms toward maximizing the presence of  $sp^2$  conjugated bonds; this is consistent with previously reported experimental and *ab initio* findings (Hornekær et al., 2006b; Andree et al., 2006; Balog et al., 2009; Bauschlicher, 2001; Bauschlicher and So, 2002; Gülseren et al., 2002; Yildirim et al., 2001). At lower coverages, the hydrogenated graphene structure is characterized by various energetically favorable pairs of hydrogenated C atoms as discussed in Sec. 3.1.

The effect of the compositional relaxation procedure on the redistribution of H atoms throughout the graphene plane can be visualized and better understood if “hydrogen distribution maps” are used; these consist of top views of the undistorted honeycomb lattice, on which hydrogenated and non-hydrogenated carbon atoms are marked with different colors. Examples of such distribution maps for graphene layers at different H surface coverages are displayed in Figure 3.3 for random distributions (left column) and compositionally relaxed distributions (middle column). A comparison between the random and the compositionally relaxed distribution maps illustrates clearly the clustering of hydrogenated and non-hydrogenated C atoms and the consequent formation of more “ordered” patterns upon redistribution of the chemisorbed H atoms according to the MC relaxation scheme. Moreover, these maps can be compared visually with STM images of hydrogenated graphite/graphene surfaces that have been reported in

the literature (Hornekær et al., 2006a,b, 2007; Andree et al., 2006; Balog et al., 2009; Sessi et al., 2009). The right column of Figure 3.3 displays some of these STM images, extracted from the work of Hornekær and coworkers (Hornekær et al., 2006b), where dark and bright spots on the lattice represent hydrogenated and non-hydrogenated surface sites, respectively. The identification of detailed structures on these STM images by mere visual inspection is not straightforward, but the main features of the images are evident and can be compared with the maps of the middle column of Figure 3.3. There is no report of the exact values for the surface coverage in each one of these STM images (Hornekær et al., 2006b), but the coverage increases from (a) to (d) as is done in the simulations and the objective here is to simply provide qualitative comparisons of structures with similar levels of surface H coverage.

Such maps of compositionally relaxed hydrogenated graphene structures and STM images share common features regarding the arrangement of H atoms throughout the surface: at low coverages, preferred pairs of hydrogenated atoms are distributed all over the surface, while at higher coverages, large clusters of hydrogenated atoms are formed, being surrounded by continuous chains of non-hydrogenated atoms. These direct comparisons demonstrate that the procedure employed for obtaining representative hydrogenated structures (AIREBO-based structural relaxation and MC compositional relaxation) describes quite satisfactorily the distribution of chemisorbed H atoms on hydrogenated graphene surfaces over the entire  $\Theta$  range examined, i.e., it predicts structures that exhibit the features of the experimentally observed and *ab initio* predicted configurations discussed in Section 3.1. We have found completely analogous results for hydrogenated SWCNTs regarding the distribution of the chemisorbed hydrogen.

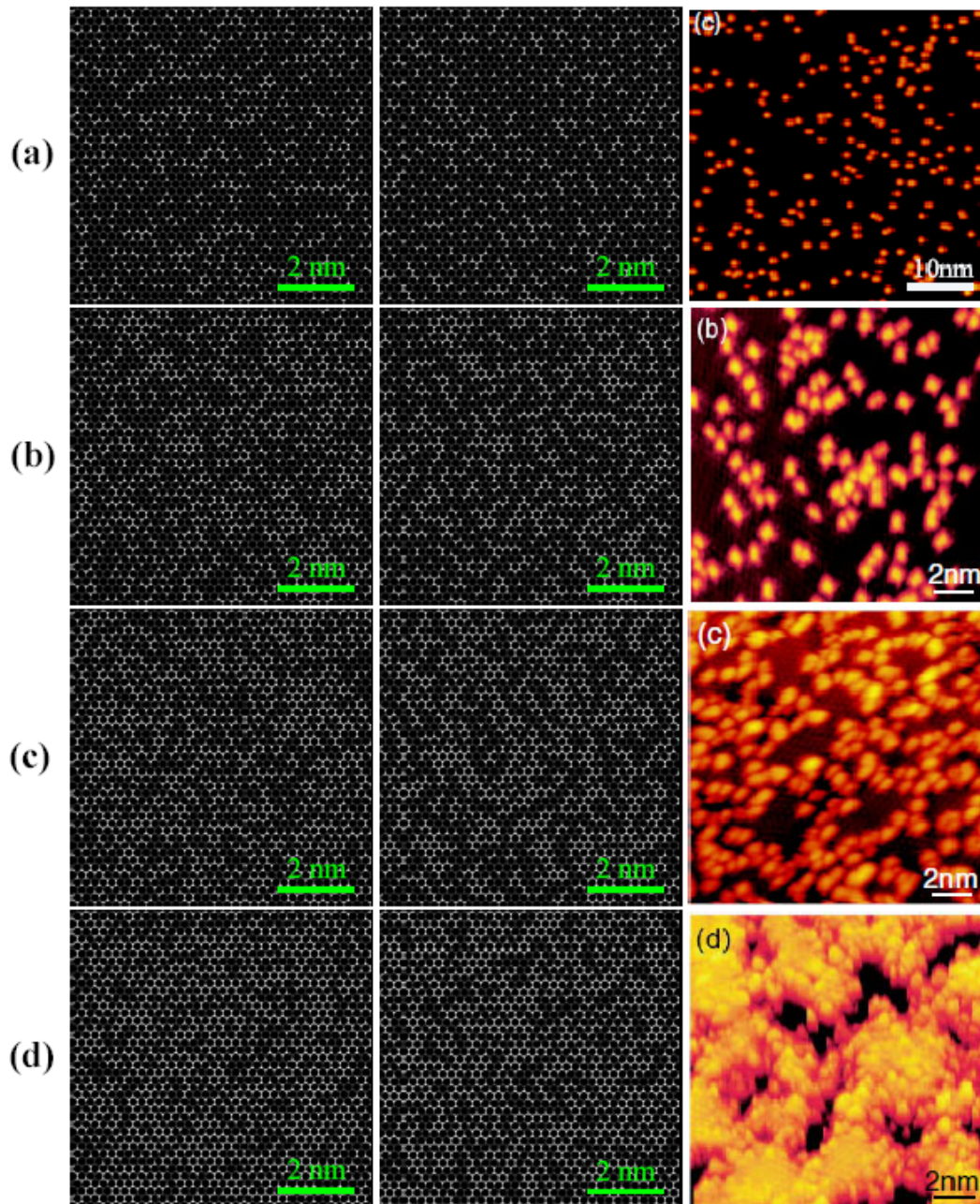


**Figure 3.3.** Top views (maps) of representative distributions of H atoms chemisorbed onto graphene layers with H surface coverages of (a)  $\Theta = 0.25$ , (b)  $\Theta = 0.40$ , (c)  $\Theta = 0.50$ , and (d)  $\Theta = 0.60$ . The first and second columns show simulation-generated maps based on random and MC-optimized distributions, respectively. Only carbon atoms are shown for clarity. Carbon atoms shaded dark gray and light gray are used to denote hydrogenated and non-hydrogenated surface sites, respectively. The third column shows STM images of hydrogenated graphite surfaces at surface coverages that are similar to those of the simulation-generated maps on each corresponding row, reproduced from Hornekær et al., 2006b. In these STM images, the bright spots correspond to the hydrogenated surface sites.

### 3.4 Structural and Morphological Analysis of Hydrogenated Graphene and SWCNTs

Structures of hydrogenated graphene layers and SWCNTs have been relaxed following the approach described in Section 3.2.1, for various surface coverages over the range  $0 \leq \Theta \leq 1$ , and employing both methods (random vs. MC-relaxed) for determining the distribution of chemisorbed H on the surface. Here, a detailed characterization is carried out of the structural and morphological changes induced by hydrogenation on these structures in order to provide a comprehensive picture of these transformations.

Figure 3.4 depicts configurations of representative relaxed structures of hydrogenated graphene layers at different H surface coverages (shown as the top panels of Figure 3.4) with H distributions obtained by the compositional relaxation procedure. Visual inspection of these configurations shows significant changes in the surface that have been induced by its hydrogenation: ripples of varying sizes have formed as a result of the  $sp^2$ -to- $sp^3$  C-C bonding transition that has occurred. One feature that is common to all of the computed structures is the presence of “hills”, i.e., finite regions that have been displaced upwards mostly in areas containing clusters of hydrogenated atoms, surrounded by “valleys”, i.e., areas characterized by the presence of consecutive chains of non-hydrogenated atoms, as pointed out by the corresponding H distribution maps (shown as the bottom panels of Figure 3.4). The hydrogenated graphene surface morphology also can be visualized by contour plots of the vertical displacements of the C atoms (in the  $z$ -direction) from the  $xy$ -plane, which also are depicted in Figure 3.4 (middle panels); the darkest color/shade corresponds to the deepest valleys, while the lightest color/shade corresponds to the highest hills in the surface morphology. This analysis of hydrogenated

graphene configurations demonstrates the strong correlation between areas rich in hydrogenated and non-hydrogenated C atoms with the formation of the aforementioned morphological features (hills and valleys, respectively).

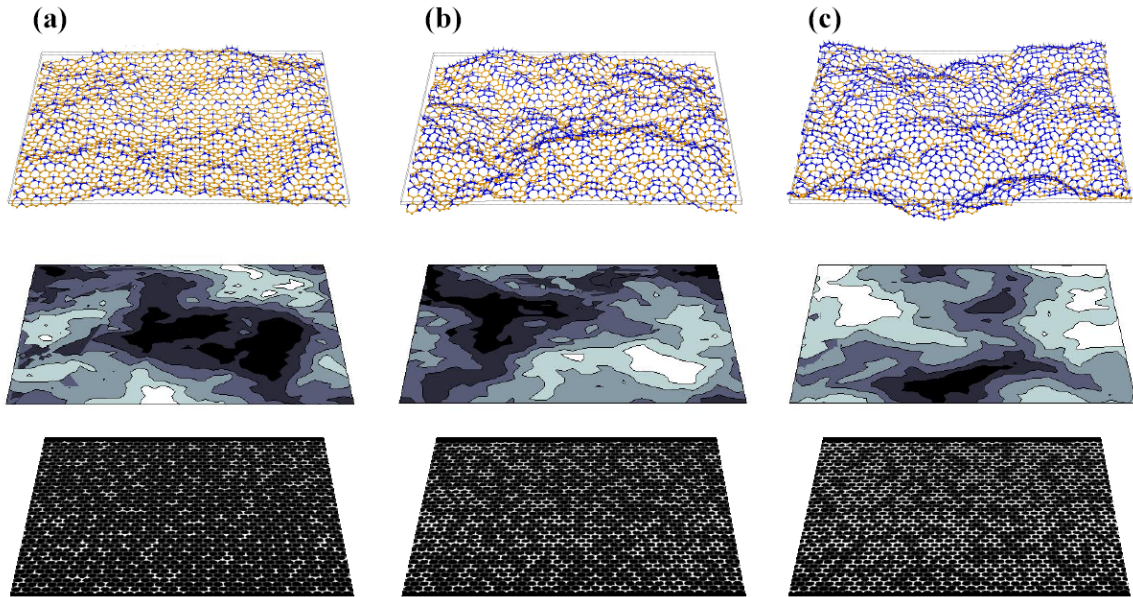


**Figure 3.4.** Relaxed configurations of hydrogenated graphene with H surface coverages of (a)  $\Theta = 0.25$ , (b)  $\Theta = 0.40$ , and (c)  $\Theta = 0.55$ . The top row shows three-dimensional views of the configurations, highlighting the graphene surface morphology. Carbon atoms shaded dark gray (colored blue online) and light gray (colored orange online) are used to denote hydrogenated and non-hydrogenated sites, respectively. The middle row shows contour plots of the corresponding surface morphologies, in terms of the distribution on the graphene plane of the vertical displacements of the carbon atoms with respect to the planar morphology at  $\Theta = 0$ . The color/shade is darkest at the deepest valleys and lightest at the highest hills of the surface morphology. The bottom row depicts top views (maps) of the distributions of the H atoms chemisorbed onto the graphene layers; carbon atoms shaded dark gray and light gray are used to denote hydrogenated and non-hydrogenated sites, respectively.

Figure 3.5 shows the corresponding results for the morphologies of hydrogenated (24,0) SWCNTs. To the right of the depicted configurations, the H distribution maps are displayed on the unfolded nanotubes. The configurations on the left correspond to side views of the hydrogenated nanotubes, viewed from different angles; the dashed and solid

horizontal lines aligned with the SWCNT axis are used to denote the top and bottom tangent planes to the SWCNT for each one of the side views, respectively. The SWCNT surface is seen to be irregular and morphological patterns analogous to those observed in the hydrogenated graphene layers are evident: C atoms are displaced outwards in regions of the SWCNT containing clusters of hydrogenated C sites, while they are displaced inwards in regions dominated by chains of non-hydrogenated C atoms.

Figures 3.4 and 3.5 also demonstrate that in the very low and very high hydrogen coverage limits ( $\Theta \rightarrow 0$  and  $\Theta \rightarrow 1$ , respectively), the surface morphologies tend to be smoother than those at intermediate coverages, which are characterized by high concentrations of hills and valleys. A parameter that can be used to characterize this effect is the surface roughness. For graphene sheets on the  $xy$ -plane, the surface

roughness can be defined as  $\eta_z \equiv \sqrt{\frac{1}{N} \sum_{k=1}^N (z_k - \bar{z})^2}$ , where  $z_k$  is the vertical displacement of

the  $k$ -th C atom,  $\bar{z}$  is the average vertical displacement, and  $N = N_C$  is the total number of C atoms on the surface. For SWCNTs, an analogous definition can be used for the surface roughness,  $\eta_r$ , by replacing in the definition of  $\eta_z$  the vertical displacements  $z_k$  and  $\bar{z}$  with the radial distance from the axis of the nanotube,  $r_k = (x_k^2 + y_k^2)^{1/2}$  (for a nanotube that is aligned with the  $z$  axis), and the average radius  $R$ , respectively. The computed surface roughness is plotted as a function of  $\Theta$  for graphene layers and SWCNTs in Figure 3.6. For both graphene and SWCNTs, we observe that the maximum surface roughness values are exhibited at intermediate coverages, where the numbers of  $sp^2$  and  $sp^3$  C-C bonds are comparable and the number of  $sp^3$ -A C-C bonds reaches its maximum (see Figure 3.2); at lower and higher  $\Theta$  values,  $sp^2$  and  $sp^3$ -B C-C bonds are

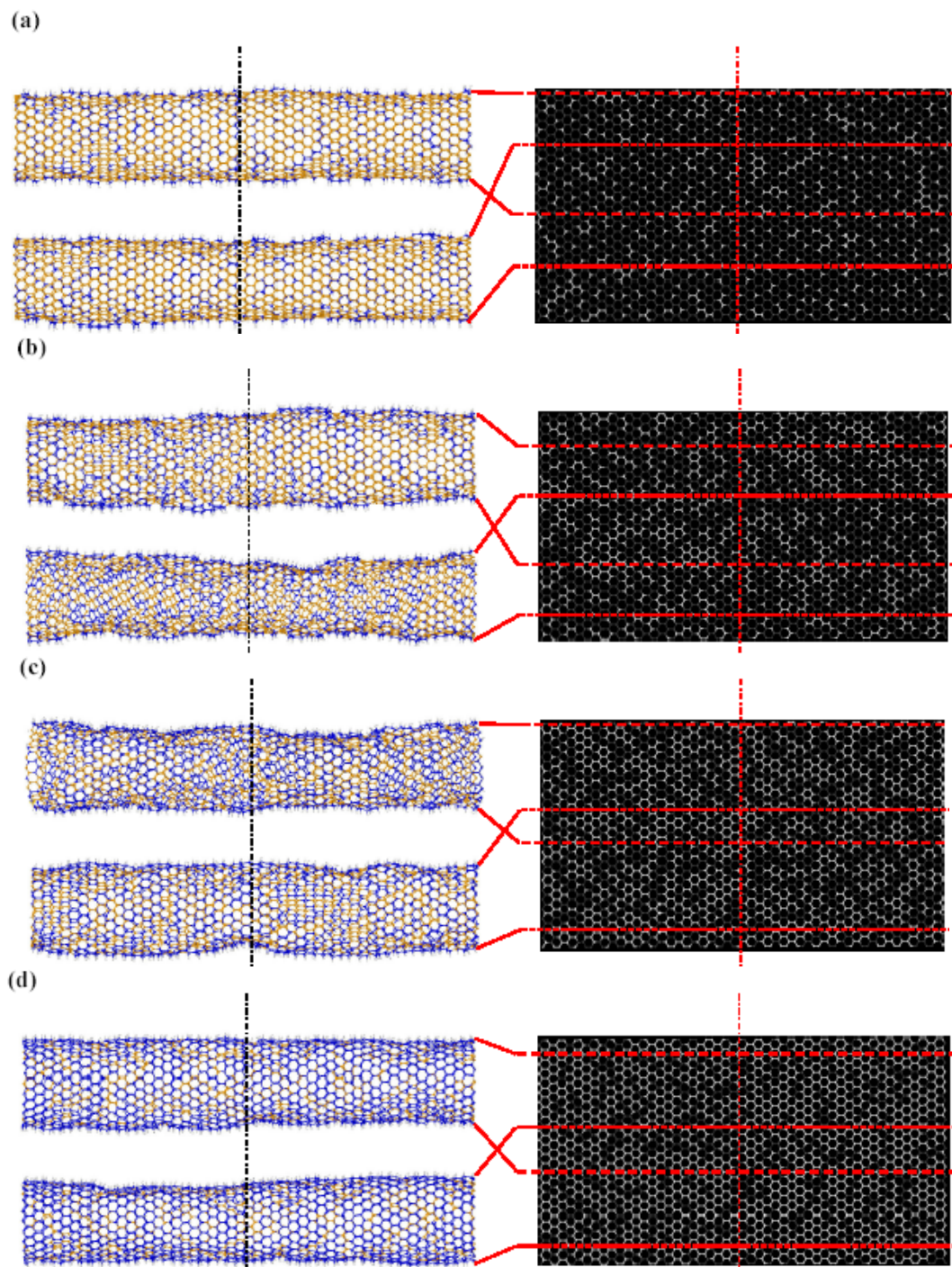


**Figure 3.5.** Relaxed configurations of a hydrogenated (24,0) SWCNT (shown on the left) with (a)  $\Theta = 0.25$ , (b)  $\Theta = 0.40$ , (c)  $\Theta = 0.55$ , and (d)  $\Theta = 0.75$ , with the corresponding top views (maps) of the chemisorbed hydrogen distributions on the unrolled surface of the zigzag nanotube (shown on the right). The horizontal lines crossing the H distribution maps represent the top and bottom tangent planes depicted in the corresponding three-dimensional configurations. In all of the atomic configurations and H distribution maps shown, the dot-dashed vertical lines are perpendicular to the nanotube axis.

predominant, respectively, and the surface tends to preserve its planarity and smooth cylindrical geometry for graphene and SWCNTs, respectively.

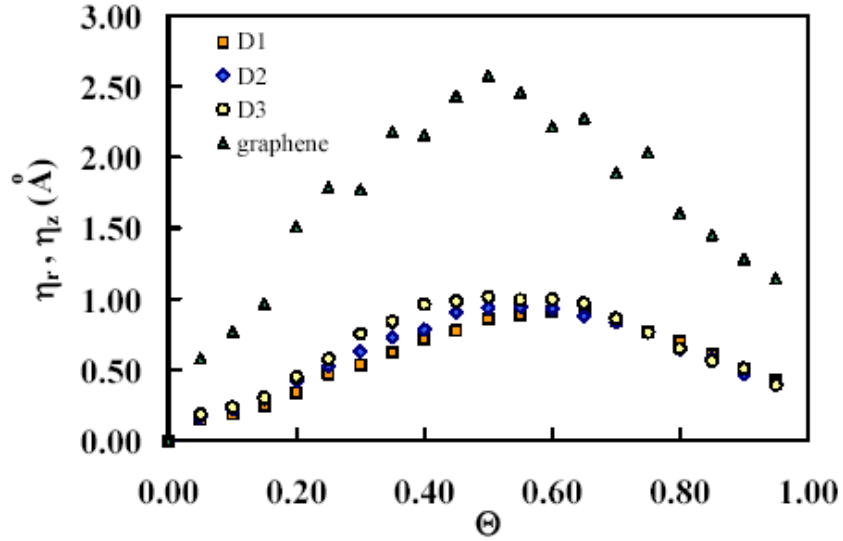


**Figure 3.6.** Surface roughness,  $\eta_z$  and  $\eta_r$ , as a function of H surface coverage,  $\Theta$ , for hydrogenated graphene sheets (triangles) and SWCNTs (squares, diamonds, and circles). The different symbols for the SWCNT results represent values for different average diameters of the pristine nanotubes, with  $D_{\text{avg}} = 1.18$  nm, 1.57 nm, and 1.86 nm for the data sets labeled D1, D2, and D3, respectively.

The structural and morphological features of the hydrogenated graphene and SWCNTs discussed above are directly correlated with significant changes in the dimensions of these materials when compared to their pristine states. Experiments demonstrated the swelling of carbon nanotubes upon their exposure to atomic hydrogen, as reflected by an increase in the diameters of SWCNTs (Zhang et al., 2006; Nikitin et al., 2008). This effect was investigated systematically for graphene layers and SWCNTs of different chiralities and diameters, using the structures and chemisorbed H distributions obtained both from random sampling and from the detailed compositional

relaxation procedure, which results in configurations with the same features (H distributions) as observed in experimental studies.

Different quantitative metrics were used to compute the changes due to hydrogenation in the structures of hydrogenated SWCNTs and of graphene layers compared to their corresponding pristine states. For SWCNTs, we have used the radial strain, defined as  $\Delta R(\Theta)/R_0 \equiv (R(\Theta) - R(\Theta=0))/R(\Theta=0)$ , and the axial strain,  $\Delta L(\Theta)/L_0 \equiv (L(\Theta) - L(\Theta=0))/L(\Theta=0)$ , where  $R(\Theta)$  and  $L(\Theta)$  denote the average radius and length, respectively, of a relaxed hydrogenated SWCNT at a given H coverage  $\Theta$ . In a similar manner, for graphene, we define the strains in the  $x$ - and  $y$ -directions as  $\Delta L_x(\Theta)/L_{x0} \equiv (L_x(\Theta) - L_x(\Theta=0))/L_x(\Theta=0)$ , and  $\Delta L_y(\Theta)/L_{y0} \equiv (L_y(\Theta) - L_y(\Theta=0))/L_y(\Theta=0)$  respectively, where  $L_x$  and  $L_y$  denote the length of the relaxed supercell in the  $x$ - and  $y$ -directions of the graphene plane ( $xy$ -plane), respectively, at a given coverage  $\Theta$ . In Figures 3.7(a) and (b), values of the binding energy of chemisorbed H,  $E_b(\Theta)$ , and these deformation parameters are plotted as a function of  $\Theta$  for a (24,0) SWCNT and for a graphene sheet, respectively; in each case, two sets of results are displayed: one for random distributions of chemisorbed H and another one for H distributions obtained by compositional relaxation.

Figures 3.7 (a) and (b) show that the binding energy of chemisorbed H is higher at low  $\Theta$  and decreases with increasing  $\Theta$ . Also, the results for the  $\Theta$  dependence of this parameter obtained by both sampling methods demonstrate that compositional relaxation generates lower-energy structures, as it was shown in the inset of Figure 3.2(a). The results for the various strains show that at low  $\Theta$ , the relative elongations are negligible. An increase in  $\Theta$  makes the strains decrease slightly. However, beyond a critical value of  $\Theta$ , the various strains are seen to increase monotonically and eventually linearly with

increasing  $\Theta$ . The same trends are observed in the  $\Theta$  dependence of the various deformation metrics for hydrogenated structures with H distributions obtained from either one of the two sampling methods, but some quantitative changes are evident at intermediate  $\Theta$  levels. Specifically, the compositional relaxation procedure generated structures with smaller tensile (positive) strains and even compressive (negative) strains at this intermediate  $\Theta$  range. The decrease in the strains at intermediate coverages is due to the clustering of hydrogenated atoms and the ensuing maximization of  $sp^2$  conjugated bonds (i.e., formation of chains of  $sp^2$  bonded C atoms), which causes the rippling of the surface at intermediate coverages. A comparison of the  $\Theta$  dependences of Figures 3.6 and 3.7 demonstrates clearly that both the minima in the strains and the maxima in the roughness results are exhibited at the same  $\Theta$  level; this is directly related to the rippling of the hydrogenated surface. Graphene planes undergo larger compressive strains at this  $\Theta$  level compared to SWCNTs as a result of the larger flexibility of an unfolded graphene sheet in a plane than that of its rolled-up counterpart; this effect also can be attributed to the larger surface roughness of hydrogenated graphene sheets than that of nanotubes at the same  $\Theta$ , as has been shown in Figure 3.6.

The same trends in the  $\Theta$  dependence of these morphological and deformation parameters are observed in SWCNTs of different diameters and chiralities with only slight quantitative differences; this is demonstrated in Figures 3.8 and 3.9. In Figures 3.8 and 3.9, only results corresponding to structures whose chemisorbed H distributions are obtained by compositional relaxation are shown. The binding energy of chemisorbed H decreases with increasing nanotube diameter and zigzag nanotubes are characterized by a slightly higher binding energy compared to armchair nanotubes of similar diameters. A dependence of strains on nanotube diameter and chirality is observed mainly at higher  $\Theta$  levels; the axial strain increases with increasing SWCNT diameter and chiral angle and it

is higher for armchair than for zigzag nanotubes of similar diameter, while the radial strain increases/decreases with nanotube diameter for armchair/zigzag SWCNTs. In both cases of nanotube configuration, the dependence of strain on chirality is more pronounced for nanotubes of smaller diameters; for SWCNTs with larger diameters, this dependence is practically negligible. Slight differences are observed at intermediate coverages. For both axial and radial strains, the larger the nanotube diameter, the larger the compressive strain induced by hydrogenation at intermediate coverages ( $\Theta \sim 0.40$ ).

These changes in the dimensions of the hydrogenated structures also can be represented in terms of volumetric and surface area changes. For SWCNTs, this volumetric deformation parameter that gives a measure of dilatation upon hydrogenation can be defined as  $\Delta\bar{V}(\Theta)/\bar{V}_0 = (\bar{V}(\Theta) - \bar{V}(\Theta = 0))/\bar{V}(\Theta = 0)$ , where  $\bar{V}(\Theta) = \pi\bar{R}(\Theta)^2L(\Theta)$  is the average nanotube volume at a coverage  $\Theta$ . For graphene, in a similar manner, an areal deformation parameter can be defined as  $\Delta\bar{A}(\Theta)/\bar{A}_0 = (\bar{A}(\Theta) - \bar{A}(\Theta = 0))/\bar{A}(\Theta = 0)$ , where the area projected on the  $xy$ -plane is defined as  $\bar{A}(\Theta) = L_x(\Theta) \cdot L_y(\Theta)$ . Results for the  $\Theta$  dependence of these deformation parameters are shown in Figure 3.10. As expected, the curves follow the same trend observed for the strains, Figures 3.7, 3.8 and 3.9, exhibiting a minimum over the range of  $\Theta = 0.30$ - $0.40$ ; starting from a pristine state, an increase in the H surface coverage leads to a slight shrinking of the structures initially, while it leads to their expansion beyond a certain critical level, as reflected in the monotonic increase with  $\Theta$  in the average volume/area that is observed at higher values of  $\Theta$ .

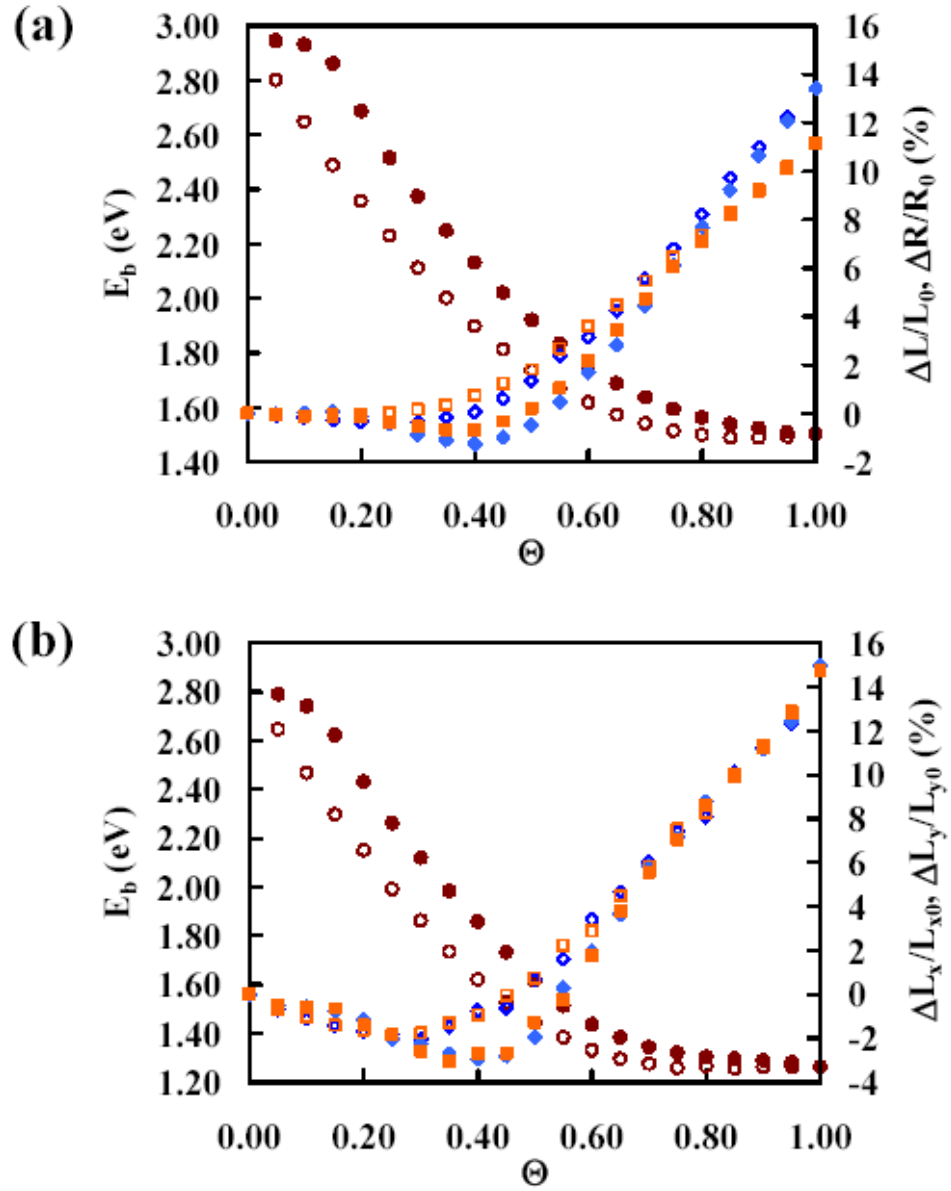


**Figure 3.7.** (a) Chemisorbed H binding energy,  $E_b$  (circles), axial strain  $\Delta L/L_0$  (squares), and radial strain  $\Delta R/R_0$  (diamonds) for a (24,0) SWCNT and (b)  $E_b$  (circles) and strains along the two principal directions  $x$  and  $y$ ,  $\Delta L_x/\Delta L_{x0}$  (squares) and  $\Delta L_y/\Delta L_{y0}$  (diamonds), for a hydrogenated planar graphene sheet as functions of H surface coverage,  $\Theta$ . Open and filled symbols are used to denote random distributions (initial states) and MC-relaxed distributions of chemisorbed H atoms, respectively.

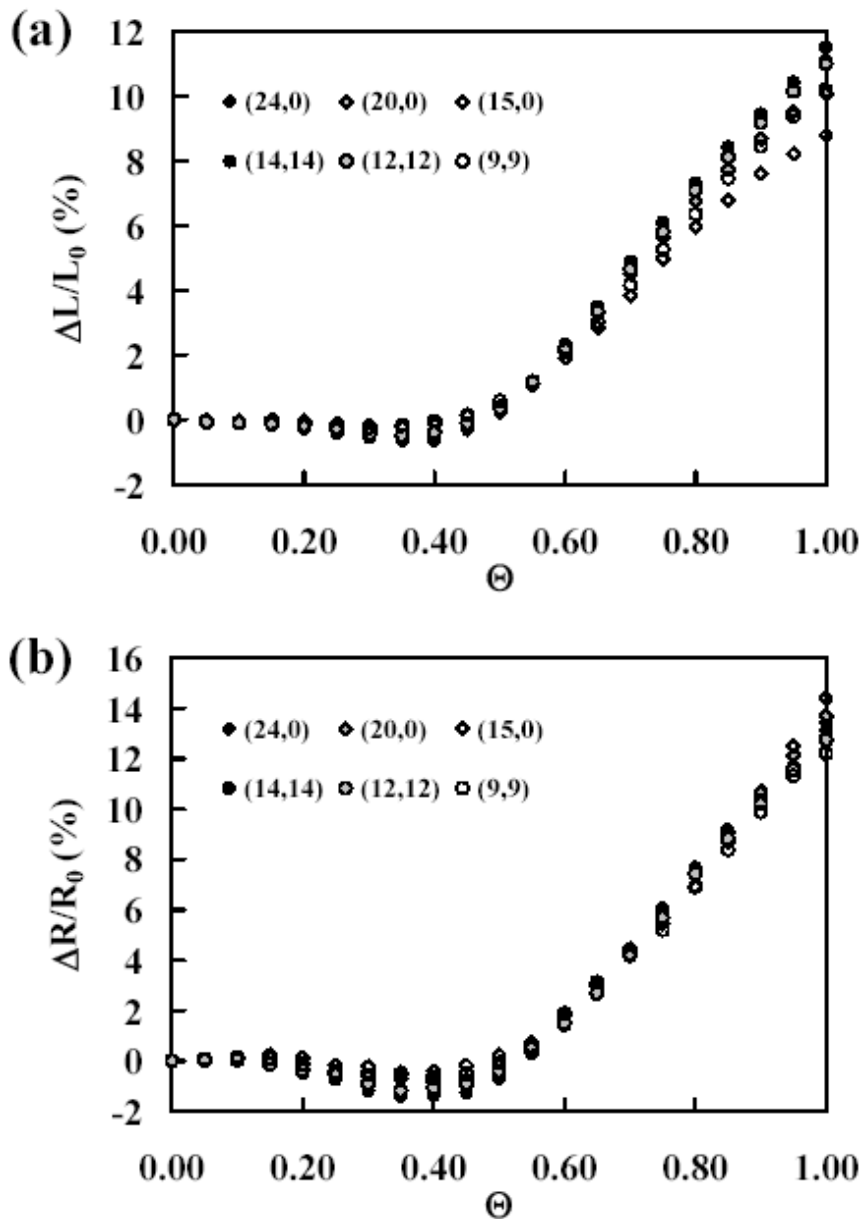


**Figure 3.8.** (a) Axial strain,  $\Delta L/L_0$ , and (b) radial strain,  $\Delta R/R_0$ , as functions of H surface coverage,  $\Theta$ , for relaxed hydrogenated SWCNTs of different diameters and chiralities.

We also validated the findings of the MD simulations by comparisons with first-principles DFT calculations; the key parameter for systematic comparisons is a structural metric given by the ratio  $f \equiv N_{sp^2}/N_{sp^3}$ , defined similarly before. Figure 3.11 (a) shows, as a function of the H coverage  $\Theta$ , a comparison of the ratio  $f$  computed by AIREBO-MD

and DFT/GGA for two zigzag nanotubes, (12,0) and (15,0) with diameters  $D = 0.93$  and  $1.16$  nm, respectively. It is seen that both methods give practically identical results for the  $\Theta$  dependence of  $f$ .

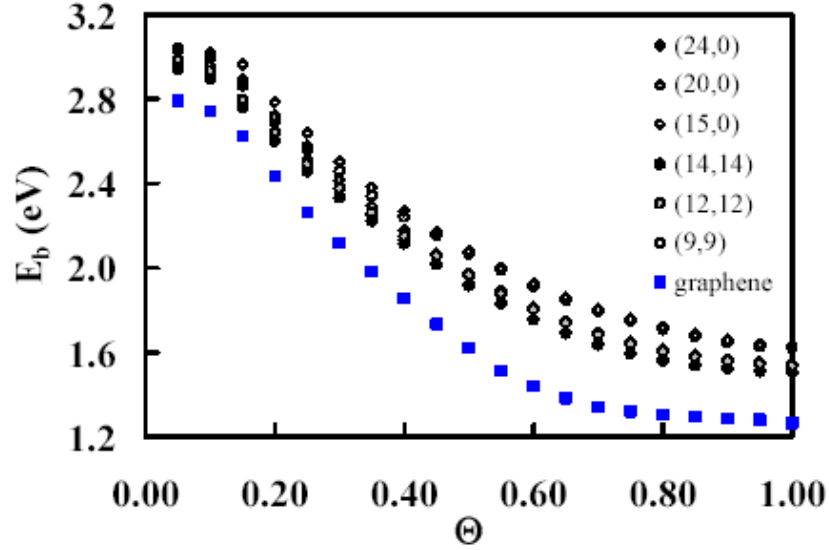


**Figure 3.9.** Chemisorbed H binding energy,  $E_b$ , as a function of H surface coverage,  $\Theta$ , for hydrogenated SWCNTs of different diameters and chiralities and for a graphene sheet.

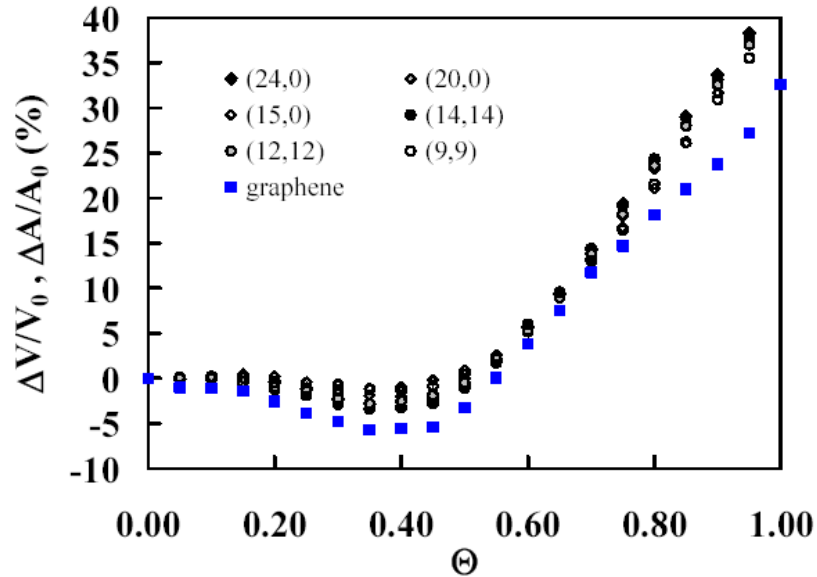


**Figure 3.10.** Volumetric ( $\Delta\bar{V}/\bar{V}_0$ ) and areal ( $\Delta\bar{A}/\bar{A}_0$ ) deformation parameters as functions of H surface coverage,  $\Theta$ , for relaxed hydrogenated SWCNTs of different diameters and chiralities and for graphene, respectively.

To finalize, we also repeated some of the MD simulations for relaxation of hydrogenated SWCNTs at higher temperatures. We did not find any significant thermal effects on the  $\Theta$  dependence of the structure and deformation of the hydrogenated SWCNTs; this is shown in Figure 3.11(b), where MD results are compared for the  $\Theta$  dependence of  $f$  defined in the previous paragraph and  $\Delta L/L$  at temperatures  $T = 0.1$  K and 300 K. We found, however, that at high H coverages, the strains are slightly higher at higher temperatures as a result of thermal expansion. This response was consistent for all the nanotube chiralities examined.

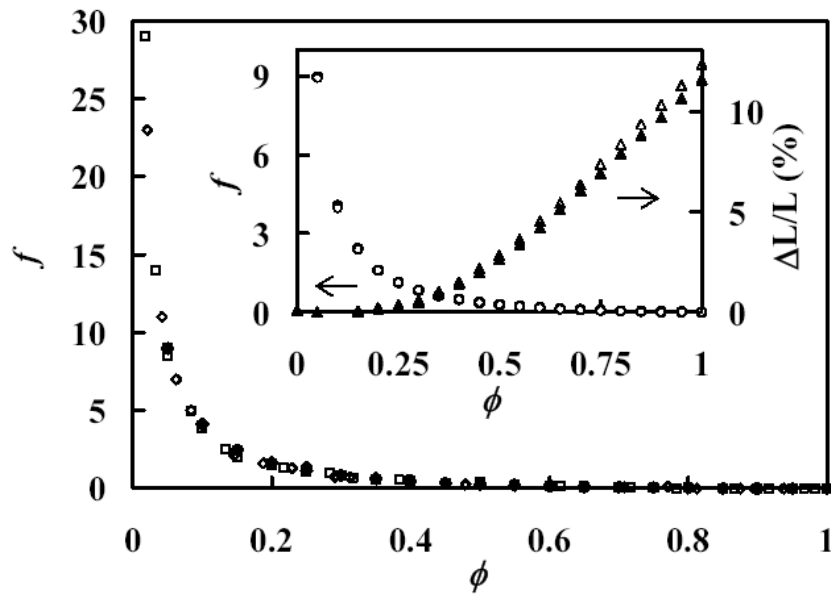


**Figure 3.11.** Dependence of the ratio  $f$  of  $sp^2$ - to  $sp^3$ -bonded C atoms on the H coverage  $\Theta$  for a (12,0) and a (15,0) SWCNT denoted by diamonds and squares, respectively. Filled and open symbols are used to denote AIREBO-MD results and DFT/GGA results, respectively. The inset shows AIREBO-MD results for the dependence on  $\Theta$  of the axial strain  $\Delta L/L$  (triangles) and the ratio  $f$  (circles) for a (14,14) SWCNT at  $T = 0.1$  K (filled symbols) and 300 K (open symbols); there is almost complete overlap between the two sets of  $f(\Theta)$  results at the two different temperatures.

### 3.5 Summary and Conclusions

In summary, a comprehensive analysis of the effects of hydrogenation on the structure of single graphene layers and SWCNTs was carried out that produced detailed information on the structural and morphological changes undergone by these materials upon their hydrogenation, as well as the determination of the dependence of these changes on the H surface coverage and on the arrangement of the chemisorbed hydrogen atoms on the surface. The entire range of H surface coverage,  $0 \leq \Theta \leq 1$ , was spanned in the analysis. We found a tendency for clustering of hydrogenated and of non-hydrogenated sites with increasing  $\Theta$ , as well as a monotonic increase with  $\Theta$  in various strain metrics beyond a critical surface coverage; this dependence of strains on  $\Theta$  is independent of nanotube chirality and diameter, as well as of temperature. The clustering leads to surface roughness as a result of surface morphologies characterized by ripples, i.e., the presence of hills and valleys due to clusters of hydrogenated and non-hydrogenated sites, respectively. The strain dependence on  $\Theta$  explains the experimentally observed swelling of carbon nanotubes upon their hydrogenation and the resulting problems in achieving uniform hydrogenation and the maximum hydrogen storage capacity of carbon nanotubes, subject which is discussed in details on Chapter 4.

An important ingredient of the analysis was the compositional relaxation method used for sampling the H atom arrangements on the carbon surfaces for given H coverage; this method was found to be efficient in determining H distributions consistent with previously reported experimental observations. Direct dynamical simulations of the exposure of the surfaces to a flux of H atoms and the subsequent relaxations provides an alternative detailed and accurate approach for computing chemisorbed H distributions;

however, the associated computational cost for the time scales required to be captured makes this approach impractical.

The calculations for graphene presented in this work considered only the one-sided hydrogenation of a free standing graphene layer. Similar analysis can be carried out for the case of two-sided hydrogenation of graphene, a route used for the synthesis of graphane (Elias et al., 2009; Sofo et al., 2007), as well as for the case where a graphene layer has been deposited on a substrate. The interactions between such a substrate and the graphene layers modify the energetics of adsorption of H atoms onto the graphene surface, which may change the favored arrangements of H atoms on the carbon surface compared to the case of a single graphene sheet or of graphite; such changes have been demonstrated recently (Balog et al., 2010; Lee et al., 2010). Also, graphene-substrate interactions may affect the dynamics and deformation of these carbon layers resulting from hydrogenation. However, all the findings presented in this study can be extended qualitatively to these cases since the important phenomena that govern the underlying structural and morphological changes have been captured adequately in the present analysis.

## CHAPTER 4

### EFFECTS OF STRUCTURAL CHANGES INDUCED BY HYDROGENATION ON THE HYDROGEN STORAGE CAPACITY OF CARBON NANOTUBES BUNDLES

#### 4.1 Introduction

A massive body of experimental and theoretical work has investigated the hydrogen storage capacity of carbon nanotubes (CNTs) following the original demonstration that CNTs can be used as hydrogen storage media (Dillon et al., 1997). Storage capacities ranging from 0.25 to 20 wt% have been reported (Yurum et al., 2009, and references therein), and numerous factors have been used to describe the variability and inconsistency of these results, including sample preparation, processing conditions, and presence of impurities such as amorphous carbon and catalyst particles. Both physisorption ( $H_2$ -CNT van der Waals interactions) and chemisorption (formation of stable  $sp^3$  C-H bonds) mechanisms have been accounted for hydrogen adsorption on CNTs. Chemisorption of H atoms (generated, e.g., in a  $H_2$  plasma) has been shown to provide storage capacities as high as 7 wt% (Nikitin et al., 2008), close to the theoretical value of 7.7 wt%, corresponding to a CNT containing one chemisorbed H atom per C atom. The measured storage capacities based on this approach varied among different studies (Khare et al., 2002a,b; Ruffieux et al., 2002, 2004; Nikitin et al., 2005, 2008; Tokura et al., 2008); this discrepancy is also due to particular features of the sample used including CNT diameter distribution and bundle density (Nikitin et al., 2008), and source of H atoms.

A limiting factor in the potential hydrogen storage capacity using chemisorbed H is the structural change undergone by CNTs upon their hydrogenation. Theoretical (Bauschlicher, 2001; Yildirim et al., 2001; Bauschlicher and So, 2002; Gülseren et al., 2002; Volpe and Cleri, 2003; Park et al., 2005; Muniz et al., 2009a; Muniz and Maroudas, 2010) and experimental (Zhang et al., 2006, Nikitin et al., 2008) studies have shown that hydrogenation causes CNT “swelling” as reflected by an increase in their dimensions. In Chapter 3 of this thesis, it was demonstrated that the resulting radial and axial strains are functions of the degree of hydrogenation as measured by the coverage,  $\Theta$ , of the nanotubes by chemisorbed atomic H. When single-walled CNTs (SWCNTs) are in the form of bundles, the expansion of individual nanotubes upon hydrogenation may introduce certain complications in the efficient hydrogenation of the bundles. H atoms need to diffuse through the interstitial space of the bundle in order to reach the innermost tubes. This is illustrated in Figure 4.1(a), where the simplest model of a bundle is depicted, consisting of a regular array of SWCNTs; the planar cross section of this array normal to the SWCNT axes forms a 2D hexagonal lattice. The arrows in Figure 4.1(a) denote the incoming atomic H flux. The hydrogenation-induced swelling of the nanotubes leads to a decrease in the inter-tube spacing in the bundle; as a result, the diffusion of H atoms through this inter-tube space becomes more difficult. This mass-transfer limitation causes a nonuniformity of bundle hydrogenation and may limit the hydrogen storage capacity of the CNT bundles.

The purpose of this chapter is to present an analytical model that describes the effect of nanotube swelling upon hydrogenation on the storage capacity of SWCNT bundles; the model is properly parameterized using atomistic calculations analogous to

the ones discussed from Chapter 3 for the relationship between the relative increase on CNT dimensions and H coverage of the CNT. This model provides experimentally testable hypotheses which can be used to explain the observed storage capacities for bundles of SWCNTs (Nikitin et al., 2005, 2008; Tokura et al., 2008).

## 4.2 Development of a Mathematical Model for Predicting the Onset of Mass Transfer Limitations in SWCNT Bundles

For a more detailed consideration of H mass transfer limitations in SWCNT bundles, we represent the bundle as a regular array of SWCNTs of equal diameter in their pristine state as depicted in Figure 4.1(a). The only criterion that we employ for efficient H diffusion through carbon nanotubes in a bundle is a minimum inter-tube spacing,  $d_{\min}$ , requirement, i.e.,  $d \geq d_{\min}$ , is required for efficient H diffusion where  $d$  is the inter-tube spacing. A close view of two nearest-neighbor nanotubes in the bundle is shown in Figure 4.1(b). The corresponding geometrical relationship is  $2R(\Theta) + d(\Theta) = a$ , where  $R$  is the radius of the carbon nanotube,  $0 < \Theta \leq 1$ , and  $a$  is the lattice parameter of the 2D hexagonal lattice of Figure 4.1(a);  $a$  is related to the density of the nanotube bundle,  $\rho_b$  [ $\rho_b = 2/(\sqrt{3}a^2)$ ]. The radius  $R$  accounts for the swelling of the individual nanotubes upon hydrogenation and can be expressed through a swelling function,  $f(\Theta)$ , as  $R(\Theta) = R_0 [1 + f(\Theta)]$ , i.e.,  $f(\Theta) = \Delta R(\Theta)/R_0 \equiv [R(\Theta) - R_0]/R_0$  is the radial strain of the hydrogenated CNT, where  $R_0$  is the carbon nanotube radius in the pristine state,  $\Theta = 0$ . Using  $d_{\min}$  as a characteristic length scale and introducing the dimensionless variables  $\delta \equiv d/d_{\min}$ ,  $\alpha \equiv a/d_{\min}$ ,  $\rho \equiv R/d_{\min}$ , and  $\rho_0 \equiv R_0/d_{\min}$ , the geometrical relationship becomes

$$\delta(\Theta) = \alpha - 2\rho_0 [1 + f(\Theta)]. \quad (4.1)$$

The requirement for efficient H diffusion in the inter-tube space of the SWCNT bundle is  $\delta(\Theta) \geq 1$ . The actual numerical value of the characteristic length  $d_{\min}$  can be computed by atomistic simulations, but it is not important for the present level of analysis.

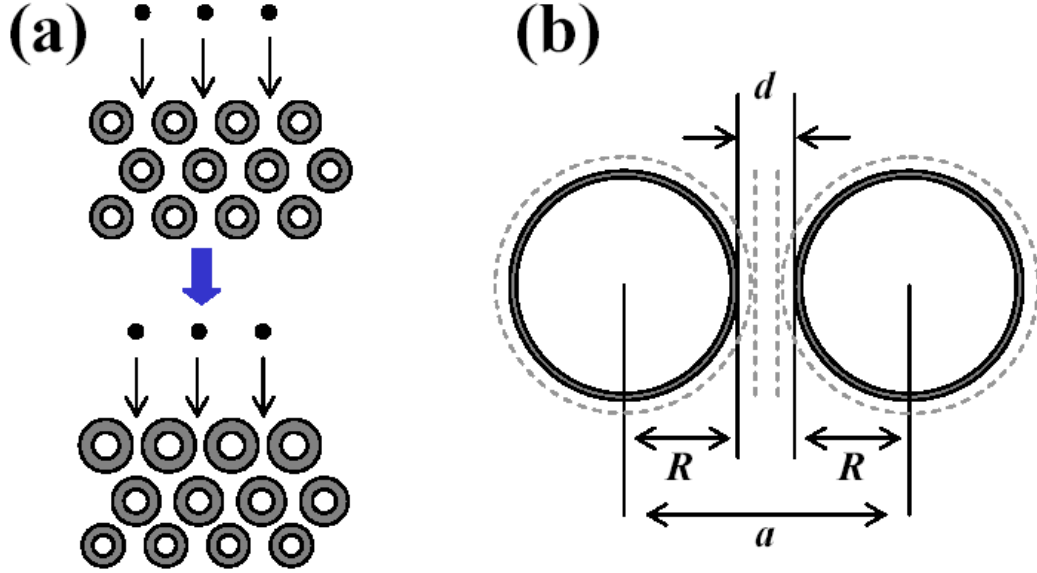


**Figure 4.1.** (a) Schematic of a SWCNT bundle exposed to an atomic H flux; the bundle is represented by a regular array of SWCNTs forming a hexagonal lattice on the plane normal to the SWCNT axes. The bundle is shown before (top) and after (bottom) its partial hydrogenation; the decrease in inter-tube spacing (bottom) is due to SWCNT swelling. (b) Characteristic dimensions of the bundle, namely SWCNT radius,  $R$ , SWCNT center-to-center distance,  $a$ , and inter-tube spacing,  $d$ . The dashed lines are used to indicate deformation due to SWCNT swelling upon hydrogenation.

The swelling function  $f(\Theta)$  is obtained by relaxing structures of pristine and hydrogenated SWCNTs of different diameters and chiralities at various coverages  $\Theta$  and calculating the resulting average  $R(\Theta)$ . Structural relaxation is based on isothermal-isobaric molecular-dynamics simulation using the AIREBO potential (Stuart et al., 2000; Brenner et al., 2002), following the same procedure described in Section 3.2 of Chapter

3, for H atoms distributed randomly on the SWCNT surfaces. Results for  $\Delta R(\Theta)/R_0$  are reported in Figure 4.2(a) by averaging over an ensemble of 5 distributions for the following nanotube configurations: one armchair (9,9) (with diameter  $D = 1.20$  nm at the pristine state), one chiral (13,4) ( $D = 1.19$  nm), and three zigzag (15,0), (20,0), and (24,0) ( $D = 1.16, 1.55,$  and  $1.85$  nm, respectively) SWCNTs. The trends observed were previously discussed in Chapter 3:  $\Delta R(\Theta)/R_0$  is negligible at lower  $\Theta$ , but beyond a critical  $\Theta$ , it increases monotonically with  $\Theta$ ; at higher  $\Theta$ , this monotonic increase becomes linear.

The results of Figure 4.2(a) show that for the smaller-diameter nanotubes [(9,9), (13,4), and (15,0) with  $D_{\text{average}} = 1.19$  nm],  $\Delta R(\Theta)/R_0$  depends on nanotube chirality only at higher  $\Theta$ . The results for the three zigzag nanotubes of different diameters show that  $\Delta R(\Theta)/R_0$  is practically independent of  $D$  within the range of diameters investigated. The dependence of  $\Delta R(\Theta)/R_0$  on diameter and chirality observed at high values of  $\Theta$  can be elucidated further by examining the dependence on  $D$  of  $\Delta R(\Theta = 1)/R_0$ , i.e., for fully hydrogenated CNTs, as shown in the inset of Figure 2(a). For smaller-diameter SWCNTs,  $\Delta R(1)/R_0$  depends on chirality, but for  $D > 1.3$  nm, the difference between the radial strains for SWCNTs of different chiralities is very small, and the increase in  $\Delta R(1)/R_0$  with  $D$  is only very slight.

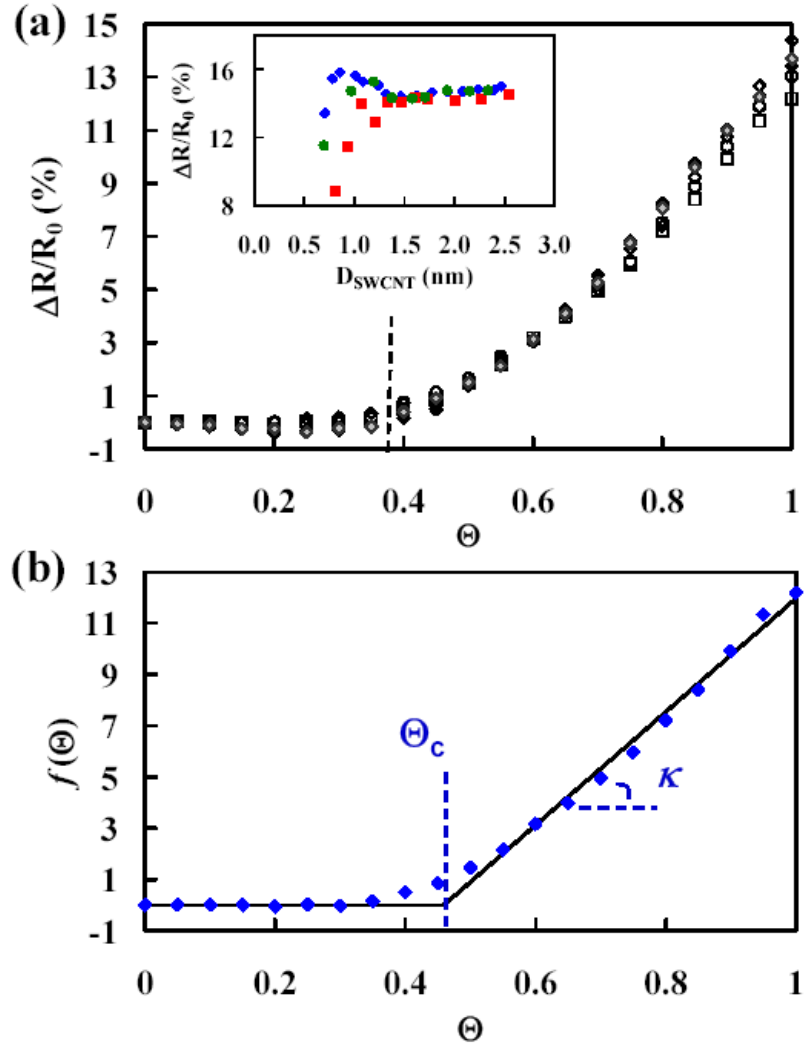


**Figure 4.2.** (a) Dependence on the H coverage  $\Theta$  of the radial strain  $\Delta R/R_0$  for the (24,0) (solid diamonds), (20,0) (gray diamonds), (15,0) (open diamonds), (9,9) (open squares), and (13,4) (open circles) SWCNTs. The inset shows the dependence of  $\Delta R/R_0$  on the pristine-SWCNT diameter for fully hydrogenated ( $\Theta = 1$ ) zigzag (solid diamonds), chiral (solid circles), and armchair (solid squares) nanotubes; the chiral SWCNTs examined have chiral angles ranging from  $13.0^\circ$  to  $18.3^\circ$ . (b) Least-squares fitting of the swelling function  $f(\Theta) = \kappa(\Theta - \Theta_c) H(\Theta - \Theta_c)$  (solid line) to the atomistic-simulation results (discrete symbols) for the (9,9) SWCNT.

Next, we introduce the simplest possible parameterization of the swelling function  $f(\Theta)$ . This involves a Heaviside step function,  $H$ , and two parameters: the critical coverage,  $\Theta_c$ , for the onset of swelling and the slope  $\kappa$  of  $f(\Theta)$  in the linear regime, i.e.,

over the high- $\Theta$  range where the function  $f(\Theta)$  is linear. The corresponding analytical expression is  $f(\Theta) = \kappa (\Theta - \Theta_c) H(\Theta - \Theta_c)$ . The validity of this parameterization in approximating the actual computed swelling function is demonstrated in Figure 4.2(b) through least-squares fitting of the analytical expression for  $f(\Theta)$  to the simulation results for  $f(\Theta)$  for the (9,9) SWCNT. The actual values of the parameters  $\kappa$  and  $\Theta_c$  depend on the diameters and chiralities of the carbon nanotubes. The least-squares estimates for the five sets of simulation results plotted in Figure 4.2(a) are:  $(\kappa, \Theta_c) = (0.221, 0.459)$ ,  $(0.234, 0.461)$ ,  $(0.259, 0.480)$ ,  $(0.253, 0.471)$ , and  $(0.249, 0.465)$  for the (9,9), (13,4), (15,0), (20,0), and (24,0) SWCNTs, respectively. These parameters  $(\kappa, \Theta_c)$  were also estimated for the sets of data presented in Figures 3.7 and 3.8 of Chapter 3, corresponding to SWCNTs of different diameters and chiralities, with H distributions obtained by the compositional relaxation procedure discussed in the same chapter. The results are summarized in Figure 4.3; they demonstrate that the strains induced by hydrogenation depend on nanotube chirality only for smaller-diameter CNTs, as discussed in the previous paragraph. For larger-diameter CNTs ( $D > \sim 1.8$  nm), dependence of the hydrogenation-induced strain on nanotube chirality and diameter becomes negligible.

Finally, with this parameterization for  $f(\Theta)$ , Eq. (1) yields the criterion

$$\delta(\Theta) = \alpha - 2\rho_0 [1 + \kappa(\Theta - \Theta_c) H(\Theta - \Theta_c)] \geq 1 \quad (4.2)$$

for efficient H diffusion in the carbon nanotube bundle.

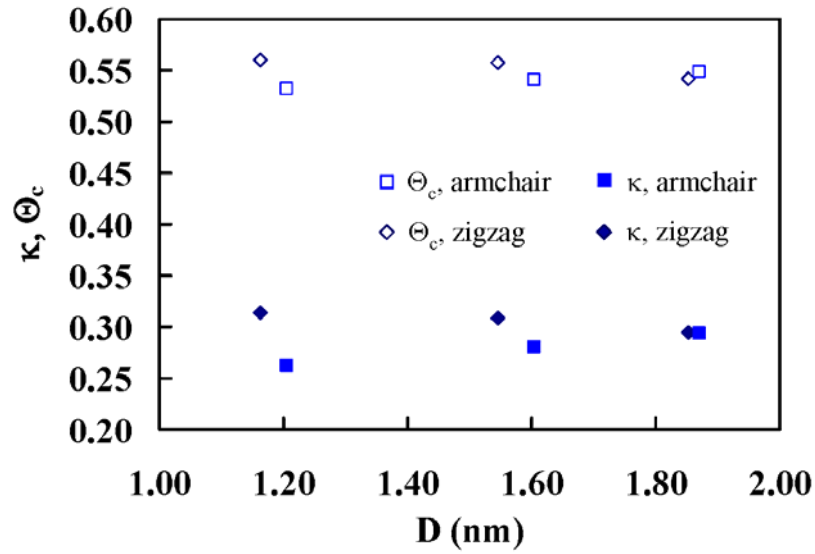


**Figure 4.3.** Estimated parameters  $\kappa$  and  $\Theta_c$  in the parameterization of the nanotube swelling function for SWCNTs of different diameters and chiralities.

Equation (4.2) can be used to investigate the dependence of  $\delta$  on the dimensionless lattice parameter  $\alpha$ , which is related to the bundle density  $\rho_b$ . In Figure 4.4(a),  $\delta(\Theta)$  is plotted for  $\rho_0 = 4.0$ ,  $\kappa = 0.240$ ,  $\Theta_c = 0.470$  and  $\alpha$  over the range  $9.1 \leq \alpha \leq 10.3$ . From this plot, it is evident that for dense bundles (low values of  $\alpha$ ), the criterion  $\delta > 1$  is satisfied for  $\Theta$  lower than a critical value. Considering that the outermost tubes are the first ones to be hydrogenated, this critical value of  $\Theta$  corresponds to the maximum degree of hydrogenation that can be achieved for the innermost tubes of the bundle. For the densest bundles represented in this figure, the extent of hydrogenation is only 50%. For more dispersed bundles (higher values of  $\alpha$ ), the maximum possible degree of hydrogenation (before  $\delta$  decreases to its critical value of 1), increases with increasing  $\alpha$ . If the nanotubes are dispersed enough, the H mass-transfer limitations are eliminated and the maximum storage capacity of the nanotube bundles can be achieved. However,

increasing  $\alpha$  causes a decrease in  $\rho_b$  and increases the footprint of the storage media for a given storage capacity; the relationship  $\rho_b \propto 1/a^2$  is depicted in the inset of Figure 4.4(a). Figure 4.4(b) shows that the maximum degree of hydrogenation realized may also depend on the atomic-scale characteristics of the nanotubes, namely their chiralities and diameters. For example, the variation of the parameter  $\kappa$ , which is determined by the SWCNT chirality and diameter, results in different ranges of  $\Theta$  which satisfy the criterion  $\delta(\Theta) > 1$ ; in Figure 4.4(b), we used two values of  $\alpha$  ( $\alpha = 9.4$  and  $\alpha = 9.7$ ),  $\Theta_c = 0.47$ ,  $\rho_0 = 4.0$ , and three representative values of  $\kappa$  ( $\kappa = 0.22$ ,  $0.24$ , and  $0.26$ ). By comparing the two cases, it is evident that for denser bundles the effects of SWCNT chirality and diameter are less pronounced than those for more dispersed bundles.

The swelling effect on individual nanotubes that our model considers has been studied before (Bauschlicher, 2001; Bauschlicher and So, 2002) and indicated the possibility of 100% coverage with half of the hydrogen inside and half outside the nanotubes. However, here, we have studied the effect for a more practical configuration of nanotube bundles by considering mass transfer limitations for the atomic hydrogen flux to reach the innermost tubes inside a bundle. A major implication of the model is that proper tailoring of the bundle density will improve the H storage capacity of carbon nanotubes substantially; this can be accomplished by lowering the bundle density to an optimal value that increases the degree of hydrogenation to  $\Theta = 1$ . In addition, the criterion of Eq. (4.2) is experimentally testable and provides a possible explanation for the observed storage capacities lower than 100% that have been reported in experiments.

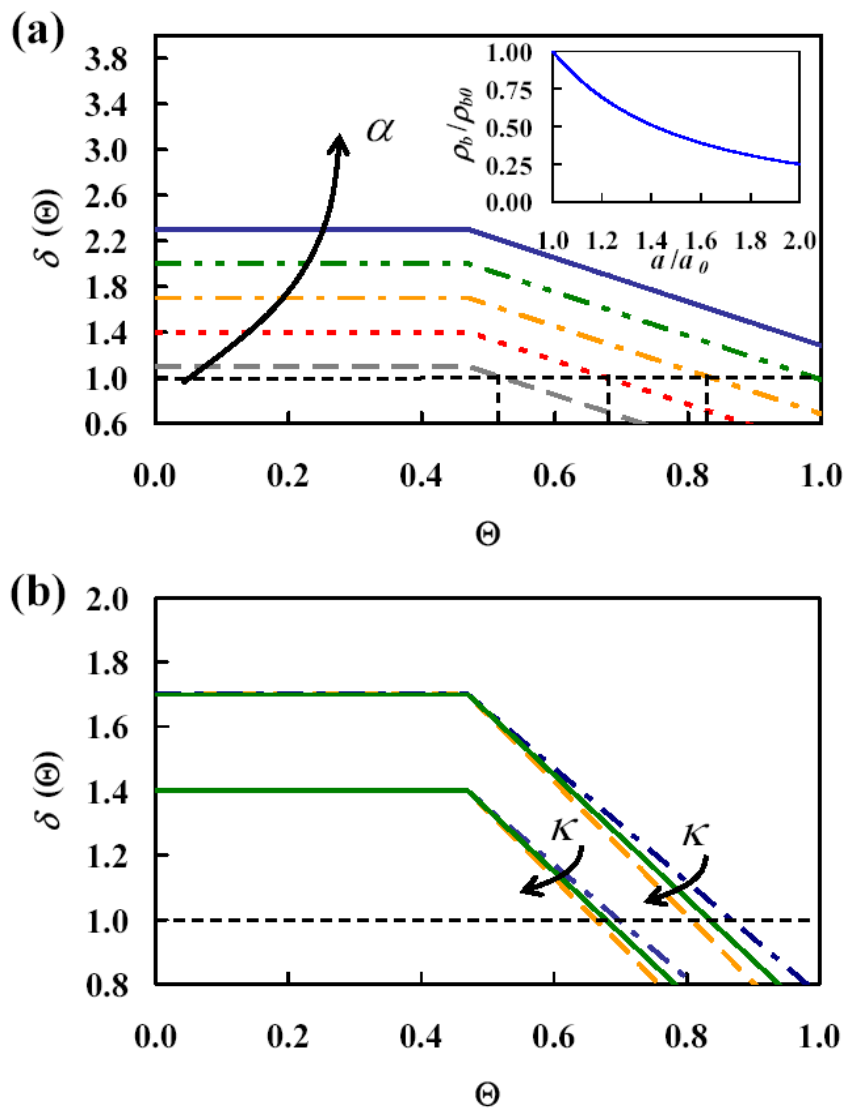


**Figure 4.4.** (a) Dimensionless inter-tube spacing  $\delta$  as a function of  $\Theta$  and its variation with the bundle density, as expressed by the dimensionless lattice parameter  $\alpha$ . The lines shown correspond to  $\alpha = 9.1, 9.4, 9.7, 10.0$ , and  $10.3$ . The inset shows the decrease of the bundle density as the lattice parameter increases; both quantities are made dimensionless with their values at the pristine state,  $\Theta = 0$ . (b)  $\delta$  as a function of  $\Theta$  for two bundle densities and its dependence on nanotube diameter or chirality, as expressed by the dimensionless parameter  $\kappa$ . The different lines in the two sets correspond to  $\kappa = 0.22, 0.24$ , and  $0.26$ .

Finally, we discuss our findings in the context of the experimental results. Ruffieux and coworkers (Ruffieux et al., 2002) reported a saturation in H uptake after 200 s, leveling off at 50% capacity. Nikitin and coworkers exposed several films of

SWCNTs to an atomic hydrogen beam and measured storage capacities of 65% (Nikitin et al., 2005) and of 30% and close to 100% (Nikitin et al., 2008). In this last study, the storage capacity of  $\sim 100\%$  of the second sample was achieved in the outermost nanotubes of the film and the hydrogenation of the sample was nonuniform; hydrogenation was practically uniform through the film for degrees of hydrogenation up to  $40\pm 5\%$ . These results are consistent with our model predictions, including the predicted values of  $\Theta_c$  ( $\sim 45\%$ ). The lowest reported hydrogen uptake is 20% for a 13- $\mu\text{m}$ -tall tower of SWCNTs grown on a silicon substrate (Tokura et al., 2008). According to our model, it is expected that, in this case, the degree of hydrogenation is low due to the very high density of the vertically aligned nanotubes in the tower and the associated difficulty for the atomic hydrogen flux to reach the nanotube surfaces at the bottom of the tower.

### 4.3 Summary and Conclusions

Our theoretical study shows how to circumvent mass transfer limitations in order to maximize the hydrogen storage capacity of SWCNT bundles and obtain a 7.0-8.0 wt% storage through atomic H chemisorption. However, practical considerations demand a careful evaluation of the energy penalty associated with the production of H atoms using a plasma or an atomic beam, particularly relative to *in situ* catalytic dissociation of  $\text{H}_2$ . Recent advances in atmospheric plasmas may offer an avenue to reduce this energy penalty.

## CHAPTER 5

### ANALYSIS OF DIAMOND NANOCRYSTAL FORMATION ON MULTI-WALLED CARBON NANOTUBES FROM INTER-SHELL BONDING

#### 5.1 Introduction

Hydrogen atoms play a critical role in determining the crystallinity of group-IV materials grown by plasma deposition. For example, nucleation and growth of diamond thin films by plasma deposition from hydrocarbons is possible only when the feed gases are heavily diluted in H<sub>2</sub> or under conditions where atomic H is present in copious amounts (Lambrecht et al., 1993; Angus and Hayman, 1988). Another example is the amorphous-to-nanocrystalline transformation of hydrogenated silicon thin films upon exposure to H atoms from a H<sub>2</sub> plasma (Layadi et al., 1995; Sriraman et al., 2002). Furthermore, nanometer-size diamonds have been formed from multi-walled carbon nanotubes (MWCNTs) and carbon onions by exposure to H atoms from a H<sub>2</sub> plasma or electron beam exposure at or above 1000 K (Banhart and Ajayan, 1996; Sun et al., 2004a, b; Wen et al., 2005; Yang et al., 2007); interactions of H atoms with MWCNTs have been speculated to be responsible for the transformation of MWCNT walls to diamond nanocrystals (Sun et al., 2004a, b; Yang et al., 2007). The underlying mechanism of the H-induced structural transition in MWCNTs leading to nanocrystalline carbon is not well understood. However, several possible mechanisms for this transition have been proposed, such as the formation of H-induced *sp*<sup>3</sup> defects in carbon nanotube walls with implications for formation of nanocrystalline carbon (Barnard et al., 2005). The

interactions of H atoms with the graphene walls of MWCNTs can trigger  $sp^2 \rightarrow sp^3$  C-C bonding transitions. These  $sp^3$  bonded local structures induced by hydrogen atoms or electron irradiation in MWCNTs can promote inter-shell C-C bonding and have been implicated to enhance material properties of MWCNTs (Peng et al., 2008; Byrne et al., 2009).

The stability of diamond nanocrystals and its size dependence has been discussed extensively in the literature (Badziag et al., 1990; Hwang et al., 1996; Jiang et al., 2000; Barnard et al., 2003a, b); specifically, diamond nanocrystals have been shown to be the most stable phase of carbon at the nanoscale for clusters with diameters ranging from  $\sim 1.9$  to  $\sim 5.2$  nm (Barnard et al., 2003a). The stability of the one-dimensional equivalent nanostructures, namely diamond nanowires, both monolithic and in the form of hollow cylinders, also has been investigated thoroughly (Menon et al., 2000; Shenderova et al., 2003; Barnard et al., 2003b, 2004; Ivanovskaya et al., 2007). It has been demonstrated that the stability of these nanowires is a function of their diameter, their surface morphology, as well as the crystallographic direction of their principal axes. The above-mentioned studies refer to isolated nanocrystals (Badziag et al., 1990; Hwang et al., 1996; Jiang et al., 2000; Barnard et al., 2003a) or practically infinitely long diamond nanowires (Menon et al., 2000; Shenderova et al., 2003; Barnard et al., 2003b, 2004; Ivanovskaya et al., 2007). Here, we focus on the formation of diamond nanostructures consisting of diamond nanocrystals embedded into MWCNTs.

The purpose of this chapter is to analyze the structures generated as a result of the inter-shell C-C bonding of adjacent, concentric graphene walls of MWCNTs. We demonstrate that these structures can provide seeds for the nucleation of cubic and

hexagonal diamond nanocrystals and that the chirality and relative alignment of the adjacent MWCNT graphene walls determine the lattice structure of the resulting crystalline phase. In addition, we show that the formation of diamond nanocrystals is possible over the broadest range of nanotube diameters and through any arrangement of adjacent graphene walls, i.e., for all possible combinations of zigzag, armchair, or chiral graphene wall configurations to within a certain range of the difference in the chiral angles between adjacent graphene walls in the MWCNT.

The chapter is structured as follows. Section 5.2 outlines the computational methods employed in our analysis of inter-shell C-C bonding in MWCNTs, including first-principles density functional theory (DFT) calculations and structural relaxation based on molecular-dynamics (MD) simulation. In Sections 5.3, 5.4 and 5.5, the results of our analysis are presented and discussed. In Section 5.3, a systematic presentation is given of all the relevant geometrical aspects of C-C bond formation between adjacent concentric graphene walls by spanning the entire space of geometrical parameters as determined by the indices  $(m,n)$  of the individual nanotubes involved; our DFT calculations of inter-shell C-C bonding in MWCNTs and analysis of the resulting relaxed structures are presented in Section 5.4; our MD computations of structurally relaxed seeds for nucleation of crystalline carbon phases through inter-shell C-C bonding in MWCNTs are presented in Section 5.5. Finally, the main conclusions of our study are summarized in Section 5.6.

## 5.2 Computational Methods

The first step in our analysis consists of a general, systematic geometrical study of adjacent concentric graphene walls in MWCNTs focusing on the range of possibilities for inter-shell C-C bonding and its implications for the crystalline structures that can be nucleated through such a process; this is presented in Section 5.3. Subsequently, we use a synergistic combination of MD simulations with first-principles DFT calculations in order to relax fully and characterize in detail the nanostructures that can be nucleated as a result of such bond formation.

First-principles DFT calculations were conducted within the generalized gradient approximation (Perdew et al., 1996), employing the supercell approximation, ultra-soft pseudopotentials (Vanderbilt, 1990), and plane-wave basis sets as implemented in the commercial code VASP (Kresse and Furthmuller, 1996). This level of theoretical calculations was used for the study of inter-shell interactions and C-C bonding between adjacent graphene walls in MWCNTs, as well as the detailed analysis of bulk crystalline carbon phases. The results of inter-shell C-C bonding reported in Section 5.4 are based on DFT calculations that employed a supercell consisting of 180 C atoms arranged to form three concentric CNTs with indices (6,0), (15,0), and (24,0), i.e., a (6,0)@(15,0)@(24,0) CNT configuration, a vacuum region between neighboring (periodic-image) MWCNTs that was at least 15 Å in thickness, and continuity in the axial direction. In addition, we conducted DFT calculations of inter-shell C-C bonding and the formation of nanocrystalline seeds for nucleation of the cubic-diamond and hexagonal-diamond (lonsdaleite) phases in CNTs of larger diameters up to 1.4 nm and confirmed that the curvature effects were minimal on the outcome of this analysis. In particular, for

concentric CNTs with indices (6,0)@(15,0) and (18,0)@(27,0), with spacing between the CNT walls of 3.53 Å, nuclei for crystalline carbon phases were generated as well through inter-shell C-C bonding.

The results reported in Section 5.4 are based on DFT calculations with a kinetic energy cut-off of 350 eV and two  $\mathbf{k}$  points in the relevant irreducible wedge of the first Brillouin zone. To calculate the total energies of the geometrically optimized configurations, the supercell was relaxed using a conjugate gradient algorithm until the differences in electronic and ionic self-consistent energies were lower than  $10^{-3}$  eV and  $10^{-2}$  eV, respectively. In all of our DFT calculations, systematic convergence tests were conducted (with respect to supercell size, kinetic-energy cut-off, and  $\mathbf{k}$ -point grid resolution) in order to guarantee the precision of the reported results. In both MWCNTs with inter-shell C-C bonding and bulk crystalline carbon phases, the local bonding environment also was analyzed by visualizing planar sections of the three-dimensional valence electron density distribution.

In our MD simulations of inter-shell C-C bonding and accompanying structural relaxation, the interatomic interactions were described by the Adaptive Intermolecular Reactive Empirical Bonding Order (AIREBO) potential (Stuart et al., 2000), introduced in Chapter 2 and presented in details in Appendix A. All the MD simulations were conducted at constant temperature and (zero) pressure using the Berendsen thermostat and barostat for temperature and pressure control (Berendsen et al., 1984). In our MD computations of inter-shell C-C bonding, periodic boundary conditions were applied in the axial direction of the CNTs.

We have tested and validated the AIREBO potential predictions extensively for their quantitative accuracy through comparisons with first-principles DFT calculations for the structure and properties of bulk crystalline and hydrogenated carbon phases; the results are discussed in Appendix A. In addition, we have carried out systematic comparisons between our AIREBO-MD predictions of fully relaxed structures resulting from inter-shell C-C bonding in MWCNTs and the corresponding predictions of our DFT calculations for the same MWCNT configurations. In general, the AIREBO predictions are in excellent qualitative agreement and in very good quantitative agreement with the DFT calculations; the agreement is excellent in comparing overall structure, average bond lengths and bond angles, and energetic ordering (relative stability) of crystalline phases and it is very good in comparing lattice parameters, individual bond lengths and bond angles, and energy differences between crystalline phases.

### **5.3 Geometrical Parameters Controlling C-C Bonding Between Adjacent Graphene Walls of MWCNTs**

First, we conducted a systematic geometrical analysis to map out the range of possibilities for inter-shell C-C bonding and considered the implications of such bonding for the resulting crystalline structures. Such a geometrical analysis provides general fundamental principles for the possible atomic structures that may be formed through inter-shell C-C bonding, regardless of the level of theory involved in the description of interatomic interactions. This generality can be achieved by spanning the space of parameters responsible for the geometrical features of each individual, concentric nanotube in the MWCNT; this parameter space is determined by each individual

nanotube's indices  $(m,n)$ . The only constraint in this geometrical analysis is that the spacing between adjacent nanotubes in the MWCNT is kept at  $\sim 3.4 \text{ \AA}$ ; this intertube spacing is consistent with experimentally measured distances between adjacent graphene walls in MWCNTs, as well as between parallel graphene sheets in graphite (Dresselhaus et al., 1996, 2001).

Initially, we consider such geometrical possibilities by examining parallel planar sheets of graphene and then generalize the analysis to the curved space of MWCNTs. Figure 5.1 shows three possible alignments between two adjacent graphene planes together with the relaxed structures generated, in each case of alignment, by the formation of inter-planar C-C bonds; how the structural relaxation has been carried out (i.e., from first principles or according to an empirical force field) is of secondary importance for this discussion. In the configuration of Figure 5.1(a), the relative positions of the hexagonal cells of each plane show that the two graphene planes are displaced with respect to each other in the  $y$ -direction of a Cartesian frame of reference by a distance equal to one side length of the regular hexagon; these hexagonal cells correspond to graphene 6-member rings consisting of  $sp^2$ -bonded C atoms and the side of the regular hexagon has length equal to the  $sp^2$  C-C bond length. In the configuration of Figure 5.1(b), the hexagonal cells of the two parallel graphene planes overlap fully when projected onto the same  $(x,y)$  plane normal to the  $z$ -direction. In the configuration of Figure 5.1(c), the two graphene planes are displaced with respect to each other in the  $y$ -direction by one half of the  $sp^2$  C-C bond length. In the bonded configurations shown in Figures 5.1(a) and 5.1(b), the C-C bonds form in the  $z$ -direction between inter-planar nearest neighbors. In Figure 5.1(a), the inter-planar bonded region resembles closely the

structure of the cubic-diamond phase and can be viewed as a seed unit for the nucleation of this phase from interacting graphene planes. In contrast, the inter-planar bonded region of Figures 5.1(b) and 5.1(c) resemble the structure of the hexagonal-diamond phase (lonsdaleite) and can be viewed as seed units for hexagonal diamond formation due to the inter-planar interactions of parallel graphene sheets.

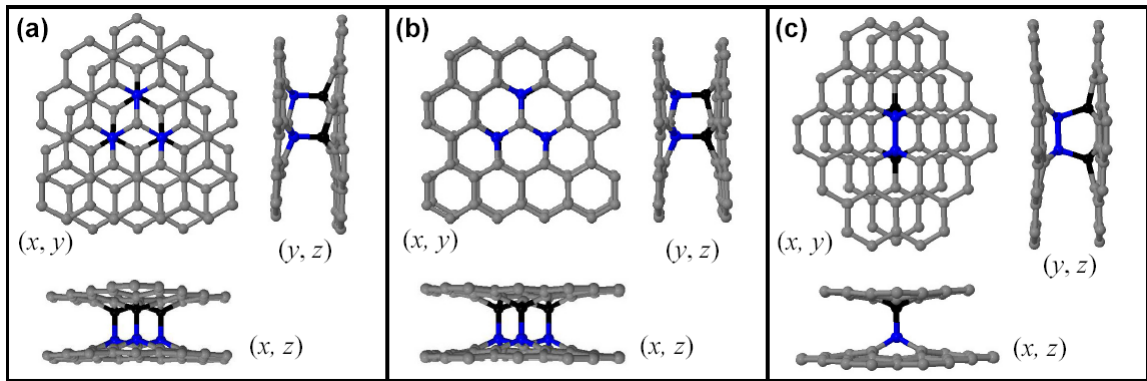


**Figure 5.1.** Three possible alignments, (a), (b), and (c), between two adjacent graphene planes and respective local structures generated by the formation of inter-planar C–C bonds. In each case, different planar views are displayed in a Cartesian frame of reference. Blue and black spheres are used to denote C atoms on the two adjacent graphene planes, respectively, that are bonded to each other.

Compared to the case of parallel graphene planes, the number of geometrical possibilities is much larger in MWCNTs. Specifically, in a MWCNT, for a given pair of adjacent concentric graphene walls of given chiralities, it is possible to find regions characterized by each one of the relative alignments depicted in Figure 5.1. Consequently, in the same MWCNT, different types of local crystalline structures may be generated due to inter-shell C–C bonding, depending on the local alignment of the graphene walls at the sites bridged by the inter-shell C–C bonds; these structures may grow to form nanocrystals separated by phase boundaries. For illustration purposes, we

consider the simplest possible case, namely double-walled CNTs (DWCNTs) with two concentric graphene walls of the same chirality.

To identify the type of local crystalline structure that is the most likely to be formed in a certain region of the DWCNT around a chosen point at the outer graphene wall, we use images that represent “relative alignment maps”; for a given pair of nanotube walls, these maps depict the regions of the DWCNT where a certain relative alignment between the walls is found according to detailed geometrical criteria. Figure 5.2(a) shows the top view of such a relative alignment map for two pairs of armchair nanotubes arranged concentrically; a larger one, (50,50)@(55,55), and a smaller one, (30,30)@(35,35). In each of these pairs of nanotubes, the alignments of the atoms marked in black and blue with respect to their nearest neighbors in the adjacent nanotube are consistent with those depicted in Figure 5.1(a) and Figure 5.1(b), respectively, for neighboring atoms between adjacent graphene planes; these are denoted as type-I and type-II alignment, respectively. It is evident that the same type of relative alignment can be found in different regions of the nanotube. For the case under consideration, the clusters of atoms with the same relative alignment with respect to their neighbors in the adjacent nanotube have a finite size in the  $\theta$ -direction and an infinite size along the nanotube axis (i.e., limited by the actual CNT length);  $\theta$  is the polar angle in a cylindrical-coordinate description of the CNTs, ranging from 0 to  $2\pi$ , with the nanotube axis taken along the  $z$ -direction. Figures 5.2(b) and 5.2(c) show close planar views for two distinct regions of the DWCNT, highlighting the two different types (II and I, respectively) of relative alignment.

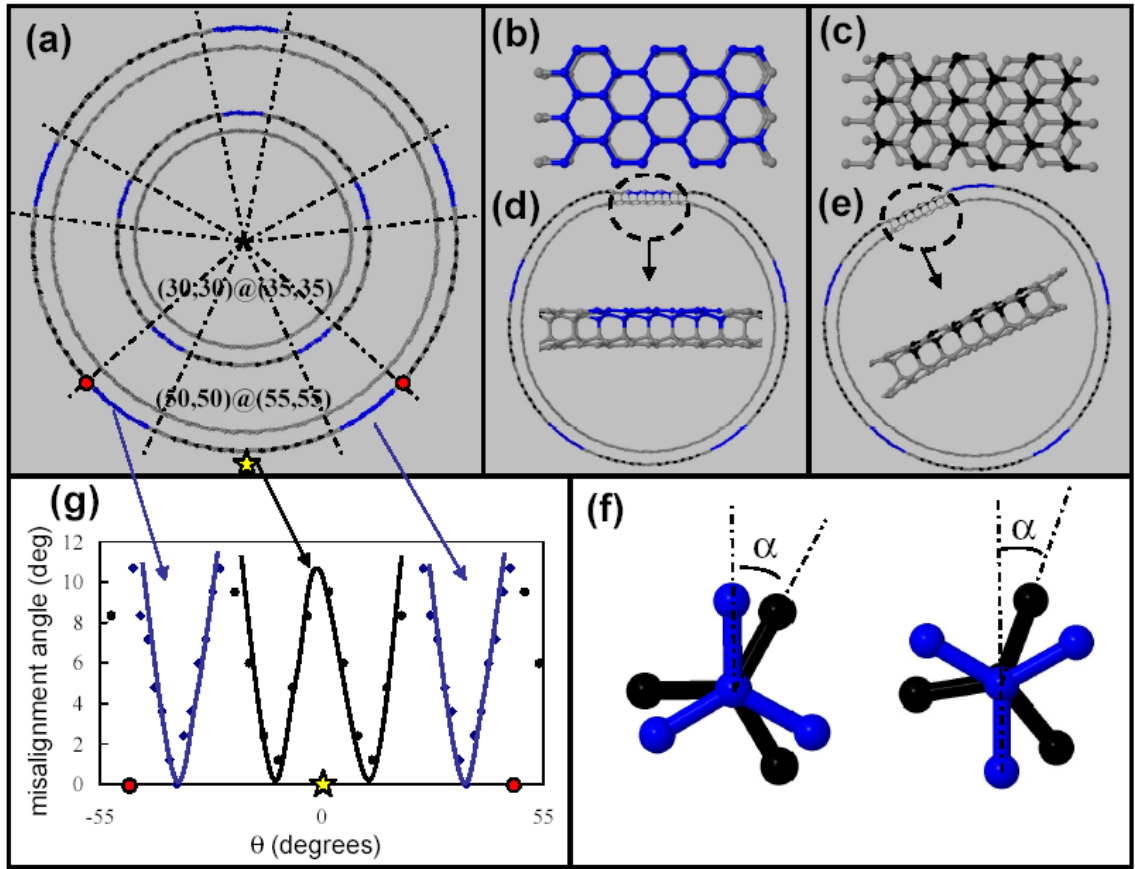


**Figure 5.2.** (a) Top view of relative alignment maps for two pairs of armchair nanotubes,  $(30,30)@(35,35)$  and  $(50,50)@(55,55)$ , arranged concentrically. The dotted lines are used to mark the regions (a total of ten) where a certain alignment, type I or type II, is favored. (b, c) Front views of the  $(50,50)@(55,55)$  DWCNT in (b) a region where type-II alignment is favorable and (c) a region where type-I alignment is favorable. (d, e) Top views of the  $(50,50)@(55,55)$  DWCNT with close views of the local structures generated by inter-shell C-C bond formation in (d) one of the regions colored blue in (a) where type-II alignment is favorable and (e) one of the regions colored black in (a) where type-I alignment is favorable. (f) Angle  $\alpha$  used for determining the possible alignment type according to the criteria described in the text. (g) Misalignment angle between nearest-neighbor atoms in different adjacent concentric nanotube graphene walls as a function of the polar angle  $\theta$  in a cylindrical frame of reference for the sections marked in (a).

Figure 5.2(a) also shows that the clusters of atoms with each type of relative alignment between graphene walls occur periodically as the circumference of the DWCNT is spanned along  $\theta$ . For a pair of armchair nanotubes, there are five regions with type-I alignment and five regions with type-II alignment in a pattern of alternating

alignment type (...I-II-I-II...). In a MWCNT, this number of regions is the same for any pair of adjacent armchair nanotubes, which satisfies the requirement of having an intertube spacing of  $\sim 3.4$  Å; for concentric armchair configurations, this spacing corresponds to combinations of  $(n,n)@(n+5,n+5)$  graphene walls. As the diameter of the nanotube increases, the size of each individual region (cluster of atoms with given-type alignment) also increases; however, the number of such regions remains always the same. This trend is evident in Figure 5.2(a).

Figures 5.2(d) and 5.2(e) depict the local structures resulting from the creation of inter-shell C-C bonds in two different regions among the ten ones shown in Figure 5.2(a) for the  $(50,50)@(55,55)$  DWCNT; these structures have been relaxed after bonding using AIREBO MD. The inter-shell bonded structure of Figure 5.2(d) corresponds to a type-II alignment and resembles the lattice structure of the hexagonal-diamond phase, while that of Figure 5.2(e) corresponds to a type-I alignment and resembles the lattice structure of the cubic-diamond phase.

Analogous patterns also occur in pairs of adjacent zigzag graphene walls. However, in such an arrangement of nanotubes, there are nine regions with specific alignment in a pattern of alternating alignment types (as opposed to five in the case of armchair graphene walls discussed above). This is the case for any pair of adjacent zigzag nanotubes in a MWCNT where the inter-tube spacing is  $\sim 3.4$  Å; for concentric zigzag configurations, this spacing corresponds to combinations of  $(n,0)@(n+9,0)$  graphene walls.

It should be emphasized that, over the extent of each region marked in the relative alignment maps, the relative alignment between the adjacent graphene walls is not as

perfect as depicted in the planar geometry of Figure 5.1. There may be slight deviations from the ideal alignment of each type, which still facilitate the formation of the corresponding inter-shell bonded local structures. To determine the relative alignment type that is most suitable for a given atom on a wall of the DWCNT, we used two criteria. To apply the first criterion, we find the atom in the outer layer that is the closest to a given atom in the inner layer, as well as the relative orientation of the (three)  $sp^2$  C-C bonds formed by each one of these atoms in the individual nanotubes. If the  $sp^2$  bonds in one graphene wall are parallel to those in the other wall and point (outwards from the atom under consideration) to the same direction, a type-II alignment is favored; on the other hand, if the  $sp^2$  bonds in the two graphene walls are parallel but point to opposite directions, a type-I alignment is favored. A tolerance must be prescribed in assessing the bonds as being “parallel”. Structural relaxations on bonded graphene planes showed that deviations from being parallel up to angles  $\alpha = 30^\circ$  allow the formation of inter-planar C-C bonds; this angle  $\alpha$  is depicted in Figure 5.2(f) for both types of alignment. The second necessary criterion is derived from the angle  $\beta$  formed between the line connecting the inter-shell nearest-neighbor pair of atoms and the projection of the atom of the inner layer on the outer one along the radial direction, which is used as a metric for the degree of alignment. For two perfectly aligned points, the aforementioned projected point and the nearest-neighbor atom in the outer layer coincide and  $\beta = 0$ . By analyzing the relative alignment of atoms for two graphene walls of the same chirality, we can define a maximum misalignment angle that determines the preference for a certain type of relative alignment. This critical value corresponds to an atom of the inner graphene wall that forms the same angle with two different neighboring atoms of the outer graphene wall,

with each one resulting in a different type of alignment (I or II) after inter-shell bonding. Figure 5.2(g) shows the dependence of this misalignment angle on the polar coordinate  $\theta$  of the atoms on the outer nanotube; the star marked in Figure 5.2(a) corresponds to  $\theta = 0^\circ$ . Three curves are identified in the plot of Figure 5.2(g), corresponding to the regions marked in Figure 5.2(a). The central atom of each blue region in the outer tube is aligned perfectly with an atom in the inner tube (a misalignment angle of  $0^\circ$ ), corresponding to the minimum of each blue curve. The misalignment angle increases as  $\theta$  changes from its value at that central point, until the type of alignment changes. For the black regions, the plotted curve exhibits two minima, corresponding to two regions of the same alignment connected to each other with a maximum (essentially a discontinuity) at the middle point.

One important point that should be considered is that, in an actual MWCNT, two adjacent graphene walls do not necessarily have the same chirality. It has been observed experimentally that there is no correlation between the chiral angles,  $\chi$ , of adjacent graphene walls in MWCNTs (Hashimoto et al., 2005); in addition, the difference between the chiral angles of each nanotube can range from small to large values. However, we can show that it is possible to find the same types of relative alignment discussed above for pairs of graphene walls of different chiralities, provided that the difference in the chiral angle between the two walls,  $\Delta\chi \equiv |\chi_{\text{inner}} - \chi_{\text{outer}}|$ , is not too large.

At this point, it is worth pointing out the analogy between our relative alignment maps and the concept of the Moiré pattern that results from the rotation of one graphene plane with respect to another: this leads to a new periodic structure that has the same symmetry with the original hexagonal lattice, but a larger periodicity; the observation of

superlattices on graphite and few-layer graphene in scanning tunneling microscopy (STM) images (Kuwabara et al., 1990; Xhie et al., 1993; Rong and Kuiper, 1993; Pong and Durkan, 2005; Hass et al., 2008; Varchon et al., 2008; Warner et al., 2009; Singh et al., 2010) is attributed to such Moiré patterns. The unit cells of these Moiré patterns have been shown to correspond to domains of the structure with a certain type of stacking of two subsequent planes (Xhie et al., 1993; Rong and Kuiper, 1993). In other words, if two adjacent graphene planes are rotationally misoriented, the three types of alignment depicted in Figure 5.1 will be present in the structure (at least until a limiting angle value, as discussed later), as illustrated in Figure 5.3, where Moiré patterns corresponding to pair of planes rotated by angles from  $\phi = 3.89^\circ$  to  $16.83^\circ$  are presented.

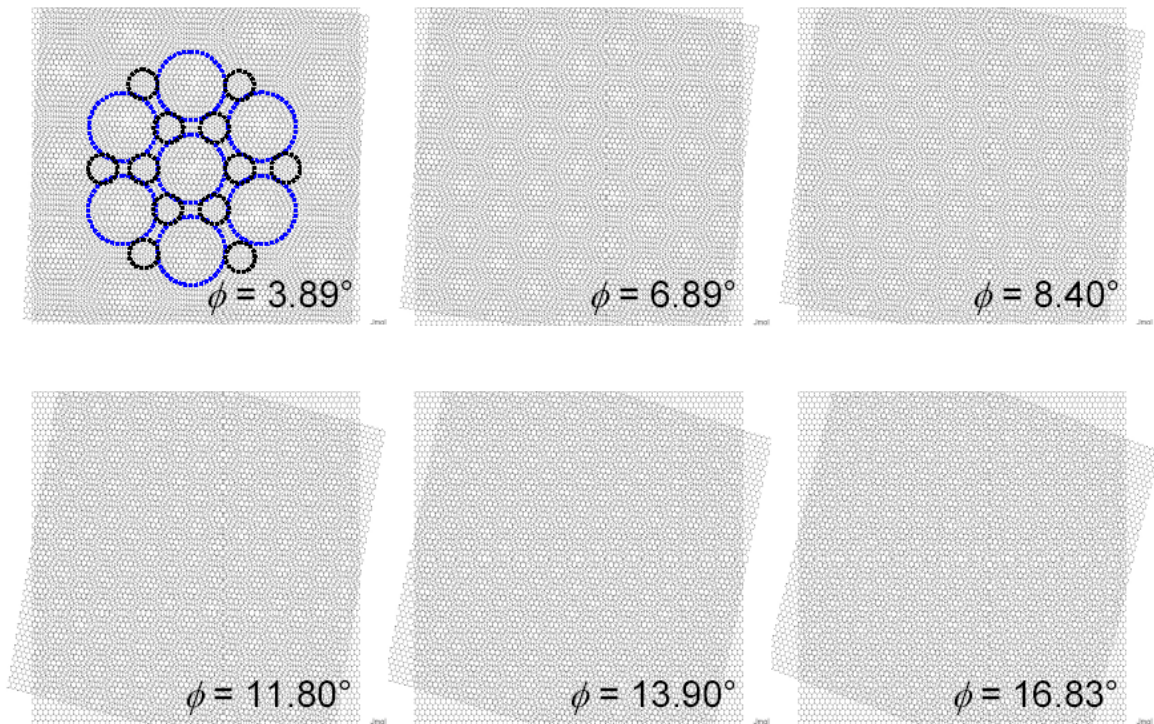


**Figure 5.3.** Moiré patterns for pairs of graphene planes rotated by different angles. For the case  $\phi = 3.89^\circ$ , the regions characterized by alignments of types I (Figure 5.1(a)) and II (Figure 5.1(b)) are marked with dotted circles in black and blue respectively; the interstitials between these domains are characterized by the alignment observed in Figure 1(c).

The periodicity of the resulting Moiré superperiodic lattice,  $D$ , is related to the periodicity of the original hexagonal lattice,  $d$ , by the expression  $D = d/[2\sin(\phi/2)]$ , where  $\phi$  is the rotation angle. In the case of DWCNTs,  $\phi$  corresponds to the difference in the chiral angles between the adjacent layers,  $\Delta\chi$ . The Moiré pattern periodicity,  $D$ , can be related to the size of the resulting domains with a certain relative alignment for a given value of  $\Delta\chi$ . However, in the curved space of CNTs, a direct application of this rule is not trivial in the sense that quantitative differences arise in different cases (different tube diameters, chiralities, and misalignment angle variations). Consequently, in our analysis, we relied on numerical determination of the relative alignment maps and the sizes of the resulting domains/clusters following the same methodology employed in the case where two adjacent walls have the same chirality (analogous to aligned planes or  $\phi = 0$ ).

To demonstrate the possibility of finding the same types of relative alignment (types I and II) for pairs of graphene walls of different chiralities, relative alignment maps analogous to those depicted in Figure 5.2(a) were generated for a broad range of combinations of graphene walls; this included zigzag@chiral, armchair@chiral, and chiral@chiral DWCNTs for different diameters and different values of  $\Delta\chi$ . The CNT indices for the various pairs of walls were chosen to satisfy the constraint that the inter-tube spacing must be  $\Delta r \sim 3.4 \text{ \AA}$  (in this study, we used  $\Delta r = 3.45 \pm 0.10 \text{ \AA}$ ). Relative alignment maps for different combinations of DWCNT indices are shown in Figures 5.4-5.6. From these maps, it is evident that for a pair of graphene walls with a chiral-angle difference  $\Delta\chi \neq 0$ , the regions of atoms with the same inter-shell alignment type are finite in size and form clusters arranged in a periodic pattern throughout the nanotube. Figure 5.4 shows maps for pairs of chiral nanotubes with practically the same average diameter

D and  $\Delta\chi$  ranging from  $3.88^\circ$  to  $16.8^\circ$ . From the analysis of these maps, we conclude that the size of the clusters of atoms with the same type of relative alignment depends strongly on the value of  $\Delta\chi$ ; specifically, the cluster size increases as  $\Delta\chi$  decreases. Obviously, when  $\Delta\chi \rightarrow 0$  (cases analyzed in Figure 5.2), the resulting regions have an infinite size (i.e., limited by the actual CNT length).

Figure 5.5 shows that the size of these clusters does not change appreciably as the average DWCNT diameter increases. In conjunction with the results of Figure 5.4, this trend implies that the size of the local inter-shell bonded structures is limited only by the chiral-angle difference  $\Delta\chi$ . Consequently, nanotubes of larger diameter are characterized by a larger number of clusters of atoms with certain alignment, but not of larger size. Figure 5.6 demonstrates that the size of these clusters is independent of the individual chiral angles  $\chi$  of the adjacent graphene walls; in summary, combining the results of Figures 5.4, 5.5 and 5.6 leads to the conclusion that the chiral-angle difference  $\Delta\chi$  is the key parameter that determines the maximum size of the clusters with the same type of inter-shell alignment.

From the analysis of the maps of Figure 5.4, it is evident that the size of the regions aligned according to the same type decreases abruptly as  $\Delta\chi$  increases. Around a value of  $\Delta\chi = 16^\circ$ , the number of atoms in such a cluster decreases to six, i.e., enough to form just three inter-shell bonds such as those in the structures of Figure 5.1. In order to quantify this trend, the dependence on the chiral-angle difference  $\Delta\chi$  of the maximum size of clusters with type-II alignment (blue regions) is plotted in Figure 5.7. For all the DWCNT diameters examined, the cluster size is determined from the number of

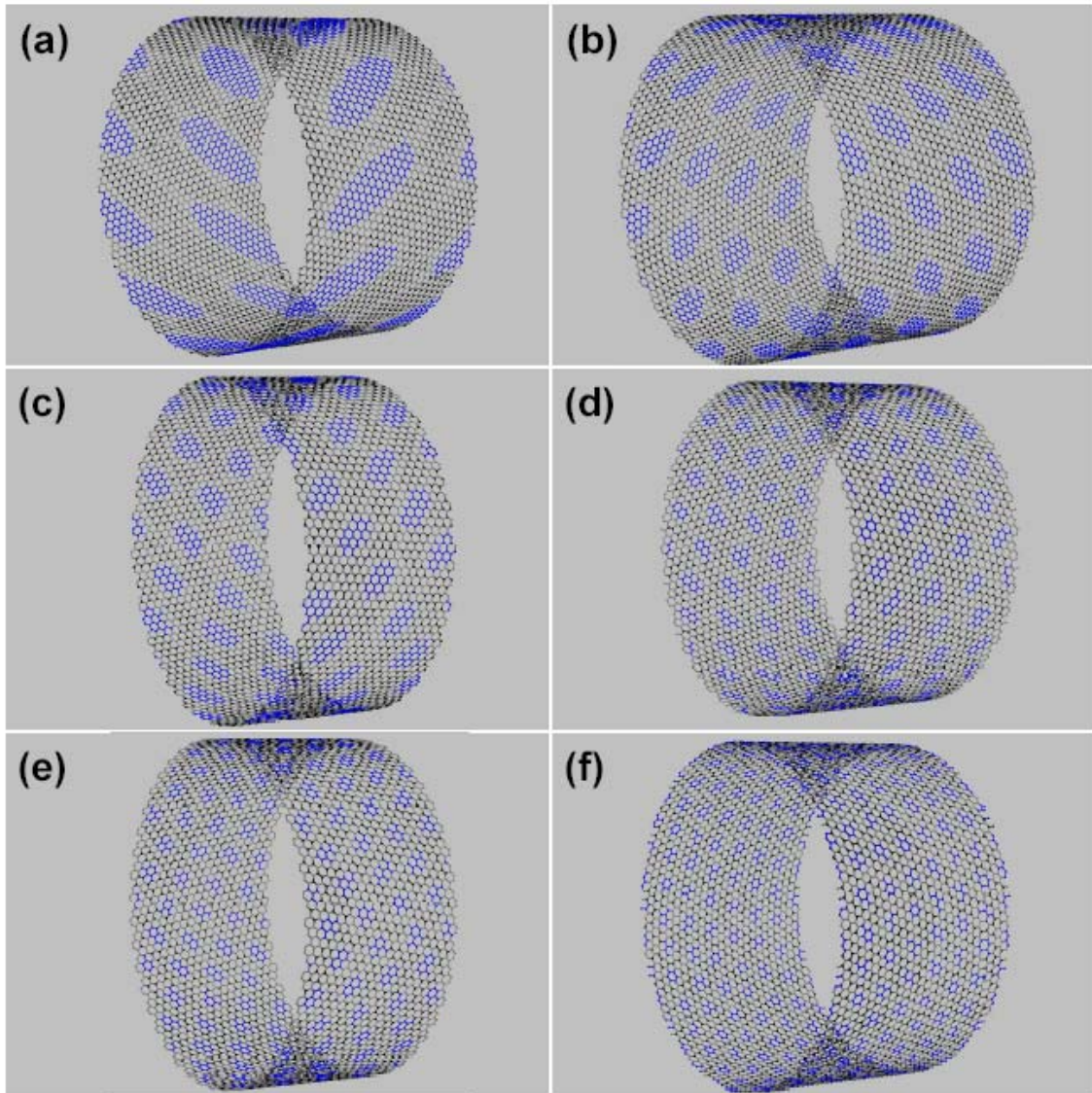


**Figure 5.4.** Relative alignment maps for DWCNTs formed by two chiral nanotubes with a difference in the chiral angles,  $\Delta\chi$ , varying from  $3.88^\circ$  to  $16.8^\circ$  and an average diameter,  $D$ , of approximately 8.9 nm. The blue and black colored regions correspond to atoms with inter-shell alignments as depicted in Figures 5.1(b) and 5.1(a), respectively, which favor the formation of hexagonal-diamond and cubic-diamond seeds, respectively. Only the outer nanotubes are shown for clarity. The DWCNTs have indices (a)  $(87,29)@(88,40)$  with  $D = 8.88$  nm and  $\Delta\chi = 3.89^\circ$ ; (b)  $(80,40)@(98,28)$  with  $D = 8.97$  nm and  $\Delta\chi = 6.89^\circ$ ; (c)  $(85,34)@(77,55)$  with  $D = 8.99$  nm and  $\Delta\chi = 8.40^\circ$ ; (d)  $(99,9)@(90,36)$  with  $D = 8.80$  nm and  $\Delta\chi = 11.80^\circ$ ; (e)  $(99,11)@(86,43)$  with  $D = 8.91$  nm and  $\Delta\chi = 13.90^\circ$ ; and (f)  $(72,48)@(105,15)$  with  $D = 8.87$  nm and  $\Delta\chi = 16.83^\circ$ .

hexagonal cells in the regions under consideration. For each DWCNT, the size of the blue regions is the same as that of the black regions. This plot also emphasizes our previous conclusion that the sizes of the local inter-shell bonded structures, as measured by the size of same-alignment inter-shell clusters, are limited only by the chiral-angle difference  $\Delta\chi$  of the adjacent graphene walls.

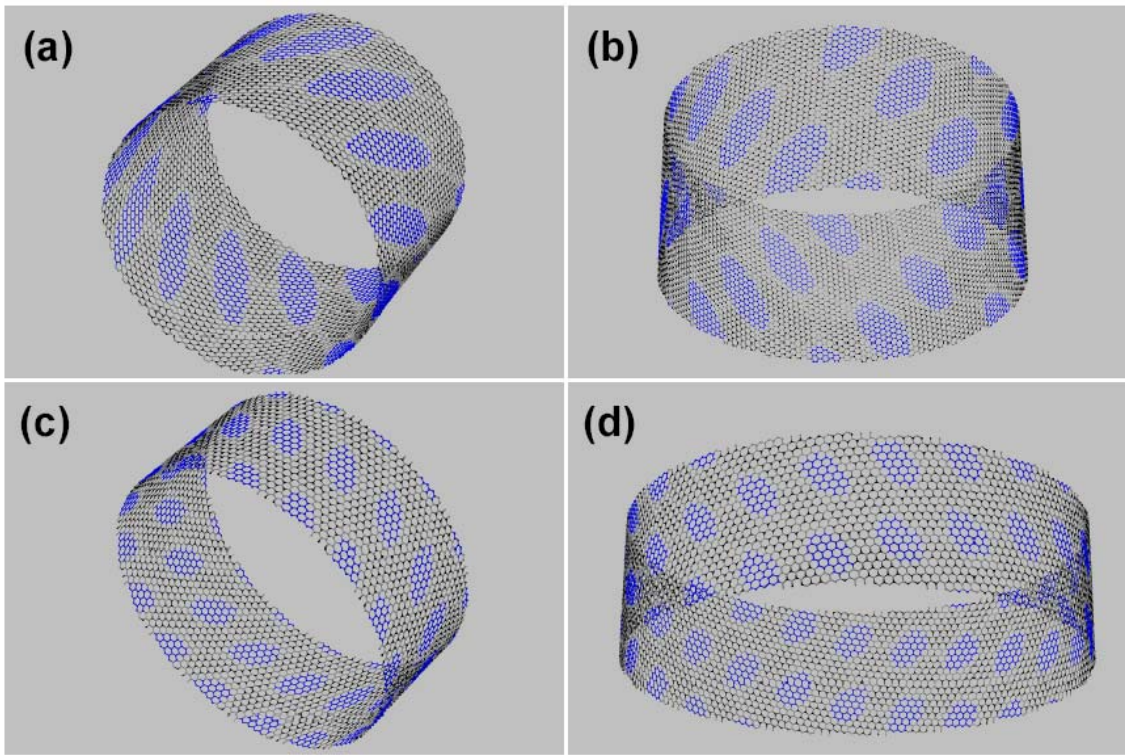


**Figure 5.5.** Relative alignment maps for DWCNTs with indices (a) (58,58)@(70,56) with  $D = 8.56$  nm and  $\Delta\chi = 3.67^\circ$ ; (b) (94,94)@(110,88) with  $D = 13.45$  nm and  $\Delta\chi = 3.67^\circ$ ; (c) (112,0)@(112,16) with  $D = 9.46$  nm and  $\Delta\chi = 6.59^\circ$ ; and (d) (165,0)@(161,23) with  $D = 13.59$  nm and  $\Delta\chi = 6.59^\circ$ . Only the outer nanotubes are shown for clarity and the coloring scheme is consistent with that of Figure 5.4. Comparing (a) with (b) and (c) with (d) shows that the sizes of the colored regions are independent of the DWCNT average diameter and depend only on the difference in the chiral angle,  $\Delta\chi$ , of the two nanotubes in each DWCNT.

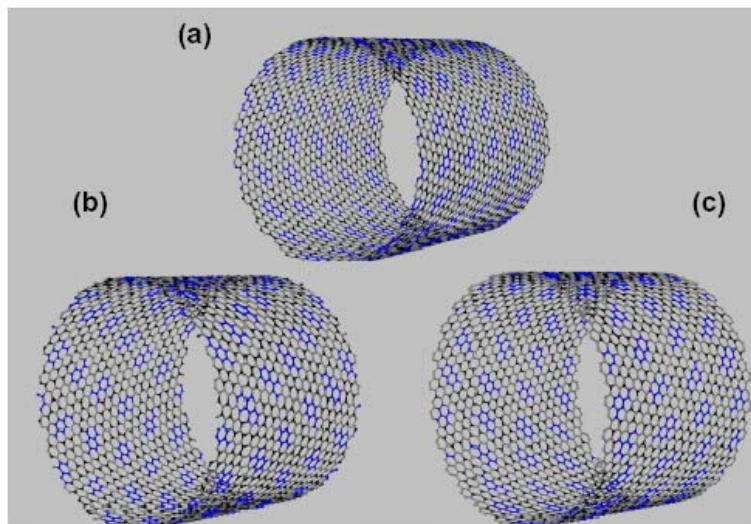


**Figure 5.6.** Relative alignment maps for DWCNTs with indices (a) (56,0)@(54,18) with  $D = 5.08$  nm and  $\Delta\chi = 13.9^\circ$ ; (b) (31,31)@(50,20) with  $D = 4.89$  nm and  $\Delta\chi = 13.9^\circ$ ; and (c) (54,6)@(50,25) with  $D = 5.18$  nm and  $\Delta\chi = 13.9^\circ$ . Only the outer nanotubes are shown for clarity and the coloring scheme is consistent with that of Figure 5.4. Comparing (a), (b), and (c) with each other shows that the sizes of the colored regions are independent of the chirality of the individual nanotubes and depend only on the difference in the chiral angle,  $\Delta\chi$ , of the two nanotubes in each DWCNT.

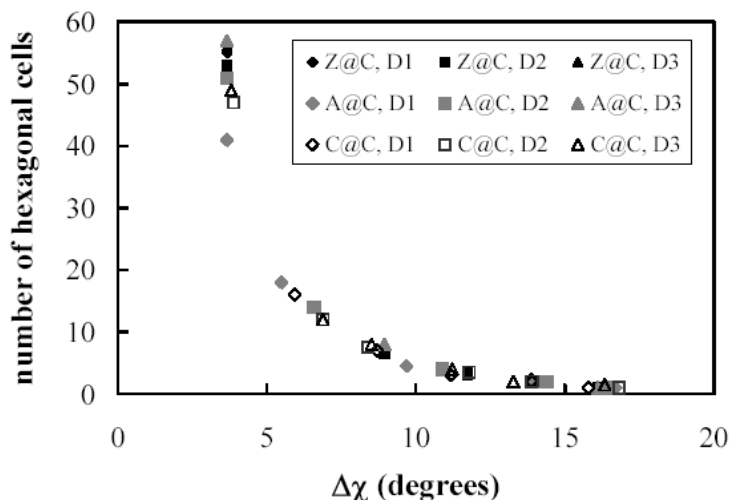


**Figure 5.7.** Maximum number of hexagonal cells in an individual patch of a relative alignment map in DWCNTs as a function of the difference in the chiral angles,  $\Delta\chi$ , between the individual nanotubes of the DWCNTs and for various DWCNT average diameters. Black, gray, and open symbols are used to represent combinations of zigzag (Z) and chiral (C) walls (Z@C), armchair (A) and chiral walls (A@C), and two chiral walls (C@C), respectively. Diamonds, squares, and triangles correspond to DWCNTs with average external diameters  $D_1 = 5.20$  nm,  $D_2 = 9.01$  nm, and  $D_3 = 13.64$  nm, respectively.

## 5.4 DFT Analysis of Inter-shell C-C Bonding in MWCNTs

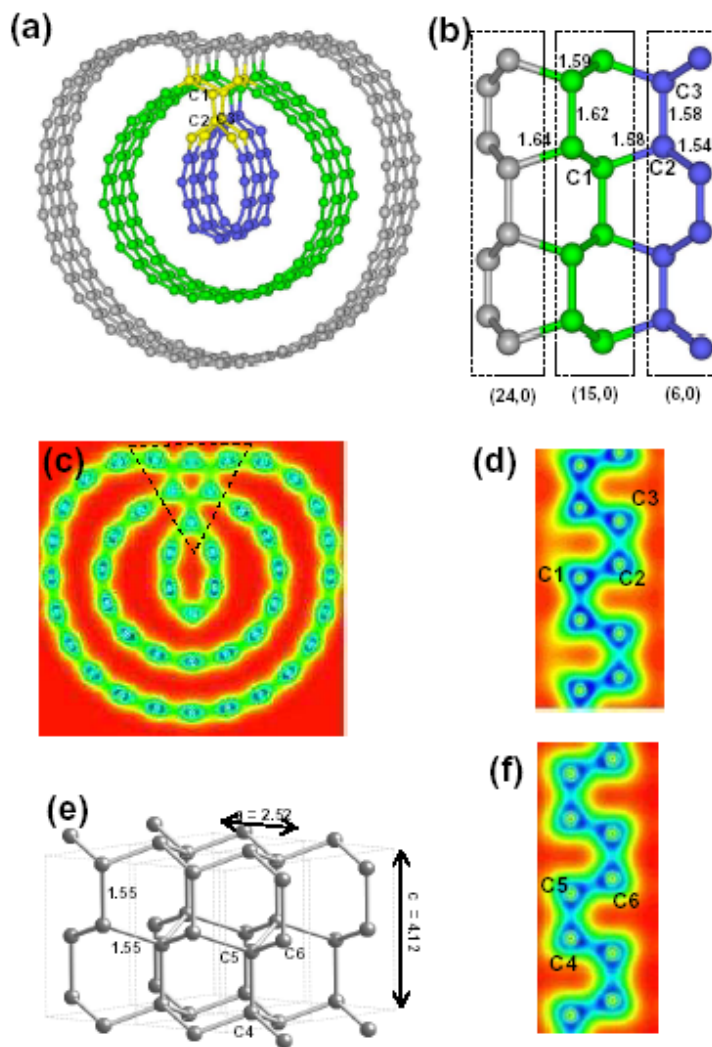
Our first-principles DFT analysis of inter-shell C-C bonding in pristine MWCNTs aims at providing insights and reaching quantitative conclusions regarding the formation of seed structures for the nucleation of nanocrystalline diamond phases. Here, we report representative results of our DFT analysis focusing on interactions between the concentric graphene walls of the triple-walled CNT (TWCNT) (6,0)@(15,0)@(24,0). In the structurally optimized configuration of this pristine TWCNT, the inter-wall distances between the (6,0) and (15,0) and the (15,0) and (24,0) nanotubes are equal to 3.4 Å. The results of the DFT analysis are shown in Figures 5.8 and 5.9. The analysis confirms that specific alignments of concentric graphene walls result in the formation of inter-shell C-C bonds in MWCNTs that constitute the seed units for the nucleation of specific crystalline C phases. These specific alignments are consistent with those described in Section 5.3.

Figure 5.8 shows results of inter-shell C-C bonding in the TWCNT that may lead to the nucleation of the hexagonal-diamond phase; the atoms constituting the seed unit for the hexagonal-diamond phase nucleation are colored yellow in Figure 5.8(a). In this case, the adjacent graphene walls of the (6,0) and (15,0) nanotubes are displaced with respect to each other in the axial direction by a distance equal to one half of the  $sp^2$  C-C bond length, i.e., an alignment consistent with that of Figure 5.1(c), and the graphene walls of the (6,0) and (24,0) nanotubes have overlapping hexagonal cells if projected onto the same plane normal to the radial direction, i.e., an alignment consistent with that of Figure 5.1(b). The resulting inter-shell C-C bonding in this specific alignment leads to a structural configuration that resembles stacking of planes in a manner equivalent to the ...ABAB... stacking in the hexagonal-diamond phase. Figures 5.8(a) and 5.8(b) depict

inter-shell C-C bonds between the (6,0) and (15,0) nanotubes and between the (15,0) and (24,0) nanotubes; the presence of subsequent outer nanotubes may lead to the formation of a larger nanocrystal, as discussed in our MD studies of Section 5.5. The configuration depicted in Figures 5.8(a) and 5.8(b) consists of 6-member rings of C atoms due to the local tetrahedral geometries. The inter-shell interactions and the resulting local  $sp^3$  bonding are highlighted by the valence electron density (VED) distributions of Figures 5.8(c) and 5.8(d); this bonding is characterized by an average bond length and bond angle of 1.56 Å and 109.31°, respectively. Evidence of strong inter-shell C-C bonding is provided by the shared electronic charge in the region enclosed by the dashed triangle in Figure 5.8(c). Figure 5.8(e) shows the crystalline lattice of the bulk hexagonal-diamond phase (lonsdaleite); the corresponding electronic structure is depicted in the VED distribution of Figure 5.8(f). The nearly identical local bonding environment shown in the VED distributions of Figures 5.8(d) and 5.8(f), corresponding to the inter-shell bonded TWCNT and the bulk hexagonal-diamond phase, confirms the possibility of formation of hexagonal diamond as a result of inter-shell interactions leading to inter-shell C-C bonding in MWCNTs.

In a similar manner, Figure 5.9 shows DFT results of inter-shell C-C bonding in the (6,0)@(15,0)@(24,0) TWCNT that may lead to the nucleation of the cubic-diamond phase. In this case, the adjacent graphene walls of the (6,0) and (15,0) nanotubes are displaced with respect to each other in the axial direction by a distance equal to one  $sp^2$  C-C bond length and the graphene walls of the (15,0) and (24,0) nanotubes are further displaced by a distance equal to one  $sp^2$  C-C bond length; as a result, the three carbon nanotubes have the relative alignment depicted in Figure 5.1(a). The inter-shell C-C

bonds between the adjacent graphene walls of the TWCNT are shown in Figure 5.9(a) and in the close view of Figure 5.9(b). The inter-shell C-C bonding in this specific alignment leads to a structural configuration that resembles stacking of planes in a manner equivalent to the ...ABCABC... stacking in the cubic-diamond phase. The VED distributions in Figures 5.9(c), 5.9(d), and 5.9(e) highlight the inter-shell interactions and the resulting local  $sp^3$  bonding between the adjacent graphene walls of the TWCNT. In order to characterize the resulting crystalline phase of carbon that may be nucleated from this cross-linking of CNTs, we examine the close view of a small region, Figure 5.9(b), from the original supercell shown in Figure 5.9(a). The local gray tetrahedral unit that is shown to have formed in Figure 5.9(b) has an average bond length and bond angle of 1.56 Å and 109.33°, respectively, while the tetrahedral unit shown in blue has an average bond length and bond angle of 1.55 Å and 109.42°, respectively. This local structural unit that has formed from inter-shell interactions in the (6,0)@(15,0)@(24,0) TWCNT provides the seed unit for the nucleation of the cubic-diamond phase. The crystalline lattice of the bulk cubic-diamond phase is shown in Figure 5.9(f). The similarities in the bonding environment of the seed unit of Figures 5.9(a) and 5.9(b) with that of the bulk cubic-diamond phase, Figure 5.9(f), are evident by comparing the VED distributions of Figures 5.9(e) and 5.9(g). The VED distribution of Figure 5.9(e) is in the plane of carbon atoms labeled C7, C8, and C9 in the TWCNT configuration of Figure 8(a), while the VED distribution of Figure 5.9(g) corresponds to the bulk cubic-diamond phase.



**Figure 5.8.** Structure resulting from inter-shell C-C bonding in a MWCNT according to first-principles DFT calculations. (a-d) Optimized atomic configuration of MWCNT with indices  $(6,0)@(15,0)@(24,0)$ , i.e., with  $(6,0)$ ,  $(15,0)$ , and  $(24,0)$  concentric inner (colored in blue), middle (colored in green), and outer (colored in gray) nanotubes, respectively, depicting inter-shell C-C bonding. (a) Top view along the axial direction. (b) Cross-sectional view on the symmetry plane. Blue, green, gray, and yellow spheres denote C atoms. The yellow colored C atoms highlight the seed unit for the nucleation of a bulk phase of hexagonal diamond. (c) Valence electron density (VED) distribution on a plane perpendicular to the axial direction of the MWCNT. (d) VED distribution on a plane parallel to the axial direction of the MWCNT, containing the atoms labeled C1, C2, and C3 in (a) and (b). The VED distributions in (c) and (d) highlight the inter-tube interactions and reveal the inter-shell C-C bonding and the accompanying shell distortions and structural relaxations [e.g., region enclosed by the triangle in (c)]. (e) Lonsdaleite lattice. (f) VED distribution for the lonsdaleite phase on the plane of C atoms labeled C4, C5, and C6 in (e). In (b) and (e), the numbers shown indicate interatomic distances or lattice parameters in Å. In (c), (d), and (f), the VED increases as the color changes from red (zero VED) to blue.

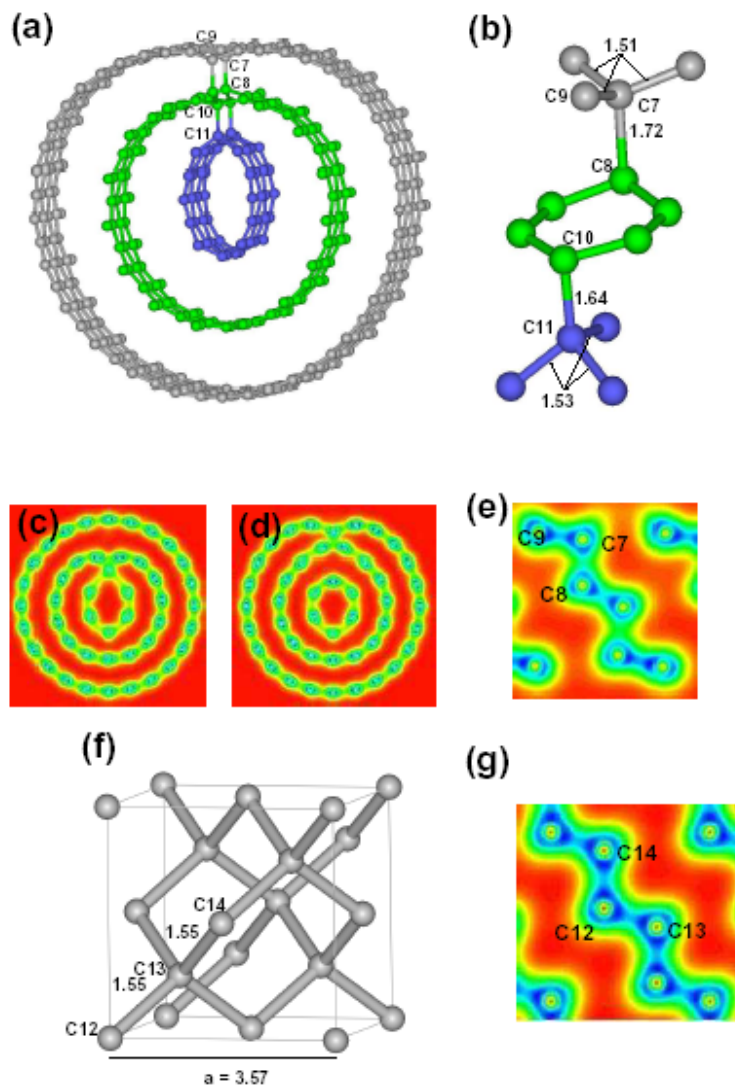


**Figure 5.9.** Structure resulting from inter-shell C-C bonding in a MWCNT according to first-principles DFT calculations. (a-e) Optimized atomic configuration of a (6,0)@(15,0)@(24,0) MWCNT with (6,0), (15,0), and (24,0) concentric inner (colored in blue), middle (colored in green), and outer (colored in gray) nanotubes, respectively, depicting inter-shell C-C bonding. (a) Top view along the axial direction. (b) Only a small region from the original supercell in (a) is shown highlighting the seed unit for the nucleation of a cubic-diamond crystal. Blue, green, and gray spheres denote C atoms. (c) VED distribution on a plane perpendicular to the axial direction of the MWCNT. (d) VED distribution on another plane perpendicular to the axial direction of the MWCNT. (e) VED distribution on a plane containing the atoms labeled C7, C8, and C9 in (a) and (b). The VED distributions in (c), (d), and (e) highlight the inter-tube interactions and reveal the inter-shell C-C bonding and the accompanying shell distortions and structural relaxations. (e) Cubic-diamond lattice. (f) VED distribution for the cubic-diamond phase on the plane of C atoms labeled C12, C13, and C14 in (f). In (b) and (f), the numbers shown indicate interatomic distances or lattice parameters in Å. In (c), (d), (e), and (g), the VED increases as the color changes from red (zero VED) to blue.

## **5.5 MD-generated Structurally Relaxed Inter-shell Bonded Nanocrystalline Structures Embedded in MWCNTs**

Our DFT analysis of Section 5.4 examined the possibility of nucleation of crystalline diamond phases through inter-shell C-C bonding in a representative MWCNT configuration. Here, we explore further the nucleation and growth of such crystalline C phases over the broadest range of CNT geometrical parameters building on the geometrical findings of Section 5.3. Given our testing and validation of the AIREBO potential for this study in Section 5.2 and Appendix A, we generated structurally relaxed inter-shell bonded nanocrystalline structures based on MD computations with interatomic interactions described by the AIREBO potential. This AIREBO-MD-based structural relaxation procedure allowed for the computationally efficient exploration of the parameter space, including MWCNT configurations of sizes much larger than those that can be handled easily by first-principles DFT analysis.

Representative results of a systematic and comprehensive structural relaxation study of inter-shell bonded nanocrystalline structures embedded in DWCNTs are shown in Figures 5.10-5.12. This study spanned a broad range of the parameter space discussed in Section III.A. In each of the cases shown in Figures 5.10-5.12, two regions of the DWCNT are chosen characterized by relative (inter-shell) alignments of type I and type II, respectively. To aid in the visualization of the resulting inter-shell bonded relaxed structures, we have used a local frame of reference appropriate for the structural analysis of each region and generated different planar views using the corresponding local coordinate system. In all cases in Figures 5.10-5.12, consistent with the findings of Section 5.3, the relaxed inter-shell bonded structures in DWCNT regions of type-I and

type-II alignment are nanocrystalline regions that can be viewed as seeds for the nucleation of the cubic-diamond and hexagonal-diamond phase, respectively.

The cases depicted in Figures 5.10-5.12 correspond to DWCNTs of similar average diameter but different combinations of graphene wall configurations and different values of  $\Delta\chi$ . In Figures 5.10, 5.11 and 5.12, the graphene wall combinations are armchair@chiral, chiral@chiral, and zigzag@chiral, respectively; the specific DWCNT indices in Figures 5.10, 5.11, and 5.12 are (63,63)@(81,54), (99,9)@(90,36), and (110,0)@(95,38), respectively, and the corresponding  $\Delta\chi$  values are  $6.6^\circ$ ,  $11.8^\circ$ , and  $16.1^\circ$ . By comparing the configurations of Figures 5.10, 5.11, and 5.12, it is evident that their main difference is in the size of the nanocrystals generated due to the inter-shell C-C bonding. Consistent with the results of Figures 5.4-5.7, the resulting nanocrystal size decreases as the chiral-angle difference  $\Delta\chi$  increases. Moreover, close inspection of the borders of these nanocrystalline regions shows the increased misalignment between the two graphene walls compared to their alignment inside the nanocrystalline regions; this confirms further the finite sizes expected of these seed units formed due to inter-shell C-C bonding between adjacent graphene walls of random chiral-angle combinations in MWCNTs.

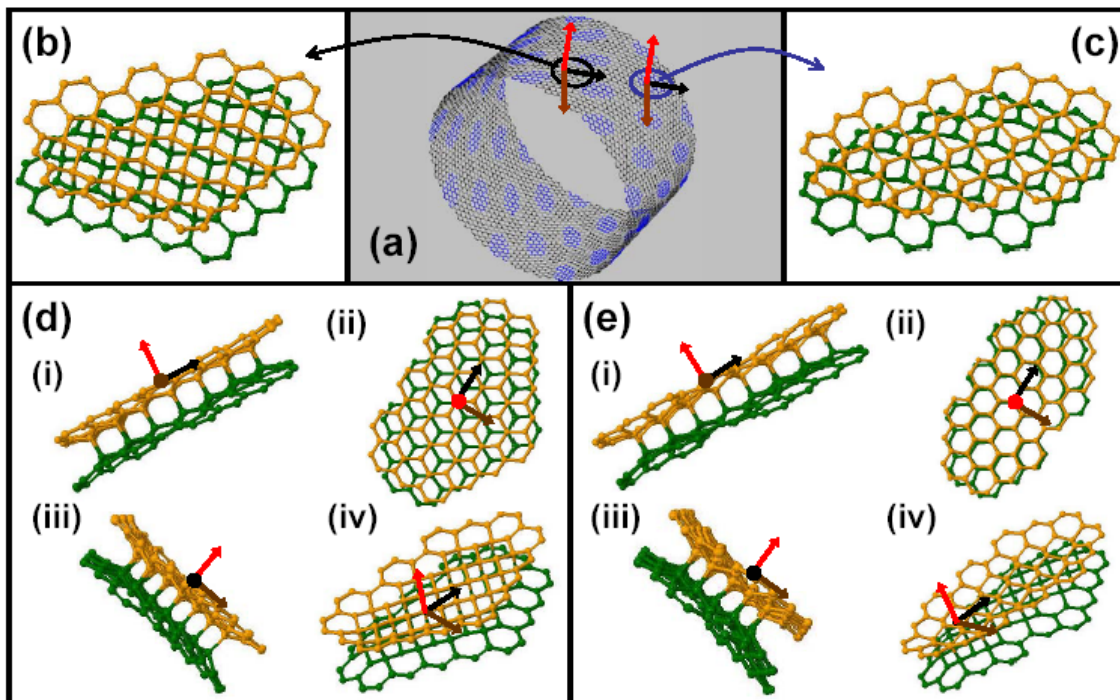


**Figure 5.10.** Representative MD-relaxed local structures formed by the creation of inter-shell C-C bonds in a DWCNT with indices  $(63,63)@(81,54)$  and  $\Delta\chi = 6.6^\circ$ . (a) Regions of the DWCNT where these relaxed structures are created, marked with black and blue circles, and local coordinate vectors used for structural analysis and visualization. Only the outer nanotube of the DWCNT is shown for clarity and the coloring scheme is consistent with that of Figure 5.4. (b, c) Local structures that can act as seeds for the nucleation of (b) the cubic-diamond phase and (c) the hexagonal-diamond phase, extracted from the DWCNT. (d, e) Different planar views, (i), (ii), (iii), and (iv), of the structures given in (b) and (c), respectively, using the local coordinates defined in (a). In (b)-(e), orange and green spheres are used to represent carbon atoms belonging to the outer and inner nanotube of the DWCNT, respectively.

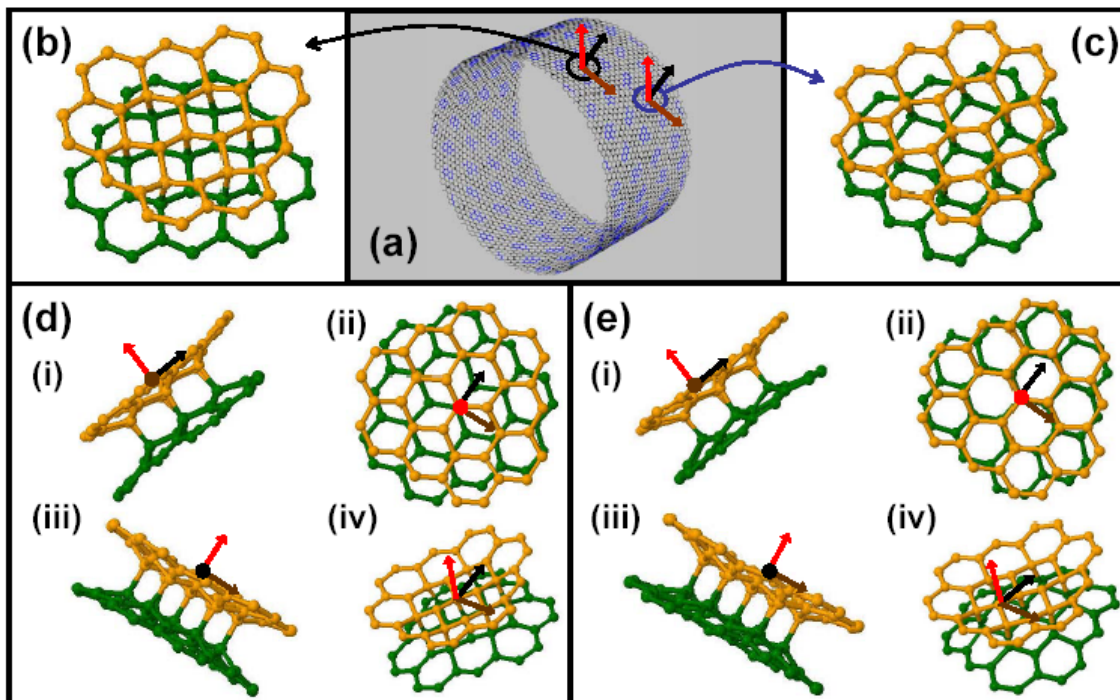


**Figure 5.11.** Representative MD-relaxed local structures formed by the creation of inter-shell C-C bonds in a DWCNT with indices  $(99,9)@(90,36)$  and  $\Delta\chi = 11.8^\circ$ . (a) Regions of the DWCNT where these relaxed structures are created, marked with black and blue circles, and local coordinate vectors used for structural analysis and visualization. Only the outer nanotube of the DWCNT is shown for clarity and the coloring scheme is consistent with that of Figure 5.4. (b, c) Local structures that can act as seeds for the nucleation of (b) the cubic-diamond phase and (c) the hexagonal-diamond phase, extracted from the DWCNT. (d, e) Different planar views, (i), (ii), (iii), and (iv), of the structures given in (b) and (c), respectively, using the local coordinates defined in (a). In (b)-(e), orange and green spheres are used to represent carbon atoms belonging to the outer and inner nanotube of the DWCNT, respectively.

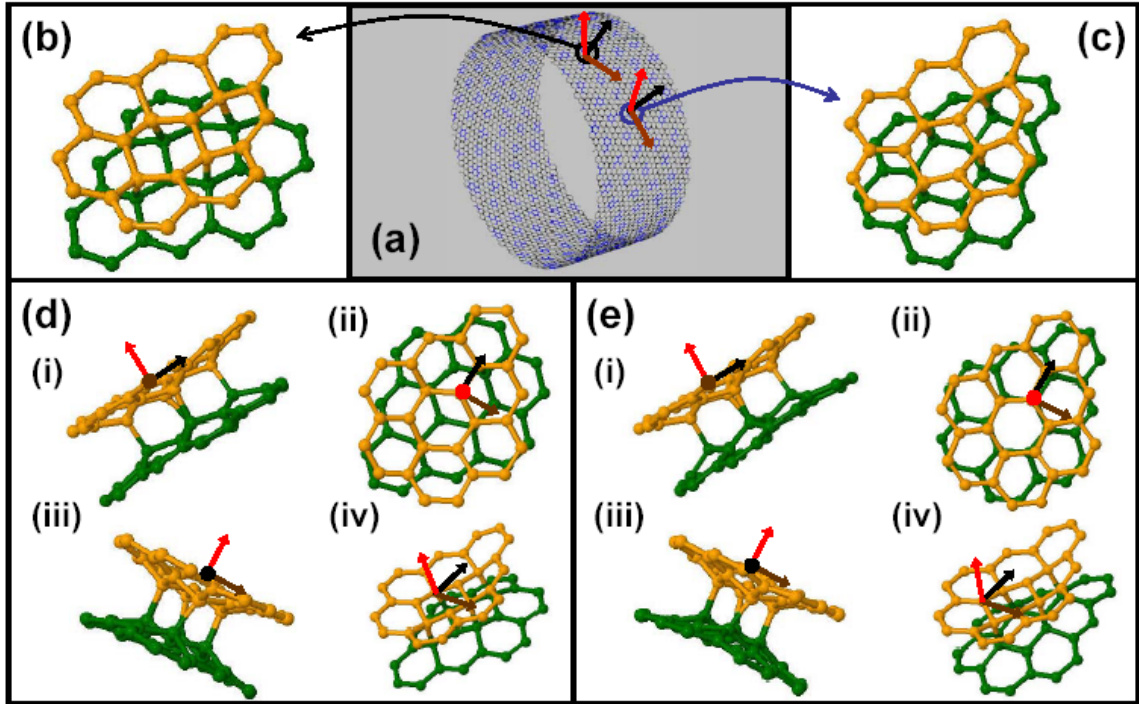


**Figure 5.12.** Representative MD-relaxed local structures formed by the creation of inter-shell C-C bonds in a DWCNT with indices  $(110,0)@(95,38)$  and  $\Delta\chi = 16.1^\circ$ . (a) Regions of the DWCNT where these relaxed structures are created, marked with black and blue circles, and local coordinate vectors used for structural analysis and visualization. Only the outer nanotube of the DWCNT is shown for clarity and the coloring scheme is consistent with that of Figure 5.4. (b, c) Local structures that can act as seeds for the nucleation of (b) the cubic-diamond phase and (c) the hexagonal-diamond phase, extracted from the DWCNT. (d, e) Different planar views, (i), (ii), (iii), and (iv), of the structures given in (b) and (c), respectively, using the local coordinates defined in (a). In (b)-(e), orange and green spheres are used to represent carbon atoms belonging to the outer and inner nanotube of the DWCNT, respectively.

In all the structurally relaxed inter-shell bonded nanostructures that we generated, we computed the energy difference,  $\Delta E$ , between the original MWCNT and the resulting fully relaxed inter-shell bonded structures; the original MWCNT structure always corresponds to the lowest-energy state. In all cases, the results of this energetic analysis and their implications for thermodynamic stability are very similar; they are based on the quantity  $\Delta E_B \equiv \Delta E/N_{\text{bonds}}$ , where  $N_{\text{bonds}}$  is the number of inter-shell C-C bonds formed.

This computation was carried out for both types of relative alignment resulting in cubic-diamond and hexagonal-diamond nanocrystals. The most important outcome of this computation is that the nanostructures with embedded cubic-diamond nanocrystals are always lower in energy, and therefore thermodynamically more stable, than those with embedded hexagonal-diamond nanocrystals. This is consistent with the difference between the cohesive energies of the corresponding bulk crystalline structures, as shown in Appendix A. Furthermore, for each MWCNT examined, the difference in  $\Delta E_B$  between the two types of nanostructures (with embedded cubic-diamond vs. hexagonal-diamond nanocrystals) is practically independent of the number of inter-shell C-C bonds; e.g., for the (50,50)@(55,55) DWCNT discussed in Section 5.3,  $\Delta E_B = 0.32$  eV (according to AIREBO-MD relaxation) independent of  $N_{\text{bonds}}$ .

Finally, Figure 5.13 shows relaxed structures of nanocrystals embedded in a MWCNT with more graphene walls, namely a TWCNT, to simply illustrate the growth in size of these nanocrystalline phases with the availability of multiple graphene walls for further inter-shell C-C bonding. For simplicity, an armchair@armchair@armchair nanotube is chosen, (50,50)@(55,55)@(60,60), and nanocrystals are generated by inter-shell C-C bonding in regions of type-I and type-II alignment depicted in Figures 5.13(a) and 5.13(b), respectively, leading to a cubic-diamond and a hexagonal-diamond nanocrystal, respectively. Structural analysis, aided by the different close planar views of the nanocrystalline regions shown in Figure 5.13, highlights the symmetries of the cubic-diamond and hexagonal-diamond phases in the central regions of the nanocrystals and how these symmetries are broken at the corresponding boundary regions.

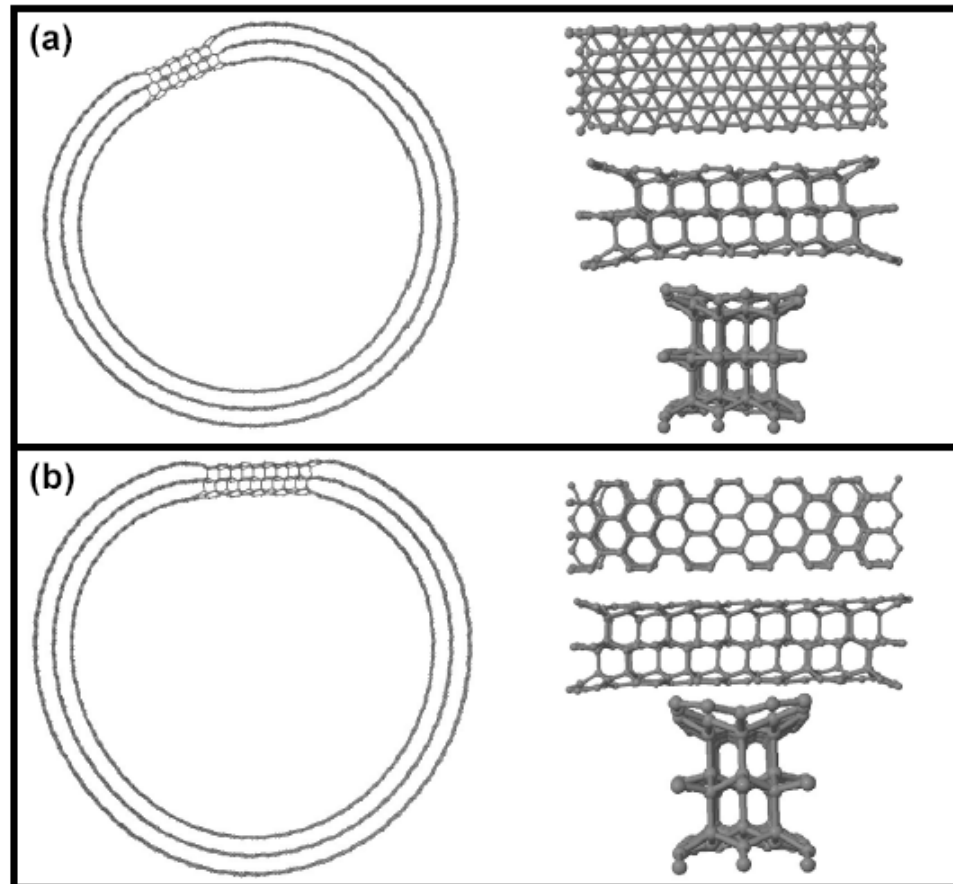


**Figure 5.13.** Crystalline structures embedded locally in a  $(50,50)@(55,55)@(60,60)$  MWCNT due to inter-shell C-C bonding that provide seeds for the nucleation of (a) cubic diamond and (b) hexagonal diamond. In both (a) and (b), a top view of the MWCNT with the embedded nanocrystal is shown on the left and three different close planar views of the nanocrystalline regions are shown on the right, corresponding from top to bottom to the planes  $(\theta, z)$ ,  $(r, \theta)$ , and  $(r, z)$  in a cylindrical-coordinate system.

## 5.6 Summary and Conclusions

In summary, we presented a systematic analysis of the nanocrystalline structures that can be generated as a result of the inter-shell C-C bonding between adjacent concentric graphene walls of MWCNTs. Our analysis was based on a combination of important geometrical, chemical, and structural elements of MWCNTs. This included a comprehensive exploration of the corresponding geometrical parameter space as

determined by the indices of the individual nanotubes that comprise the MWCNT, first-principles density functional theory calculations of inter-shell C-C bonding between adjacent graphene walls in MWCNTs, and molecular-dynamics-based structural relaxation of the resulting inter-shell bonded nanocrystalline structures employing a well validated interatomic potential. These structures can be viewed as nuclei for the growth of cubic-diamond and hexagonal-diamond nanocrystals embedded in the MWCNTs. We derived systematic rules for the determination of the lattice structure of the resulting nanocrystals according to the chirality and the relative alignment of adjacent graphene walls in the MWCNT. We demonstrated the formation of these crystalline phases over a broad range of nanotube diameters and for any possible combination of zigzag, armchair, or chiral configurations of graphene walls. Finally, we found that the size of the generated nanocrystals due to such inter-shell bonding depends strongly on the chiral-angle difference between adjacent graphene walls in the MWCNT.

Although the emphasis of this study is not on the origin of the inter-shell C-C bonding in MWCNTs, we believe that this may be possible due to a number of experimental circumstances including the interaction of H atoms with the MWCNT graphene walls or increased pressure and temperature in shock tubes. Future studies are going to be carried out, aiming at generating pathways of H-induced inter-shell C-C bond formation based on first-principles DFT calculations in conjunction with the climbing-image nudged elastic band (NEB) method (Henkelman et al., 2000). Here, we only mention that in the absence of H atoms, our DFT calculations revealed that the formation of the seed structure for nucleation of the lonsdaleite phase on a (6,0)@(15,0) DWCNT, i.e., the two inner tubes of the TWCNT of Figure 5.8(a), required overcoming an

activation energy barrier over 3.8 eV; this value corresponds to the energy difference between the original DWCNT and that containing inter-shell C-C bonds as shown in Figure 5.8(a), which is the higher-energy state. This implies that in the absence of H atoms, nucleation of the lonsdaleite phase is kinetically prohibited over the temperature range reported in experiments (Sun et al., 2004a, b; Yang et al., 2007). The calculated activation barriers are generally high for nucleation of either cubic or hexagonal diamond over the range of MWCNT chiralities and adjacent graphene wall alignments that we examined. In brief, our first-principles calculations indicate that the formation of crystalline seeds for the nucleation of the lonsdaleite and cubic-diamond crystalline phases is induced by H-MWCNT interactions, consistent with experiments which reported that MWCNT transformations are observed exclusively due to their exposure to a hydrogen plasma (Sun et al., 2004a, b; Yang et al., 2007) .

## CHAPTER 6

### INTERLAYER COVALENT BONDING IN TWISTED BILAYER GRAPHENE: ATOMIC AND ELECTRONIC STRUCTURE

#### 6.1 Introduction

Graphene, a two-dimensional material consisting of one-atom-thick sheets of  $sp^2$ -hybridized carbon atoms arranged in a honeycomb lattice, possesses an outstanding and unique set of electronic and mechanical properties, which has potential to enable a broad range of applications (Geim, 2009). Chemical modification of graphene, such as hydrogenation (Elias et al., 2009; Balog et al., 2010) and fluorination (Nair et al., 2009; Cheng et al., 2010) that gives rise to graphane and fluorographene, respectively, has been used to tailor graphene properties aiming at specific applications. Exposure of graphitic single- and multi-layered carbon nanomaterials to atomic hydrogen leads to formation of  $sp^3$ -hybridized C-H and C-C bonds, which alter their structure remarkably (Nikitin et al., 2008; Elias et al., 2009; Balog et al., 2010; Muniz and Maroudas, 2010); this process has been considered for hydrogen storage purposes, band gap control, and synthesis of other carbon phases (Sun et al., 2004a, b; Yang et al., 2007). For example, transformation of multi-walled carbon nanotubes (MWCNTs) to nanocrystalline diamond has been observed upon hydrogen plasma exposure (Sun et al., 2004a, b; Yang et al., 2007); it was suggested in Chapter 5 that the initial stage of the process (nucleation) is related to the creation of inter-shell bonds, i.e., covalent  $sp^3$  C-C bonds between atoms from adjacent shells (Muniz et al., 2009c). Moreover, density functional theory (DFT) calculations (Leenaerts et al., 2009; Chernozatonskii et al., 2009) have suggested that two-sided

hydrogenation of bilayer graphene may lead to formation of interlayer bonds, which stabilizes the structure. The graphite-to-diamond transition induced by high pressure/temperature or shock compression is the best-known case where such interlayer bonds are created (Scandolo et al., 1995; Ribeiro et al., 2005); under these extreme conditions, planes slide and/or buckle to generate the bonds between atoms from adjacent graphene planes. Interlayer covalent bonds also can be formed when defects are introduced, e.g., due to ion/electron irradiation of samples (Krasheninnikov and Banhart, 2007), in the structure of multi-layered carbon materials as a result of a healing mechanism (Telling et al., 2003).

The creation of interlayer bonds in multi-layered graphitic carbon materials leads to formation of new phases that are determined by the stacking of the pristine planes; these phases can transform to more thermodynamically stable ones (Scandolo et al., 1995; Ribeiro et al., 2005; Krasheninnikov and Banhart, 2007; Umemoto et al., 2010). For example, the two typical stackings observed between two adjacent planes in graphite and few-layer graphene (FLG), namely, *AB* (Bernal) and *AA* (hexagonal), form cubic and hexagonal diamond-like structures (Scandolo et al., 1995; Muniz et al., 2009c), as discussed in Chapter 5. For a pair of non-rotated graphene planes, in the absence of defects, the same stacking (either *AB* or *AA*) is found throughout the domain. When these planes are rotated with respect to each other, by angles ranging from  $0^\circ$  (perfect *AA* or *AB* stacking) to  $30^\circ$ , the resulting stacking is not unique. Early scanning tunneling microscopy (STM) studies of graphite surfaces have shown that the presence of such rotational faults forms moiré patterns on the surface (Kuwabara et al., 1990; Xhie et al., 1993; Rong and Kuiper, 1993); for a given rotation angle  $\theta$ , these patterns exhibit

different plane stackings in different regions of the surface. For small rotation angles, both  $AA$  and  $AB$  stacking sequences, as well as intermediate cases, are distributed throughout the structure within finite intercalated domains. The size of these finite domains decreases with an increase of the rotation angle  $\theta$  (Campanera et al., 2007; Muniz et al., 2009c; Shallcross et al., 2008b) and at the limit  $\theta \rightarrow \sim 15^\circ$  it practically vanishes:  $AA$  and  $AB$  plane stackings are no longer present and different configurations arise. In Chapter 5, we showed that inter-shell-bonded structures may be formed within pairs of adjacent walls of MWCNTs, with rotation angles up to this limit of  $\sim 15^\circ$ ; in this case, the rotation angle corresponds to the difference of chiral angles of the individual walls.

Recently, it was observed experimentally that epitaxial FLG samples grown on the C-face of SiC(000 $\bar{1}$ ) (Hass et al., 2007, 2008; Varchon et al., 2008) are formed by sequences of planes rotated with respect to each other over the range  $0 < \theta < 30^\circ$ . Calculations have suggested that bilayers become more stable when  $\theta \rightarrow 30^\circ$  (Campanera et al., 2007; Shallcross et al., 2008b); the most stable bilayer among the ones investigated by Shallcross and coworkers (Shallcross et al., 2008b) is the commensurate one corresponding to  $\theta = 30 \pm 2.204^\circ$ . The moiré pattern generated by this bilayer has been observed in STM images of FLG samples (Hass et al., 2008). The presence of such rotational faults makes epitaxial FLG retain some of the outstanding electronic properties of single-layer graphene due to electronic decoupling of the layers (Hass et al., 2008; Latil et al., 2007; Lopes dos Santos et al., 2007; Shallcross et al., 2008a; Sprinkle et al., 2009); these properties usually vanish when bilayers are stacked in  $AA$  and  $AB$  plane sequences (Latil and Henrard, 2006; Aoki and Amawashi, 2007).

The central question of this study is: considering that interlayer bonds are formed between atoms in two or more rotated planes for  $\theta > \sim 15^\circ$  in a multilayered material, is it possible to generate any specific local ordered structure, or just a random amorphous phase? In this chapter, using a combination of first-principles DFT calculations and classical molecular-dynamics (MD) simulations, we derive a set of novel carbon nanostructures from rotationally misoriented graphene bilayers (twisted bilayer graphene), upon creation of interlayer covalent C-C bonds. These structures consist of caged fullerene-like configurations embedded within the graphene bilayer and are generated from pairs of layers rotated by angles  $\theta \sim 30^\circ$ ; in this limit, a zigzag- and an armchair-oriented pair of planes are aligned. We calculate the electronic structures of these materials. For certain such structures, we show that, in spite of the introduction of  $sp^3$  bonds due to hydrogenation and interlayer bonding, the linear dispersion around the  $K$ -point in the Brillouin zone (Dirac cones), characteristic of graphene and twisted bilayer graphene, is preserved. We also demonstrate that an entire class of similar caged structures of different sizes can be generated in an analogous manner.

## **6.2 Computational Methods**

### **6.2.1 Density Functional Theory Calculations**

For determination of the electronic structure and structural relaxation of the proposed nanomaterials, we employed first-principles DFT calculations using the QUANTUM ESPRESSO software package (Giannozzi et al., 2009). These calculations were carried out within the local density approximation (LDA), using the exchange-correlation functional as parameterized by Perdew and Zunger (Perdew and Zunger,

1981), and employing plane-wave basis sets and ultrasoft pseudopotentials available from the QUANTUM ESPRESSO database, which were tested properly for accuracy. The Monkhorst-Pack sampling scheme (Monkhorst and Pack, 1976) was used to generate uniform  $\mathbf{k}$ -point grids for integrations in the Brillouin zone (BZ). In the calculations for graphitic structures, Marzari-Vanderbilt cold smearing (Marzari et al., 1999) was applied with a smearing factor of 0.020 Ry. In the implementation of the supercell approximation, convergence regarding the amount of vacuum used in the direction perpendicular to the planes (distance between images of at least 10 Å) was tested in order to avoid spurious interactions between images.

In this study, we chose LDA for the exchange-correlation functional because of its ability to predict the interlayer spacing  $c$  in graphite/graphene bilayers with very good accuracy; LDA is shown to perform better than GGA for the prediction of  $c$ , but it underpredicts slightly the in-plane lattice parameter  $a$  (see discussion below and Table 6.1). In addition, LDA describes correctly the electronic structure of graphene (single and multi-layered) in the vicinity of the Fermi level (Latil and Henrard, 2006; Aoki and Amawashi, 2007; Latil et al., 2007; Hass et al., 2008; Shallcross et al., 2008a,b).

Before addressing the problems of interest, some preliminary calculations were carried out in order to assess the accuracy of the methodology for predicting the structure and properties of the carbon nanostructures. The equilibrium lattice parameters and bulk moduli for cubic diamond, graphite, and graphene bilayers (with  $AA$  and  $AB$  stacking) were estimated and the results are summarized in Table 6.1. A convergence test was carried out in order to obtain solutions independent of the energy cutoff and number of  $\mathbf{k}$ -points; the results presented for cubic diamond correspond to kinetic energy cutoffs of 40

Ry for plane waves and 360 Ry for charge density, and a  $8 \times 8 \times 8$  Monkhorst-Pack mesh of  $\mathbf{k}$ -points, while for graphene (single and bilayer) and graphite energy cutoffs of 60 Ry for plane waves and 540 Ry for charge density were used with  $\mathbf{k}$ -point meshes of  $8 \times 8 \times 1$  for single/bilayers graphene ( $2 \times 2$  supercells) and  $8 \times 8 \times 4$  for graphite ( $2 \times 2$  supercells). The bulk modulus for diamond and graphite was calculated by fitting energy versus volume data, using the Murnaghan equation of state (Murnaghan, 1944). The values found (Table 6.1) are in good agreement with results reported in the literature for calculations with the same exchange-correlation functional and similar pseudopotentials, as well as with experimental results (Yin, 1984; Yin and Cohen, 1984; Fahy et al., 1986; Fahy and Louie, 1987; Jansen and Freeman, 1987; Furthmüller et al., 1994; Janotti et al., 2001; Kim and Chen, 2004; Aoki and Amawashi, 2007; Campanera et al., 2007; Shallcross et al., 2008b; Leenaerts et al., 2009).

**Table 6.1.** Lattice parameters and bulk moduli  $B_0$  for different carbon phases, calculated by DFT/LDA and compared to values previously reported in the literature. The  $B_0$  values computed for graphite correspond to uniform compression, except for the ones marked with “\*”, which correspond to uniaxial compression along the direction perpendicular to the planes. Numbering of the corresponding references follows the sequence: [1] Yin, 1984; Yin and Cohen, 1984; [2] Fahy et al., 1986; Fahy and Louie, 1987; [3] Jansen and Freeman, 1987; [4] Furthmüller et al., 1994; [5] Janotti et al., 2001; [6] Kim and Chen, 2004; [7] Aoki and Amawashi, 2007; [8] Campanera et al., 2007; [9] Shallcross et al., 2008b.

	This Work				Literature
	$a$ (Å)	$c/a$	$c/2$ (Å)	$B_0$ (GPa)	$a$ (Å), $c/a$ // $B_0$ (GPa)
diamond	3.527	-	-	463	3.548//444[2], 3.528//460[4], 3.535//465[5], 3.567//443 (exp)[6]
graphite (AB)	2.439	2.731	3.33	288 / 29.6*	2.47, 2.724//236.1[1], 2.459, 2.776//319[3], 2.440, 2.738 // 286[4], 2.447, 2.706//26.8*[5], 33.8-41 (exp)[6]
graphite (AA)	2.439	2.952	3.60	-	-
	$a$ (Å)	$c/a$	$c/2$ (Å)	$B_0$ (GPa)	$c/2$ (Å)
bilayer (AB)	2.439	-	3.31	-	3.33 [7], 3.32 [8], ~3.32 [9]
bilayer (AA)	2.439	-	3.58	-	3.62 [7], 3.59 [8], ~3.61 [9]

## 6.2.2 AIREBO-based Molecular-Dynamics Simulations

For larger structures, geometrical optimization with DFT becomes computationally expensive; in such cases, isobaric-isothermal (NPT) classical molecular-dynamics simulations were employed according to the Adaptive Interatomic Reactive Empirical Bond-Order (AIREBO) potential for description of the C-C and C-H interactions (Stuart et al., 2000), introduced in Chapter 2. Such classical simulations were also used to obtain initial configurations for the DFT-based structural optimization, as discussed in section 6.2.3. The AIREBO potential has been used widely for modeling solid carbon phases and hydrocarbon molecules and it has been successful in predicting inter-shell C-C bonding in multi-walled carbon nanotubes and structures of hydrogenated SWCNTs and graphene, as demonstrated in Chapters 3, 4 and 5 of the thesis.

These classical structural relaxations were carried out by isothermal-isobaric (NpT) molecular-dynamics (MD) simulations at low temperature and hydrostatic pressure; temperature and pressure were controlled by employing the Berendsen thermostat/barostat (Berendsen et al., 1984). A variant of the simulated annealing method was employed in order to minimize the possibility of the system getting trapped into local energy minima during the relaxation process. This procedure consists of equilibrating the structures through a sequence of (NpT) MD simulations at each temperature stage of a cooling schedule with a final temperature  $T = 0.1$  K.

## 6.2.3 Structural Relaxation of Interlayer Bonded Configurations

We report in this chapter, results for optimized structures of pristine and hydrogenated twisted bilayers in the absence and presence of interlayer bonding. To

obtain the initial configurations for the DFT-based geometrical optimization of the interlayer-bonded structures, we displaced the desired atoms to be bonded in the pristine bilayer and then relaxed the resulting deformed structure using classical molecular-dynamics (MD) simulations, as described in Section 6.2.2; AIREBO-MD was chosen for this initial step for its computational efficiency compared to the first-principles calculations. The AIREBO-MD-generated structures are taken as the initial guesses for the DFT-based full relaxation, where both atomic and volume relaxation is carried out, until convergence in energy, atomic forces, and stresses is achieved.

For reasons of computational efficiency, only the  $\Gamma$  point was used for sampling the Brillouin zone in the electronic structure calculation during the structural optimizations, due to the large size of the supercells employed (194-218 atoms for the case where  $\theta = 30^\circ$ , and 208-232 atoms for  $\theta = 30 \pm 2.204^\circ$ ). Moreover, using only the  $\Gamma$  point makes the calculations more computationally efficient, taking advantage of the real character of the Kohn-Sham orbitals in this case (Giannozzi et al., 2009).

In the iterative procedure for structural relaxation, the cutoff energy for plane waves used was 30 Ry; in preliminary test cases, relaxation with values up to 60 Ry led to practically identical structures. For reporting the binding energies of the geometrically optimal configurations (Table 6.2, presented later in this chapter), a cutoff energy of 60 Ry was employed; this value provides well-converged relative energy differences, as illustrated in Figure 6.1. The cutoff energy for charge density calculations was taken to be 9 times higher than that used for plane waves, for maintaining consistency; convergence studies with respect to this parameter confirmed that this value was sufficiently large.

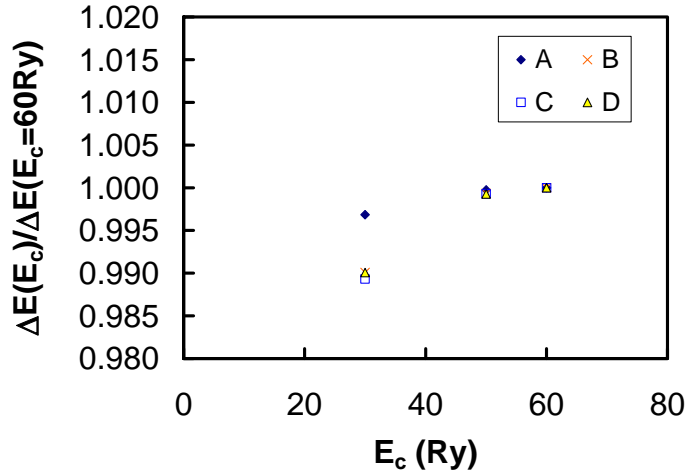


**Figure 6.1.** Computed binding energies,  $\Delta E$ , as a function of cutoff energy for plane waves,  $E_c$ , for interlayer-bonded structures with  $\theta = 30^\circ$  and hydrogenation patterns A, B, C, and D (defined in Section 6.3). Results are presented in terms of the ratio of the energy for a given cutoff over the energy computed at  $E_c = 60$  Ry.

#### 6.2.4 Band Structure Calculations

Electronic band structures were calculated for pristine single-layer graphene and with *AA*- an *AB*-stacked graphene bilayers, as benchmark cases in order to assess the accuracy of our DFT/LDA calculations. DFT calculations within the LDA approximation have been shown to predict accurately the band structure for these nanomaterials around the Fermi level (Latil and Henrard, 2006; Aoki and Amawashi, 2007; Latil et al., 2007; Hass et al., 2008; Shallcross et al., 2008a,b). The results obtained in our calculations are summarized in Figure 6.2. The inset in Figure 6.2(a) illustrates the Brillouin zone (BZ) and the path used in the calculation ( $\Gamma$ -M-K- $\Gamma$ ). For single-layer graphene, calculations were carried out for a  $1 \times 1$  and a  $2 \times 2$  supercell (2 and 8 atoms, respectively); for the bilayers,  $2 \times 2$  supercells containing 16 atoms were used. All of these results are in agreement with previous calculations reported in the literature (Latil

and Henrard, 2006; Aoki and Amawashi, 2007; Latil et al., 2007; Hass et al., 2008; Shallcross et al., 2008a,b; Mele, 2010; Xu et al., 2010).

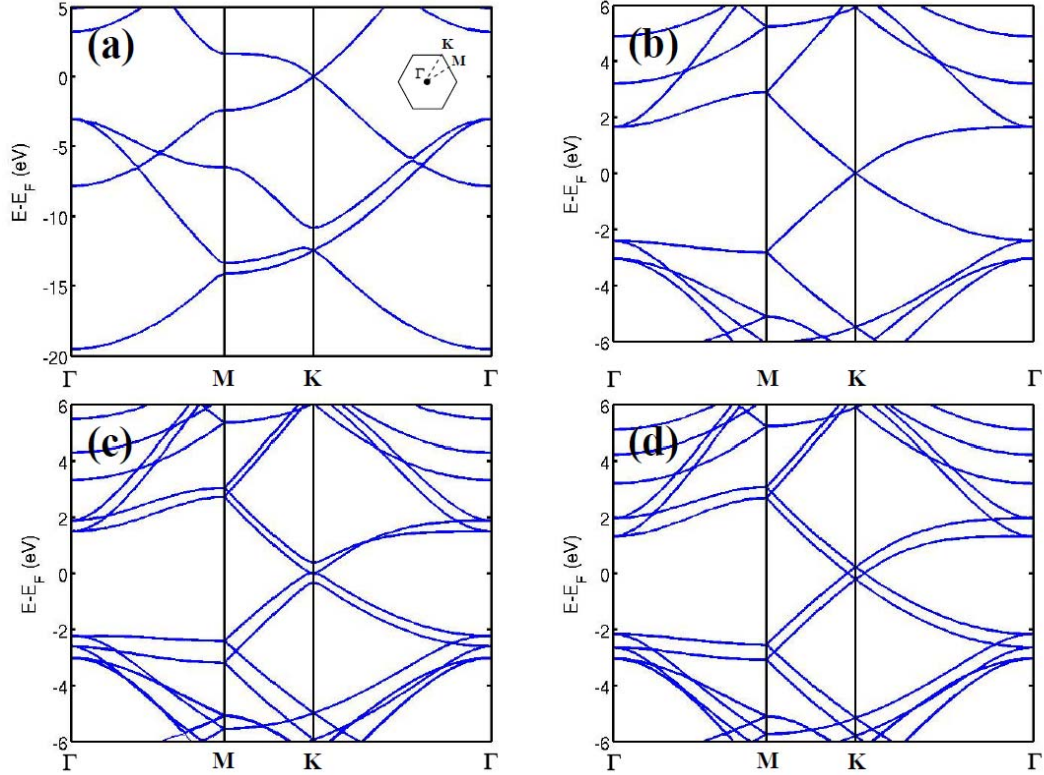


**Figure 6.2.** Band structures for single-layer graphene computed using (a)  $1\times 1$  and (b)  $2\times 2$  supercells and bilayer graphene using a  $2\times 2$  supercell for (c)  $AB$  and (d)  $AA$  stacking.

For the computation of the electronic band structures for pristine and hydrogenated interlayer-bonded and non-bonded bilayers, we employed the optimized configurations as discussed in Section 6.2.3. Self-consistent calculations for determination of their electronic structure were carried out with an energy cutoff of 30 Ry and 270 Ry for plane waves and charge density, respectively, and a  $2\times 2\times 1$  mesh for sampling the (BZ); the band structure was then calculated by a sequence of non-self-consistent calculations, using the path along the BZ as illustrated in the inset of Figure 6.2(a).

### 6.3 Geometrical Considerations and DFT Analysis of Interlayer-Bonded Configurations in Twisted Bilayer Graphene

Upon visual inspection of the moiré patterns that arise for rotation angles over the range  $15^\circ < \theta \leq 30^\circ$ , a geometrical analysis similar to the one described in Section 5.3 of the thesis was conducted; an interesting pattern can be observed in the  $\theta \rightarrow 30^\circ$  limit, i.e., where the bilayer consists of one zigzag- and one armchair-oriented plane. Such patterns have been observed in STM images of few-layer epitaxial graphene (Hass et al., 2008) and ultrasonicated exfoliated graphene (Warner et al., 2009) for angles of  $\theta = 30 \pm 2.204^\circ$  and  $30^\circ$ , respectively.

The moiré pattern generated from a pair of planes rotated by  $\theta = 30^\circ$  is shown in Figure 6.3(a). The existence of an apparent superlattice can be observed, as marked by the dotted lines. In the center of each unit cell of this superlattice, a relatively well-ordered collection of atoms shaded dark (colored blue online) is depicted; these atoms are the most likely to form C-C interlayer bonds in the bilayer. However, the two layers are not perfectly commensurate: considering that the lattice parameters  $a$  of both graphene planes are identical, the superlattice vectors for each individual plane do not have the same length: the corresponding cell edge lengths are  $12a_{cc}$  for the armchair-oriented ( $4\sqrt{3} \times 4\sqrt{3}$  R $30^\circ$  supercell) versus  $7\sqrt{3}a_{cc}$  for the zigzag-oriented ( $7 \times 7$  supercell) plane, where  $a_{cc}$  is the C-C bond length. Shallcross and coworkers (Shallcross et al. 2008a, 2010) presented an elegant analytical solution for the existence of commensurate graphene bilayers. By using this solution, we did not find commensurability for an exact angle of  $\theta = 30^\circ$  for supercells containing less than  $\sim 10^5$  atoms. For smaller supercell

sizes, we found commensurability for  $\theta = 30 \pm 0.5907^\circ$  (388 atoms) and  $\theta = 30 \pm 0.1583^\circ$  (724 atoms); the closest to  $30^\circ$  angle that we found for commensurability was  $\theta = 30 \pm 0.0008^\circ$ , for a much larger supercell size (140452 atoms).

To generate a  $\theta = 30^\circ$  rotated commensurate bilayer, as depicted in Figure 6.3(a), the twisted bilayer graphene planes need to be slightly strained and further relaxed; one plane expands and the other shrinks (by a factor of  $12/7\sqrt{3}$ ) due to the initial mismatch. According to our DFT calculations, the new strained/relaxed planes have an average bond length of 1.4158 Å and 1.4012 Å, respectively, compared to the original ones of 1.4081 Å (a decrease/increase of  $\sim 0.5\%$ ). The supercell contains a total of 194 atoms, 96 from one layer and 98 from the other, and the predicted equilibrium interlayer spacing is 3.38 Å, consistent with DFT values previously reported for twisted bilayers (Campanera et al., 2007; Latil et al., 2007; Hass et al., 2008; Shallcross et al., 2008b).

Interlayer C-C bonds are then created for either the atoms on the border of the shaded regions, or the atoms beyond the border marked by circles and diamonds in Figure 6.3(c), by simply displacing normal to the bilayer plane the atoms in each layer and relaxing the resulting structure; two different structures can be formed, both upon creation of 12 consecutive interlayer C-C bonds. On the upper-right corner and on the bottom of Figure 6.3(c), two different side views of the two generated structures are shown. The structure generated upon creation of interlayer bonds between the atoms on the border of the shaded regions is examined first; it consists of a circular cage-like atomic configuration embedded within the bilayer. If this caged structure is removed from the layers and relaxed further, it forms a  $C_{48}$  fullerene (space group symmetry  $D_{6d}$ ), as illustrated in the left panel of Figure 6.3(d). Comparison of the embedded and the

removed/relaxed structures shows clearly that the fullerene configuration is strained when embedded within the layers.

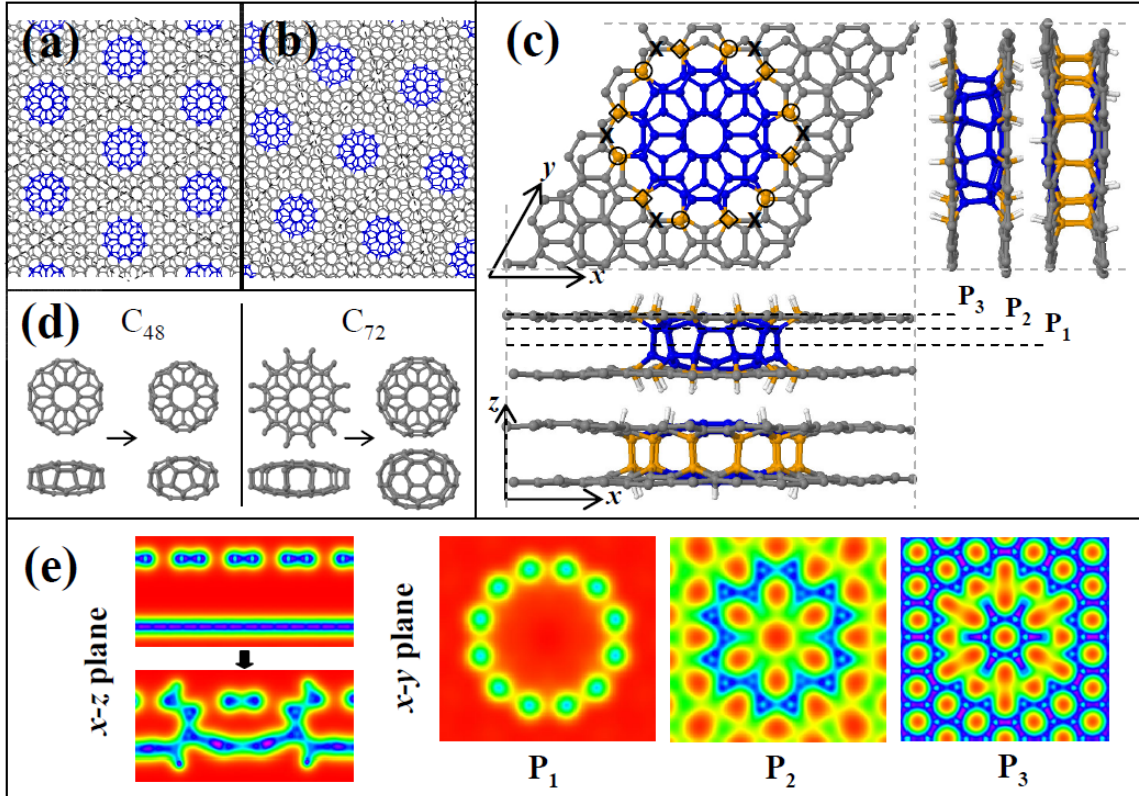


**Figure 6.3.** (a, b) Moiré patterns generated by a pair of graphene layers rotated by angles of  $\theta = 30^\circ$  and  $\theta = 30 \pm 2.204^\circ$  with respect to each other, respectively. The dark shaded atoms (colored blue online) correspond to those involved in the creation of the embedded caged structures; dotted lines are used to visualize the superlattices. (c) Supercell for a  $\theta = 30^\circ$  twisted bilayer and top and side views of the interlayer-bonded configurations generated. Open squares, open diamonds, and X marks are used to denote either interlayer bonded or hydrogenated C atoms. The shaded (colored online) atoms are removed from the structure and relaxed, generating the  $C_{48}$  and  $C_{72}$  fullerenes, different views of which are depicted in (d). For each panel in (d), caged structures removed from the bilayers (left side) and relaxed further (right side) are presented. (e) Valence electron density (VED) distributions on planes normal to the surface of the pristine and bonded bilayers (top and bottom, respectively, in the image on the left), and on planes  $P_1$ ,  $P_2$ , and  $P_3$  parallel to the graphene layers at different positions, as defined in (c). The VED increases as the color changes from red (zero VED) to blue. For interpretation of the references to color in the VED distributions, the reader is referred to the online version of this thesis.

To stabilize this bonded structure, hydrogen atoms are required for passivation of some of the resulting dangling bonds, similarly to the hydrogenated interlayer-bonded bilayers presented by Leenaerts and coworkers (Leenaerts et al., 2009), and Chernozatonskii and coworkers (Chernozatonskii et al., 2009); the presence of chemisorbed H atoms introduces an  $sp^3$  character to the neighboring bonds, favoring the creation of the interlayer bonds and stabilizing the resulting structure. To check the thermodynamic stability of the structures as a function of the amount of chemisorbed H, we define the binding energies for interlayer-bonded and –non bonded structures,

$$E_{bb} \equiv (E_{BGHbonded} - E_{BGpristine} - N_H E_H) / N_H \quad (6.1)$$

and

$$E_{bn} = (E_{BGHnonbonded} - E_{BGpristine} - N_H E_H) / N_H \quad (6.2)$$

where  $E_{BGHbonded}$  and  $E_{BGHnonbonded}$  correspond to the energies of hydrogenated interlayer-bonded and -nonbonded structures respectively,  $E_{BGpristine}$  is the energy of the pristine bilayers,  $E_H$  is the energy of an isolated hydrogen atom and  $N_H$  is the number of H atoms used. The binding energies for structures with different hydrogenation patterns and hydrogen coverages are summarized in Table 6.2. The cases investigated are labeled as (A) one H atom chemisorbed onto the outer side of each layer for each inter-shell bond (24 H atoms) at the C atoms marked by either circles or diamonds in Figure 6.3(c); (B) one H atom chemisorbed onto only one of the two layers for each inter-shell bond (12 H atoms) at the C atoms marked by either circles or diamonds in Figure 6.3(c); (C) one H atom chemisorbed for each inter-shell bond (12 H atoms) at the C atoms marked by circles onto both layers and (D) by diamonds onto one layer and by circles onto the other;

and (E) with one H atom chemisorbed for every two inter-shell bonds (6 H atoms) at the C atoms marked by circles on one side.

**Table 6.2.** Binding energies for interlayer bonded ( $E_{bb}$ ) and non-bonded ( $E_{bn}$ ) structures of  $\theta = 30^\circ$  and  $30 \pm 2.204^\circ$  twisted bilayers for different numbers of chemisorbed H atoms,  $N_H$ , and different hydrogenation patterns (A)-(G).

$\theta(^{\circ})$	case	$N_H$	$E_{bb}$ (eV)	$E_{bn}$ (eV)
30	A	24	-2.211	-2.585
30	B	12	-1.316	-2.761
30	C	12	-1.220	-2.428
30	D	12	-1.223	-2.411
30	E	6	0.736	-2.646
30	F	12	-1.690	-2.229
30	G	6	0.690	-2.461
$30 \pm 2.204$	A	24	-2.059	-2.436
$30 \pm 2.204$	B	12	-0.998	-2.473
$30 \pm 2.204$	C	12	-1.035	-2.275
$30 \pm 2.204$	D	12	-1.053	-2.270
$30 \pm 2.204$	F	12	-1.448	-2.137

The results of Table 6.2 show that at least 12 H atoms, one for each interlayer bond, are required to make the final structure more stable than the reference state (pristine bilayer + atomic hydrogen); the most stable configuration is the one containing two H atoms per interlayer bond (case A). Structure (A) also is perfectly symmetric with respect to the  $x$ - $y$  plane; for the other configurations (B-E), bond lengths and angles change slightly due to the smaller number of chemisorbed H atoms. Increasing the  $sp^3$  bonding character introduced by H chemisorption improves the stability of the resulting structure. Comparing the binding energies for the hydrogenated interlayer bonded ( $E_{bb}$ ) and non-bonded ( $E_{bn}$ ) bilayers implies that the non-bonded ones are always more stable than the bonded ones, i.e., the interlayer-bonded structures presented here are metastable.

Calculating energy barriers for the transition between these two states is beyond the scope of this study.

Figure 6.3(e) shows the valence electron density (VED) maps for different planes of the structure,  $P_1$ ,  $P_2$ , and  $P_3$ , as defined in Figure 6.3(c), with the configuration of hydrogenation pattern (A); by comparing the maps on the  $x$ - $z$  plane, for the pristine non-bonded and the hydrogenated and interlayer-bonded states, the formation of covalent C-C bonds between the two adjacent layers is evident. The same covalent bonding can be seen in the VED maps for the planes parallel to the layers ( $x$ - $y$ -planes), especially in the plane marked as  $P_2$ , which intersects the interlayer bonds.

Another caged fullerene-like structure can be formed within graphene planes rotated at  $\theta = 30^\circ$  from formation of C-C bonds between the atoms marked by circles and diamonds in Figure 6.3(c); this is illustrated in the different views shown in the bottom and upper-right images of Figure 6.3(c). In this case, the caged structure formed is larger, containing 72 C atoms; the relaxed structure resulting from removing this  $C_{72}$  fullerene is shown in the right panel of Figure 6.3(d). Due to the presence of two-fold-coordinated atoms on the border of the removed structure, there is a rearrangement of bonds in this region (reconstruction) during structural relaxation. The embedded, unreconstructed  $C_{72}$  structure is not a stable fullerene contrary to the  $C_{48}$  structure of Figure 6.3(d), which preserves the same symmetry before and after removal from the bilayer and relaxation and does not require reconstruction. To generate the corresponding interlayer-bonded structures, H atoms were chemisorbed at the positions shown by X-marks on Figure 6.3(c), onto either both or one of the layers (total of 12 and 6 H atoms, respectively), labeled as cases (F) and (G), respectively; the corresponding

binding energies also are presented in Table 6.2. For the same number of chemisorbed H atoms, the embedded  $C_{72}$  structure is more stable than the embedded  $C_{48}$  one due to the perfect alignment (in  $z$ ) in the initial configuration of the C atoms to be bonded and the resulting smaller strain imposed on the entire structure.

Structures similar to the ones illustrated in Figure 6.3(c) (cases A-G), also can be generated from bilayers with graphene planes rotated by angles deviating slightly from the ideal angle of  $30^\circ$ . A perfectly commensurate superlattice with a relatively small supercell size exists in this neighborhood at  $\theta = 30 \pm 2.204^\circ$  (with 52 atoms and both layers forming  $\sqrt{13} \times \sqrt{13}$   $R46.1^\circ$  supercells) as demonstrated in earlier studies (Kolmogorov and Crespi, 2005; Latil et al., 2007; Shallcross et al., 2008a,b) and observed experimentally (Hass et al., 2008). The corresponding moiré pattern is depicted in Figure 6.3(b); the unit cells of the superlattice (containing 104 atoms for each graphene layer) are marked by the dotted lines; the C atoms that participate in the formation of the caged structures similar to the ones for  $\theta = 30^\circ$  are shaded dark (colored blue online). The predicted equilibrium interlayer spacing is  $3.385 \text{ \AA}$ , consistent with values reported in the literature for twisted bilayer graphene of the same  $\theta$  (Hass et al., 2008; Shallcross et al., 2008b). It should be mentioned that the supercell used in the calculations ( $2\sqrt{13} \times 2\sqrt{13}$   $R46.1^\circ$ ) is four times larger than the one of minimum size; due to the strain and deformation upon bond formation, creation of interlayer bonded structures in two consecutive units of this smaller superlattice is unlikely. Therefore, we consider that the interlayer-bonded structures are formed only within the shaded regions of Figure 6.3(b), and we repeat the same procedure described before to obtain the corresponding relaxed structures. These are completely analogous to the ones depicted in Figure 6.3(c), but

characterized by a slightly higher strain compared to those for  $\theta = 30^\circ$ , as reflected in the changes on the C-C bond lengths (discussed below) and binding energies. The corresponding results for the energies as function of the H coverage and distribution are summarized in Table 6.2 (only the cases that generate stable structures are presented). Observations analogous to those for  $\theta = 30^\circ$  can be made, regarding the relative stability of the structures.

Top and side views of the embedded  $C_{48}$  and  $C_{72}$  caged configurations generated by interlayer bonding of twisted bilayers is shown in Figures 6.4(a) and (b), respectively, depicting some characteristic bond lengths  $d_k$ ,  $k = 1, \dots, 10$ . Due to symmetry, equivalent atom positions along the periphery of the caged structures result identical bond lengths. Table 6.3 lists the numerical values for the bond lengths,  $d_k$ , corresponding to relaxed structures of interlayer-bonded configurations with hydrogenation patterns (A), (B) ( $C_{48}$  embedded structure), and (F) ( $C_{72}$  embedded structure), generated from twisted bilayers with rotation angles of  $\theta = 30^\circ$  and  $\theta = 30 \pm 2.204^\circ$ .

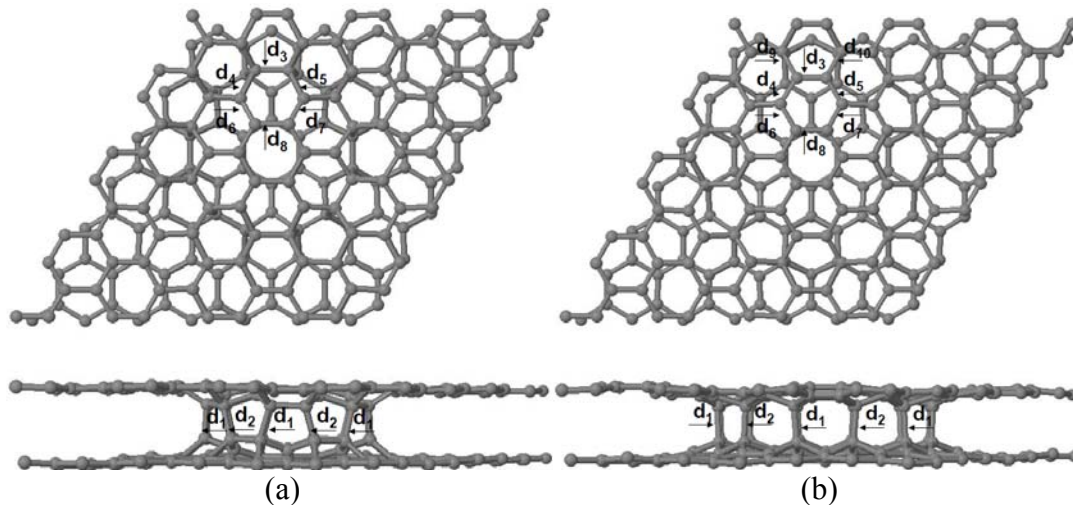


**Figure 6.4.** Characteristic bond lengths for (a)  $C_{48}$  and (b)  $C_{72}$  embedded caged structures generated by interlayer bonding in the  $\theta = 30^\circ$  twisted bilayer; for the  $\theta = 30 \pm 2.204^\circ$  twisted bilayer, the supercell is different, but the internal caged structure has the same geometry. Chemisorbed H atoms have been removed from the configurations for clarity.

**Table 6.3.** Values for the characteristic bond lengths as defined in Figure 6.4 for hydrogenation patterns (A), (B), and (F), for the  $\theta = 30^\circ$  twisted bilayer and hydrogenation patterns (A) and (F) for the  $\theta = 30 \pm 2.204^\circ$  twisted bilayer. For each entry ( $d_k, k > 2$ ), two values are given, corresponding to the bond lengths at the top and bottom layer of the bilayer.

bond length (Å)	(A), $30^\circ$	(B), $30^\circ$	(A), $30 \pm 2.204^\circ$	(F), $30^\circ$	(F), $30 \pm 2.204^\circ$
$d_1$	1.576	1.591	1.559	1.636	1.630
$d_2$	1.576	1.639	1.593	1.636	1.643
$d_3$	1.532, 1.517	1.525, 1.516	1.519, 1.519	1.361, 1.354	1.358, 1.358
$d_4$	1.503, 1.488	1.501, 1.490	1.494, 1.494	1.422, 1.412	1.416, 1.416
$d_5$	1.503, 1.488	1.486, 1.476	1.493, 1.493	1.422, 1.412	1.415, 1.415
$d_6$	1.347, 1.340	1.348, 1.344	1.345, 1.345	1.418, 1.410	1.414, 1.414
$d_7$	1.347, 1.340	1.348, 1.344	1.345, 1.345	1.418, 1.410	1.414, 1.414
$d_8$	1.478, 1.467	1.475, 1.463	1.468, 1.468	1.427, 1.418	1.421, 1.421
$d_9$	-	-	-	1.507, 1.495	1.503, 1.503
$d_{10}$	-	-	-	1.507, 1.495	1.499, 1.499

The results of Table 6.3 show that for a given caged structure generated by interlayer bonding, the corresponding bond lengths  $d_k$  vary with the hydrogenation pattern and with the rotation angle of the twisted bilayers. Chemisorption of H atoms introduces  $sp^3$  bonds into the structure, affecting the C-C bonds in the neighboring atoms: this effect can be observed by comparing the bond lengths of the structures generated with hydrogenation patterns (A) and (B) (24 and 12 atoms respectively) in the  $\theta = 30^\circ$  twisted bilayer. Similar observations can be made for the other patterns investigated, (C), (D), and (E) (not discussed here). In general, the larger the number of chemisorbed H atoms onto the C atoms in the vicinity of the interlayer bonds, the shorter the interlayer C-C bonds become (getting closer to the typical C-C  $sp^3$  bond length of  $\sim 1.54$  Å). Also, it can be observed that for the configurations generated from a  $\theta = 30^\circ$  twisted bilayer, there is a difference between the in-plane C-C bond lengths in each layer; this is due to the slight strain imposed on the layers in order to make them commensurate, as discussed in the previous paragraphs.

The results of Table 6.3 also indicate that the bond lengths are affected by the rotation angle of the twisted bilayer; deviations from the ideal angle of  $30^\circ$  distort the interlayer bonds slightly, giving rise to two characteristic bond lengths arranged in an alternated pattern around the periphery of the caged structures. However, due to the commensurability of layers in the  $\theta = 30 \pm 2.204^\circ$  case, the in-plane C-C bond lengths remain the same in each layer.

#### 6.4 Electronic Structure of Interlayer-bonded Configurations

Figure 6.5 shows the electronic band structures of pristine twisted bilayer graphene (rotation angles of  $\theta = 30^\circ$  and  $\theta = 30 \pm 2.204^\circ$ ), and the corresponding hydrogenated interlayer-bonded and non-bonded configurations. For the interlayer-bonded structures, the results for hydrogenation patterns (A) and (F) (that generate symmetric  $C_{48}$  and  $C_{72}$  cages) only are considered. Energy bands are plotted along the path connecting the special points  $\Gamma$ -M-K- $\Gamma$  in the Brillouin zone of the supercell; the bands are shifted in the vertical direction in order to make the Dirac-point energy coincide with the Fermi level. For the pristine bilayers (dotted blue curves in Figure 6.5), the band structures preserve the essential features of single-layer graphene (SLG), due to the effective electronic decoupling of layers (Latil et al., 2007; Hass et al., 2008; Shallcross et al., 2008a,b, 2010; Sprinkle et al., 2009): the characteristic Dirac cone at the K point (with the same Fermi velocity as that of SLG) is present in both cases and is doubly degenerate for  $\theta = 30 \pm 2.204^\circ$  and not degenerate for  $\theta = 30^\circ$ . In the latter case, a second Dirac cone appears at the  $\Gamma$  point, being also degenerate. This difference can be understood in terms of the band structures for the individual single-layered graphene

supercells which form the twisted bilayer graphene structures under investigation, presented in Figure 6.6. As a consequence of the effective electronic decoupling, the energy bands for the bilayer can be seen as a “superposition” of the bands of each layer. For the commensurate case ( $\theta = 30 \pm 2.204^\circ$ , two  $2\sqrt{13} \times 2\sqrt{13}$   $R \pm 46.1^\circ$  graphene supercells), depicted in Figure 6.6(c), both of the layers have identical band structure; consequently, the bilayer exhibits doubly degenerate Dirac cones at the K point of the BZ and away from the K point, the bands are perturbed compared to the single-layer case due to the interaction between layers (Shallcross et al., 2010), as seen in Figures 6.5 (c) and 6.5(d).

For the  $\theta = 30^\circ$  twisted bilayer, each layer possesses a different band structure due to its different orientation, as illustrated in Figures 6.6(a) and 6.6(b); the band structure for the zigzag-oriented layer ( $7 \times 7$  graphene supercell), exhibits the characteristic Dirac cone at the K point of the BZ, similarly to the commensurate bilayer, with the  $\{K, K'\}$  points of graphene BZ folding into the analogous  $\{K, K'\}$  points of the supercell BZ. However, for the armchair-oriented layer ( $4\sqrt{3} \times 4\sqrt{3}$   $R 30^\circ$  graphene supercell), a degenerate Dirac cone appears at the  $\Gamma$  point, as a consequence of the folding of both the K and the K' points of the graphene BZ into the  $\Gamma$  point of the supercell BZ (García-Lastra et al., 2010; Martinazzo et al., 2010; Casolo et al., 2011). Therefore, the band structure of the bilayer exhibits two Dirac cones, as depicted in Figures 6.5(a) and 6.5(b), with curves slightly shifted in the vertical direction compared to their single-layer counterparts due to the interaction between layers.

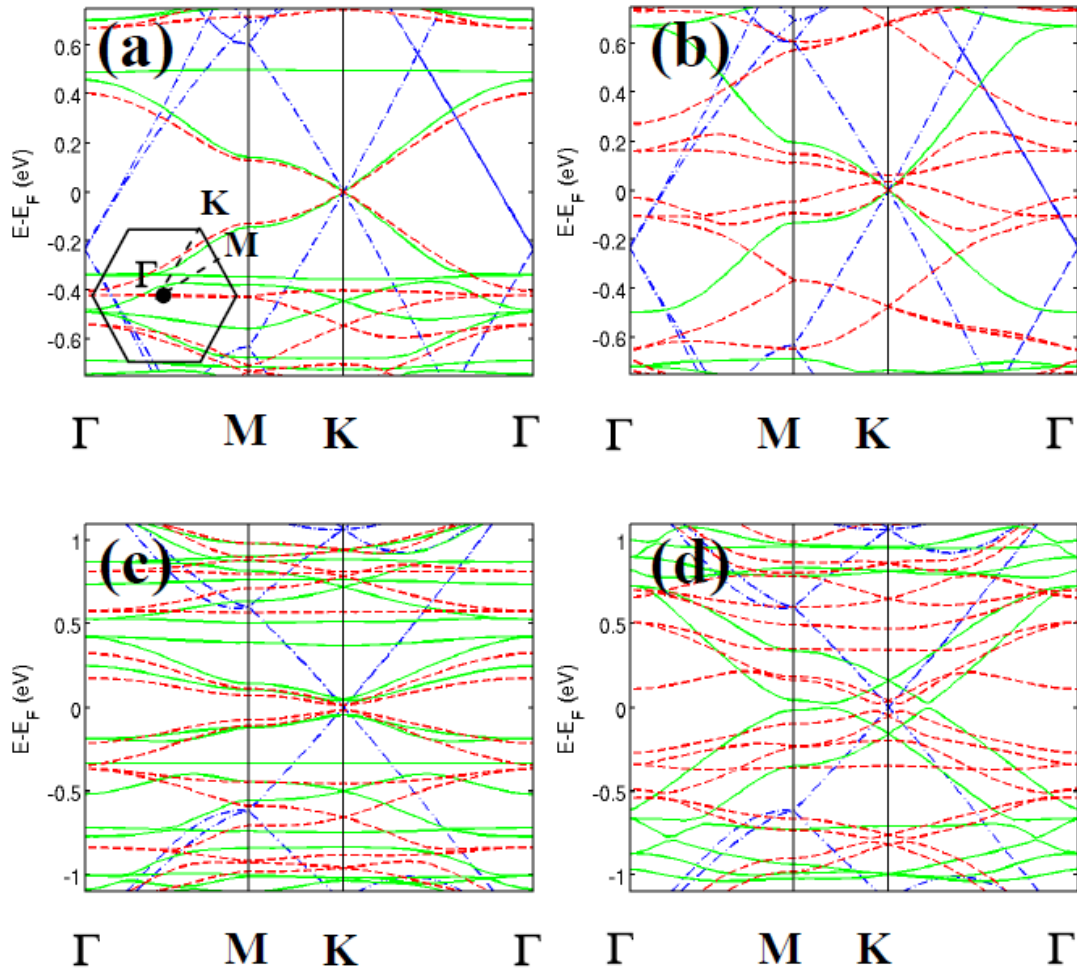


**Figure 6.5.** Electronic band structures for pristine (dotted blue curves), hydrogenated interlayer-bonded (solid green curves), and hydrogenated non-bonded (dashed red curves) twisted bilayer graphene for rotation angles of (a,b)  $\theta = 30^\circ$  and (c,d)  $\theta = 30 \pm 2.204^\circ$ . Band diagrams correspond to configurations (a,c) with hydrogenation pattern (A) and (b,d) with hydrogenation pattern (F), generating embedded  $C_{48}$  and  $C_{72}$  caged structures, respectively. The energies are plotted along the path in the Brillouin zone illustrated in the inset.

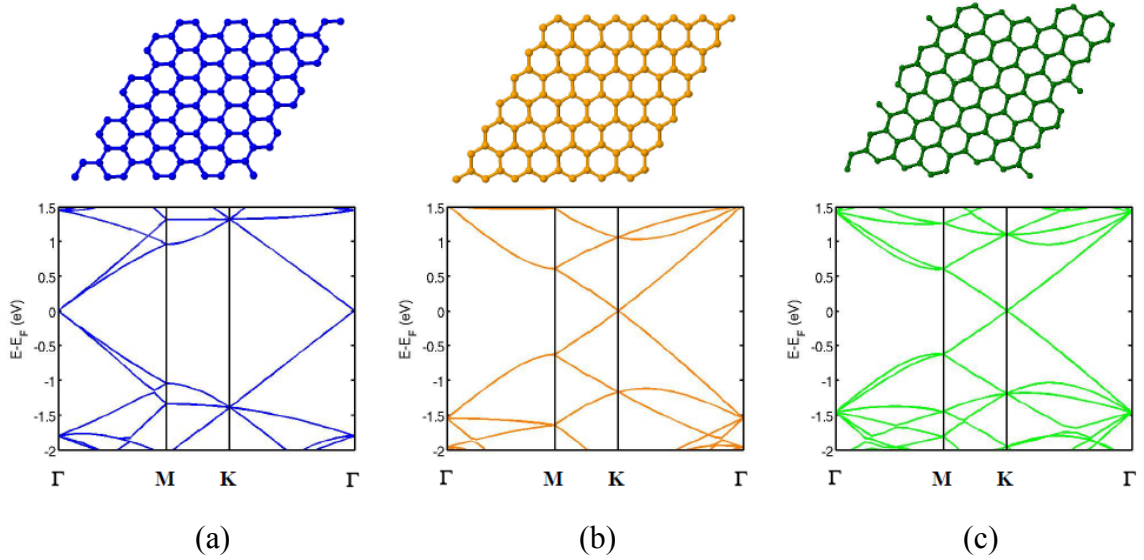


**Figure 6.6.** Supercells (top) and corresponding band structures (bottom) of (a) armchair-oriented layer ( $4\sqrt{3}\times 4\sqrt{3}$  R $30^\circ$  supercell); (b) zigzag-oriented layer ( $7\times 7$  supercell); and (c) layer ( $2\sqrt{13}\times 2\sqrt{13}$  R $46.1^\circ$  supercell) rotated by  $16.1^\circ$  with respect to layer in (b).

Introduction of  $sp^3$  bonding into the structure due to hydrogenation and creation of interlayer bonds would be expected to open a band gap at the K point (Duplock et al., 2004; Leenaerts et al., 2009; Chernozatonskii et al., 2009; Balog et al., 2010); however, creation of defects in superlattices with specific symmetries may preserve the Dirac cones or open gaps of different widths, as recently demonstrated for superlattices of chemisorbed H atoms (García-Lastra et al., 2010; Martinazzo et al., 2010), substitutional defects (Casolo et al., 2011), and antidot lattices (Petersen et al., 2011).

In the  $\theta = 30^\circ$  case, Figures 6.5(a) and 6.5(b), hydrogenation and creation of interlayer bonds preserve the Dirac cones around the K point for both embedded caged structures (A) and (F) with a reduction of the Fermi velocity compared to the pristine bilayer. For interlayer-bonded structure (F), no gap is predicted, while the opening of a very narrow gap on the order of 1 meV was found for interlayer-bonded structure (A), as well as for the non-bonded states; the presence of such a narrow gap may be related to the

off-plane distortion induced by the creation of  $sp^3$  bonds, similar to what was reported for superlattices of substitutional defects (Casolo et al., 2011). Comparing the electronic structures of configurations (A) and (F), Figures 6.5(a) and 6.5(b), reveals strong similarities in the band structures of the interlayer-bonded configurations, while those of the non-bonded ones differ due to the different arrangement of the H atoms chemisorbed onto the surface; for the non-bonded configuration (A), the energy dispersion relation in the vicinity of the K point differs only slightly from that of the corresponding interlayer-bonded one. For the non-bonded configuration (F), midgap states arise around the K point, crossing conduction bands; as a result, this configuration exhibits a metallic behavior.

Figures 6.5(c) and 6.5(d) illustrate that the effect of hydrogenation and interlayer bonding on the band structure for  $\theta = 30 \pm 2.204^\circ$  is different from that for  $\theta = 30^\circ$ . In both cases (A) and (F), creation of the caged configurations, or simply hydrogenation of the bilayers according to Figure 6.3, causes a band gap opening and the loss of the linear dispersion around the K point. This difference in the observed changes on the band structure near the Fermi level due to creation of interlayer bonded configurations in  $\theta = 30^\circ$  and  $\theta = 30 \pm 2.204^\circ$  twisted bilayers may be related to the difference in the superlattice unit cell sizes ( $7a$  and  $2\sqrt{13}a$ , respectively), or in their orientation with respect to the underlying graphene lattice. Petersen and coworkers (Petersen et al., 2011) shows that the formation of graphene antidot lattices (superlattices of holes on SLG) may or may not lead to a band gap opening, depending on hole geometry and diameter, superlattice symmetry, and cell size; for honeycomb superlattices, for example, 1/3 of the possible

configurations lead to band gap opening, while the remaining 2/3 are shown to retain the Dirac cones.

## 6.5 Larger Embedded Caged Configurations

Structural optimization with DFT for supercells containing more than a few hundred atoms becomes computationally very demanding. Consequently, to investigate interlayer bonded structures involving supercells much larger than those of Figure 6.3 and 6.4, we employed classical MD-based structural relaxation according to the AIREBO potential (Stuart et al., 2000), as discussed in Section 6.2.3. Geometrical analysis of the moiré patterns formed by planes rotated by  $\theta = 30^\circ$  shows that, following the same procedure described above, many other embedded caged structures could be formed of size larger than the  $C_{48}$  and  $C_{72}$  configurations. Figures 6.7 and 6.8 show some of these structures, as predicted by AIREBO. These structures have a larger number of interlayer bonds  $N_{IB}$ , and more distinct shapes; this specific class of configurations can be viewed as the result of “coalescence” of a sequence of units defined by the basic structure of the  $C_{48}$  embedded fullerene.

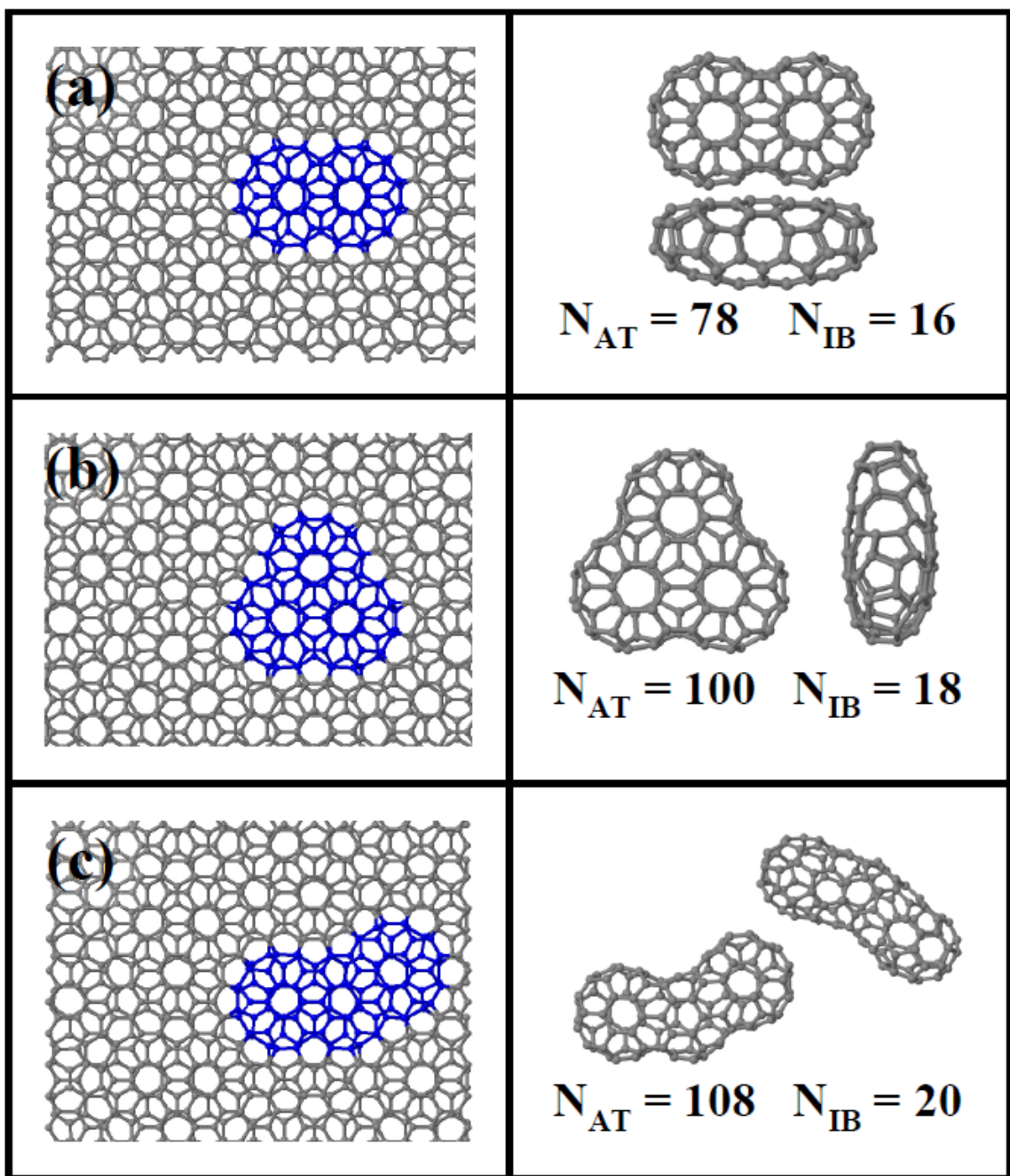


**Figure 6.7.** (a-c) Embedded caged structures formed by interlayer C-C bonding in a  $\theta = 30^\circ$  twisted bilayer, containing different numbers of atoms ( $N_{AT}$ ) and interlayer bonds ( $N_{IB}$ ). In each case, the atoms involved in the creation of the interlayer-bonded configurations are marked on the left side of each panel, and different views of the removed/relaxed fullerenes are displayed on the right.

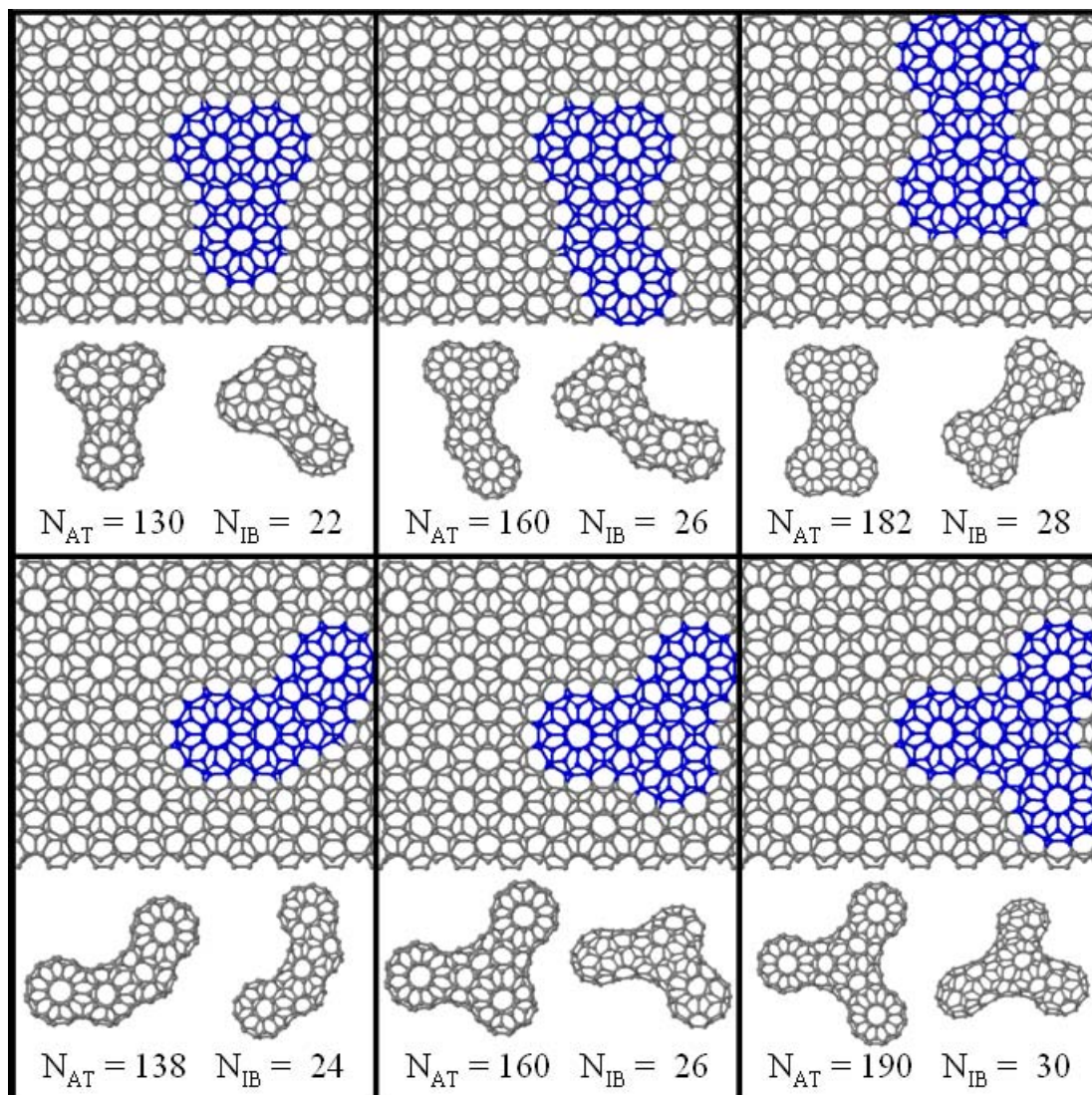


**Figure 6.8.** Additional embedded caged configurations formed by interlayer bonding in a  $\theta = 30^\circ$  twisted bilayer containing different numbers of atoms ( $N_{AT}$ ) and interlayer bonds ( $N_{IB}$ ). The atoms involved in the creation of the interlayer-bonded configurations are marked at the top of each panel, and different views of the removed/relaxed fullerenes are displayed at the bottom.

## 6.6 Summary and Conclusions

In conclusion, we have proposed a novel type of carbon nanostructures, consisting of caged fullerene-like configurations embedded within planes of twisted bilayer graphene; these structures are formed as a result of interlayer C-C bonding for graphene

planes rotated with respect to each other by angles around  $30^\circ$ . The electronic structure of a specific sub-class of these carbon nanomaterials preserves at least partially the electronic character of single-layer graphene around the K point, which endows it with some of its unique properties. Our findings have far reaching implications: 2-D carbon nanostructures can be functionalized by generating superstructures through embedding of 0-D carbon structures to tailor their electronic properties without deviating from those of SLG. This embedding of fullerene-like structures can be accomplished by chemical modification through hydrogenation to form certain patterns of chemisorbed H. We have found these structures to be less stable than their hydrogenated non-bonded counterparts at low pressure; under higher pressure, these structures are expected to become thermodynamically more favorable. The structures proposed in the present study may be related to the intermediate carbon phases observed in laser-induced shock wave loading (Luo et al., 2005) and high-temperature shock compression (Kurdyumov et al., 2006) experiments on graphitic samples, which were likely to exhibit a turbostratic stacking of planes. Luo and coworkers (Luo et al., 2005) have demonstrated that a “crystalline carbon-cage structure occupying a transitional state intermediate between (fullerene)  $C_{60}$  polymerization and graphite interlayer bridging” explains reasonably the X-ray diffraction patterns exhibited by the synthesized samples. The conceptual similarity between this hypothetical structure and the ones presented in this chapter is evident. However, compared to the structure proposed by Luo and coworkers (Luo et al., 2005), our proposed configurations possess a straightforward geometrical relationship with the graphene planes which were involved in their generation. Additional studies are required to elucidate the possible relationship between the proposed structures in the present study

and the inconclusive intermediate phases observed in the aforementioned experiments (Luo et al., 2005; Kurdyumov et al., 2006).

## CHAPTER 7

### SUMMARY, CONCLUSIONS AND FUTURE DIRECTIONS

#### 7.1 Summary and Conclusions

This thesis presented a comprehensive atomic-scale computational analysis of the structural transformations in carbon nanotubes and graphene induced by hydrogenation and interlayer C-C bonding. A synergistic combination was employed of computational techniques, namely, molecular-dynamics and Monte Carlo simulations, as well as first-principles DFT calculations, aiming to explore different aspects of the problems addressed. Chapters 3 and 4 focused on the effects of hydrogen chemisorption on the structure and morphology of single-layered materials, while Chapters 5 and 6 explored configurations generated by interlayer C-C bonding in multi-layered carbon structures, where the presence of atomic H is crucial for the synthesis process and stability of the resulting nanostructures.

Chapter 3 discussed in depth the effects of hydrogen chemisorption and the associated  $sp^2$ - $sp^3$  C-C bonding transition on the structure and morphology of single-walled nanotubes and graphene layers. This bonding transition gives rise to a “swelling effect”, which depends strongly on the H surface coverage  $\Theta$ ; for low coverages, swelling is negligible, but beyond a critical coverage value, an increase in  $\Theta$  leads to a monotonic and eventually linear increase in the characteristic lengths of the materials. Chemisorption of H also affects the roughness of the surface, which reaches a maximum at intermediate surface coverages. The implementation of a methodology for finding the

most energetically favorable H distributions on the surfaces demonstrated that chemisorbed H atoms tend to form clusters on the surfaces and an excellent qualitative agreement of these distributions was found with a series of experimental observations. The combination of these effects results in an interesting morphology for hydrogenated graphitic surfaces, characterized by the presence of intercalated regions of positive and negative curvature (resembling valleys and hills in a landscape). These features are correlated directly with the distribution of H atoms on the surface; regions corresponding to the clustered hydrogenated  $sp^3$ -hybridized sites are displaced outwards from the pristine surface (“hills”) and are surrounded by continuous chains of non-hydrogenated  $sp^2$ -hybridized sites that are displaced inwards (“valleys”).

The dependence of nanotube dimensions on hydrogen surface coverage that was reported in Chapter 3 was used to provide an alternative explanation about the inconsistencies in the H storage capacity of SWCNT bundles reported in the literature. The hydrogenation-induced swelling of individual nanotubes results in a decrease of the free interstitial space available for diffusion of H atoms throughout the bundle; for low surface coverages, this effect is negligible and, as a result, incoming H atoms are able to penetrate the bundle and reach its innermost tubes. When the coverage reaches the critical value for the onset of swelling, the interstitial spacing starts decreasing and, consequently, it might hinder the diffusion of H atoms throughout the bundle, depending on the initial bundle density and CNT diameter distribution. This mass-transfer limitation causes a non-uniformity of bundle hydrogenation and may limit the hydrogen storage capacity of the CNT bundles. An analytical mathematical model, properly parameterized by atomistic calculations, was developed to describe this phenomenon.

The model predicts the maximum H storage capacity that can be achieved for a SWCNT bundle as a function of process parameters, providing guidelines for the optimization of the amount of hydrogen stored in such a medium.

The MWCNT-to-diamond transition induced by exposure to a H<sub>2</sub> plasma reported in the literature (Sun et al., 2004a, b; Yang et al., 2007), motivated the investigation of the effects of hydrogenation on multi-layered carbon materials. In Chapter 5 of the thesis the crystalline phases were explored that can be formed within walls of MWCNTs through creation of C-C inter-shell bonds between adjacent graphene walls. It was found that inter-shell bonding in MWCNTs generates ordered local structures that resemble the crystalline structure of either cubic or hexagonal diamond; these local structures may act as seeds for the nucleation of crystalline phases embedded within the graphitic matrix, as observed in experimental studies. The resulting structures are determined by the relative alignment of adjacent graphene walls in the original MWCNT. The key parameter that determines the type and size of the generated nanocrystals is the chiral-angle difference between adjacent graphene layers/walls in the original structure; for values of this angle up to  $\sim 15^\circ$ , diamond-like local structures can be formed, regardless of the chirality/diameter of the individual nanotube walls.

In Chapter 6, interlayer bonding in multilayered carbon nanomaterials was studied in the case where adjacent planes/walls are rotated with respect to each other by angles larger than the limiting value of  $\sim 15^\circ$ ; for simplicity, only the planar case was investigated. The analysis of moiré patterns generated by superposition of planes rotated with respect to each other at angles  $\theta \rightarrow 30^\circ$  showed that a different class of local structures emerges: interlayer bonding leads to creation of caged fullerene-like

configurations of different sizes embedded within the layers. The rotation angle of  $30^\circ$  provides the ideal alignment for creation of such structures, but small deviations from this value also allows their formation; analogous structures were generated for angles  $\theta = 30^\circ$  and  $\theta = 30 \pm 2.204^\circ$ . The electronic structure of the resulting nanomaterials was investigated and an interesting behavior was revealed: some of the unique electronic properties of pristine single-layer graphene, desired in many potential practical applications, are partially retained after creation of interlayer bonds, despite the introduction of  $sp^3$  bonding (due to H chemisorption and interlayer C-C bonding).

In summary, the findings presented in this thesis help explain a series of experimental observations previously reported in the literature. These findings also provide a set of experimentally testable hypotheses that may guide future experiments in the field. Undoubtedly, numerous questions regarding the topics addressed in the thesis remain unanswered. In the next Section, some suggestions for future theoretical and computational studies in the area are discussed.

## **7.2 Future Directions**

### **7.2.1 Hydrogenation of Single-layered Carbon Nanomaterials. Practical Consequences of Structural/Morphological Changes**

Chapter 3 discussed the structural and morphological changes induced by hydrogenation of graphene layers. A particular morphology was observed for hydrogenated surfaces at intermediate surface coverages: regions corresponding to clusters of hydrogenated sites are displaced outwards from the surface (“hills”) and are surrounded by continuous chains of non-hydrogenated sites that are displaced inwards

(“valleys”). Given these features, it is plausible to expect that the access of incoming H atoms to these non-hydrogenated sites is harder compared to that for a planar surface due to repulsive interactions between incoming H and the hydrogenated sites on the “hills” surrounding the “valleys”; the rougher the surface, the higher the energy required for an H atom to reach the available non-hydrogenated sites. Considering that surface diffusion of H atoms on hydrogenated surfaces is not favorable due to their tendency for clustering, as discussed in Chapter 3, the effect discussed above might be relevant to the saturation surface coverage (of around 50%) which has been observed consistently in different experiments on hydrogenation of graphene/graphite reported in the literature (Hornekær et al., 2006b; Luo et al., 2009; Allouche et al., 2005, 2006). Calculation of the energy barriers required for the diffusion of H atoms from the incoming flux to these available sites, which are deeper in the surface, in conjunction with thermodynamic considerations, sets the stage for providing definitive explanations to the observed saturation coverage.

Furthermore, it is worth investigating the effect of the surface coverage and the H distribution on the mechanical properties of hydrogenated graphene and carbon nanotubes, using molecular-dynamics simulations under constant strain rate, which allow for predicting, e.g., the corresponding Young’s modulus, tensile strength, and fracture strain. The optimized structures of Chapter 3 can be used directly in such an investigation, considering that their corresponding H distributions are in good agreement with experimental observations. Pei and coworkers (Pei et al., 2010) carried out such calculations for double-sided hydrogenated graphene layers, employing random H distributions; they observed that hydrogenation deteriorates the mechanical properties of graphene and that fracture always starts at the  $sp^3$  bonds inserted in the structure by

hydrogenation. If the surfaces used were consistent with the experimental observations, where hydrogenated sites (and consequently  $sp^3$  bonds) are clustered, a different dependence of the mechanical properties on hydrogen surface coverage is likely to be found. We would expect such a response to show that the effect of hydrogenation on the degradation of the mechanical properties is more severe than that reported by the authors (Pei et al., 2010).

### **7.2.2 Modeling of Mass Transfer Limitations in SWCNT Bundles**

The phenomenological model proposed in Chapter 4 describes how the swelling of SWCNTs upon hydrogenation leads to mass transfer and H storage capacity limitations when a bundle of nanotubes is exposed to a  $H_2$  plasma. This simple model can provide the starting point for the development of a more detailed model that is capable of predicting quantitatively the changes in the bundle properties resulting from hydrogenation. In the more detailed model, additional physics needs to be included for a more accurate description of hydrogenation effects. For example, the simplified model of Chapter 4 neglected any interactions between SWCNTs in the bundle. The inclusion of these interactions in the model will allow for a more accurate description of the effects of H chemisorption onto the SWCNTs of the bundle, although the overall qualitative picture does not change.

The minimum inter-tube spacing required for H diffusion ( $d_{\min}$ ) is the most important parameter for the hydrogen-storage capacity model developed; its determination is crucial for making quantitative predictions. Two approaches may be considered for the determination of  $d_{\min}$ . The first one consists of carrying out a

comprehensive set of molecular-dynamics simulations of the exposure of SWCNT bundles to H atoms in order to estimate the diffusion coefficient for H atoms in bundles. A systematic parametric study can be performed in order to verify the effect of parameters, including the intertube spacing,  $d$ , nanotube diameter and chirality, degree of hydrogenation of nanotubes, and temperature. The value for  $d_{\min}$  can be obtained by comparing the values of the diffusion coefficient estimated for various intertube spacings. A decrease in the intertube spacing, while keeping all the other parameters constant in the simulations, will cause a decrease in the diffusivity; extrapolation of the results as a function of  $d$  will provide a satisfactory estimate for  $d_{\min}$ .

The second complementary approach employs the Nudged Elastic Band (NEB) method (Jonsson et al., 1998; Henkelman et al., 2000) in conjunction with the AIREBO potential for calculating optimal pathways for the diffusion of a H atom through the intertube spacing  $d$  between two nanotubes in a bundle and the determination of the corresponding activation energy barrier. Comparing the energy barriers obtained at different values of  $d$  and extrapolating will give a satisfactory estimate of the minimum value for the spacing  $d_{\min}$ , at given temperature. The dependence of this energy barrier on the model parameters discussed in the implementation of the first approach also can be investigated.

### **7.2.3 Investigation of Mechanisms for Inter-shell/interlayer C-C Bonding in Multilayered Materials**

The specific role of atomic hydrogen in the MWCNT-to-diamond transition is an important point that has not been addressed in this thesis. A future study shall pursue a

fundamental understanding of how hydrogen atoms induce the nucleation of crystalline phases by facilitating inter-shell C-C bonding between adjacent graphene walls of MWCNTs, and determine the conditions required for accomplishing this transformation process. Furthermore, the possibility of formation of crystalline carbon phases other than cubic or hexagonal diamond will be analyzed. Toward these goals, the following specific research tasks should be executed.

AIREBO MD simulations can be used as an exploratory tool in the search for identifying the mechanisms responsible for the MWCNT-to-diamond transition. Simulations of the exposure of MWCNTs to hydrogen atoms can be carried out, over a range of processing conditions. The parameters to be varied in such an analysis include temperature, average MWCNT diameter, atomic H dose and presence/absence of defects in the graphene walls. Another approach to be considered in such an investigation is the use of *ab initio* molecular-dynamics simulations (Car and Parrinello, 1985), which also will serve the purpose of validating the AIREBO potential for this task.

Once the mechanisms that lead to formation of the  $sp^3$  C-C inter-shell bonds are identified, the corresponding optimal pathways can be constructed and the activation energy barriers can be calculated based on DFT calculations in conjunction with the NEB method (Jonsson et al., 1998; Henkelman et al., 2000). A comprehensive set of reaction pathways, with the respective activation energies will enable the future development of kinetic Monte Carlo (KMC) simulations to model this process over longer time scales.

In addition, it should be noticed that the inter-shell spacing in MWCNTs is a length comparable to that of the intertube spacing in a SWCNT bundle; both distances are determined by van der Waals interactions between individual graphene walls. This

similarity suggests that C-C bonding analogous to the inter-shell bonding in MWCNTs may occur in SWCNT bundles; in such a case, reactions between hydrogen atoms and the SWCNT walls in bundles would promote the crosslinking of individual nanotubes in the bundle. Such crosslinking of nanotubes in bundles has been observed in experiments of electron and ion irradiation of bundles (Krasheninnikov and Banhart, 2007), which resulted in an improvement of the mechanical properties of the nanotube bundle. The possibility that similar reactions may be induced by exposure of the bundles to H atoms also can be investigated.

#### **7.2.4 Investigation of Properties of Interlayer-bonded Structures in Twisted Bilayer Graphene**

In Chapter 6, we introduced a novel family of carbon-based nanostructures, consisting of caged fullerene-like configurations embedded within a pair of graphene layers rotated with respect to each other at angles  $\theta \rightarrow 30^\circ$ . It is worth conducting a comprehensive study toward determining the mechanical, optical, and magnetic properties of these nanostructures, as well as their expected X-ray diffraction patterns and spectra corresponding to different analytical methods; computation of diffraction patterns and spectra may follow an approach similar to that adopted for other theoretically-proposed carbon allotropes (Luo et al., 2005; Kurdyumov et al., 2006; Li et al., 2009; Umemoto et al., 2010). These synthetic spectra can be used to assess experimental studies on the synthesis of such structures, by direct comparison with analytical measurements.

In addition, *ab initio* molecular-dynamics simulations in conjunction with first-principles DFT/NEB calculations can be employed to investigate possible pathways and corresponding energy barriers for the formation of the structures, providing information about the required processing conditions for accomplishing the synthesis in practice.

For these novel interlayer-bonded nanomaterials, the computation of the electronic band structure revealed that, in certain cases, the characteristic Dirac cones at the *K* point of the Brillouin zone, which are directly related to the exotic and unique electronic properties of single-layer graphene (SLG), are preserved after H chemisorption and formation of the interlayer C-C bonds. It has been demonstrated that the chemisorption of even a single H atom onto graphene opens a band gap in the electronic structure (Duplock et al., 2004). A complete fundamental understanding of the reasons why the SLG-like electronic properties are retained (at least partially) in these cases remains elusive; the formation of superlattices of defects in SLG recently reported in the literature (García-Lastra et al., 2010; Martinazzo et al., 2010; Casolo et al., 2011; Petersen et al., 2011) may help provide the insights required to make progress in this direction.

## APPENDIX

### AIREBO POTENTIAL AND EVALUATION OF ITS PREDICTIVE CAPABILITIES

In the implementation of classical molecular-dynamics simulations, it is of crucial importance to choose an appropriate and reliable force field, that is capable of describing accurately the interatomic interactions in the material system under consideration. A suitable interatomic potential for the problems addressed in this thesis is the Adaptive Intermolecular Reactive Empirical Bonding Order (AIREBO) developed by Stuart and coworkers (Stuart et al. 2000), which has been extensively used for describing the interactions in solid carbon and hydrocarbon molecules. This potential is an improvement over the original Reactive Empirical Bonding Order (REBO) potential developed by Brenner (Brenner, 1990; Brenner et al., 2002), which is based on the concept of the bond-order function that was introduced by Tersoff and includes many-body effects into an effectively two-body (pair) potential (Tersoff, 1988).

AIREBO generates a typical reactive force field: it treats in an empirical way the formation and dissociation of covalent bonds, as well as the resulting changes in the atomic hybridization and coordination number. This version of the potential also accounts for the treatment of long-range interactions (van der Waals forces), which is of fundamental importance in the study of MWCNTs and SWCNTs bundles.

The AIREBO potential has the functional form

$$E = \sum_i \sum_{j \neq i} \left[ V_R(r_{ij}) - b_{ij} V_A(r_{ij}) + V_{vdw}(r_{ij}) + \sum_{k \neq i, j, l \neq i, j, k} V_{kijl}^{tors} \right], \quad (A1)$$

where  $r_{ij}$  is the distance between atoms  $i$  and  $j$ ,  $V_R(r_{ij})$  and  $V_A(r_{ij})$  denote pair-additive repulsive and attractive interactions, respectively, and  $b_{ij}$  is the bond-order function. These two terms alone constitute the original REBO potential. The terms  $V_{vdw}(r_{ij})$  and  $V^{tors}$  correspond to the long-range interactions and torsional potential, respectively, introduced by Stuart et al. in the AIREBO version of the force field (Stuart et al. 2000).

Many-body effects are introduced by the bond-order function  $b_{ij}$ , which depends on the local atomic coordination, bond angles, and conjugation effects. Quantum mechanics is not included explicitly in the description: hybridized states and conjugation are described by the system geometry (Stuart et al. 2000; Brenner et al., 2002). These articles (Stuart et al. 2000; Brenner et al., 2002) give a complete description of the functional forms of each term in Eq. (A1), the procedure employed in the parametrization of the potential, as well as the numerical values for all the parameters involved.

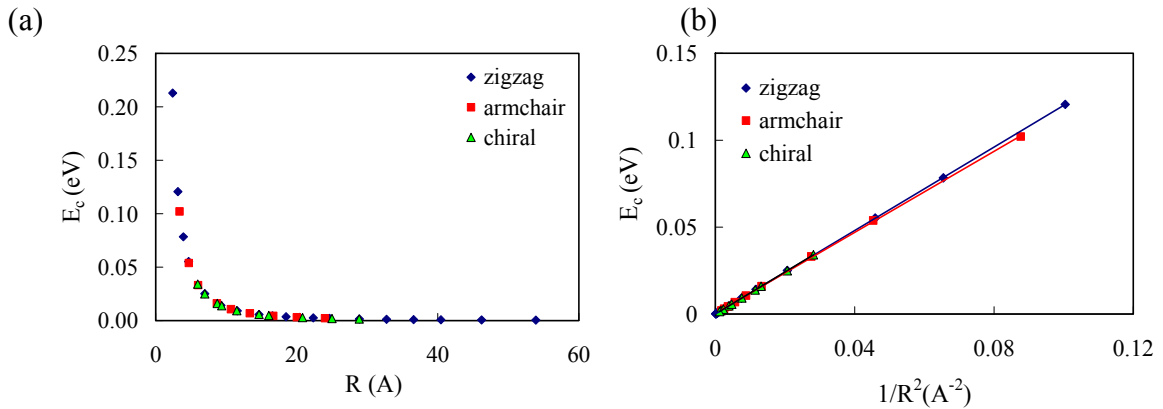
The AIREBO potential was tested for its quantitative accuracy through systematic comparisons with first-principles DFT calculations for the structure and properties of bulk crystalline carbon phases, carbon nanotubes, as well as for the chemisorption of H atoms onto CNTs. Some of the DFT results that were used in these comparisons were taken from the literature, while others were obtained by our own DFT calculations.

Table A.1 compares the AIREBO and DFT predictions for the lattice parameters and cohesive energies of crystalline carbon phases. The agreement is excellent in comparing overall structure, average bond lengths and bond angles, and energetic ordering (relative stability) of crystalline phases and it is very good in comparing lattice parameters, individual bond lengths and bond angles, and energy differences between crystalline phases.

**Table A.1.** Comparison between AIREBO and first-principles DFT predictions of the equilibrium lattice parameters and cohesive energies of the cubic-diamond, hexagonal-diamond (lonsdaleite), and graphite crystalline phases. The cohesive energy differences given in parentheses are expressed with respect to the cohesive energy of graphite. Comparisons of the lattice parameter predictions and predictions of the cohesive energy ordering (relative stability between phases) confirms good agreement between AIREBO and DFT in describing bulk crystalline carbon phases.

PHASE (Space Group)	Lattice parameter (Å)		Cohesive energy (eV)	
	DFT	AIREBO	DFT	AIREBO
Graphite (P6 <sub>3</sub> /mmc,194)	a = 2.46, c = 3.40	a = 2.425, c = 3.40	-9.05 (0.00)	-7.45 (0.00)
Diamond (Fd $\bar{3}$ m,227)	a = 3.57	a = 3.565	-8.92 (0.13)	-7.39 (0.06)
Lonsdaleite (P6 <sub>3</sub> /mmc,194)	a = 2.52, c = 4.12	a = 2.52, c = 4.11	-8.89 (0.16)	-7.24 (0.21)

As discussed in Chapter 1, carbon nanotubes can be viewed as rolled-up graphene sheets; consequently, compared to graphene planes, CNTs are under an additional strain due to the curvature of their surface. The curvature energy,  $E_c$ , can then be defined as the difference in the total energy per carbon atom between a pristine CNT and a graphene plane.  $E_c$  was calculated for nanotubes of different diameters and chiralities using the AIREBO potential and MD-based structural relaxation; the results are shown in figure A.1.



**Figure A.1.** (a) Curvature energy as function of (a) CNT radius  $R$  and (b)  $1/R^2$ .

The curvature energies plotted in Figure A.1 depend on the radius  $R$  of the CNTs according to the equation  $E_c = \alpha/R^2$ , in complete agreement with classical elasticity theory (Gulseren et al., 2002b). By plotting the AIREBO computed  $E_c$  values versus  $1/R^2$ , perfect linear fits are obtained for the data, as displayed in Figure A.1(b). For zigzag, armchair, and chiral CNTs, the linear regression analysis gives  $\alpha = 1.200 \text{ eV \AA}^2/\text{atom}$ ,  $1.165 \text{ eV \AA}^2/\text{atom}$ , and  $1.210 \text{ eV \AA}^2/\text{atom}$ , respectively. These AIREBO results can be compared with the DFT results obtained by Gulseren and co-workers (Gulseren et al., 2002a). They found the same linear dependency of  $E_c$  on  $1/R^2$ , with a coefficient  $\alpha = 2.14 \text{ eV \AA}^2/\text{atom}$  for zigzag nanotubes; Figure A.2 shows a comparison between our AIREBO predictions and these DFT results. The results are in excellent qualitative agreement and fairly quantitative agreement. The results of Figure A.1(a) also suggest that curvature-induced strain effects are present in pristine CNTs with a radii up to approximately 2 nm.

AIREBO predictions for the structure and energies of hydrogenated CNTs also were compared with our own DFT calculations and DFT results from the literature (Gulseren et al., 2001, 2002b; Yildirim et al., 2001; Barnard et al., 2005). Figure A.3. presents a visual comparison between the structures of a (6,6) CNT with three H atoms chemisorbed onto the surface, as obtained by structural relaxation according to AIREBO and DFT calculations (Barnard et al., 2005). The predicted structures are practically identical; after adsorbing a H atom, the initially  $sp^2$  carbon atoms on the nanotube structure assume a tetrahedral geometry characteristic of  $sp^3$  hybridization as predicted by DFT. A slight deformation of the circular section of the CNT upon chemisorption also is observed in both cases.

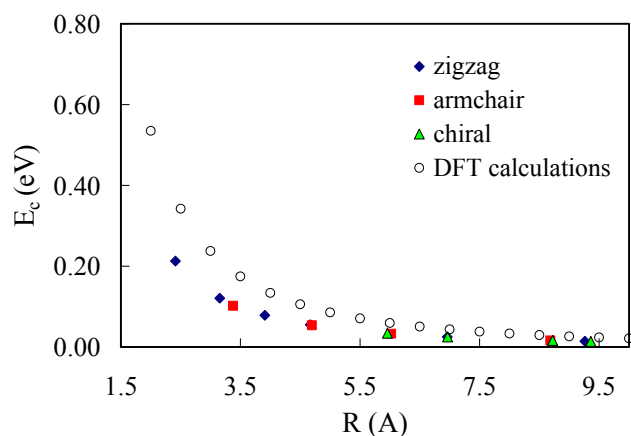


**Figure A.2.** Curvature energy as function of CNT radius  $R$ . Comparison between AIREBO predictions with DFT results for zigzag nanotubes (Gulseren et al., 2002a).

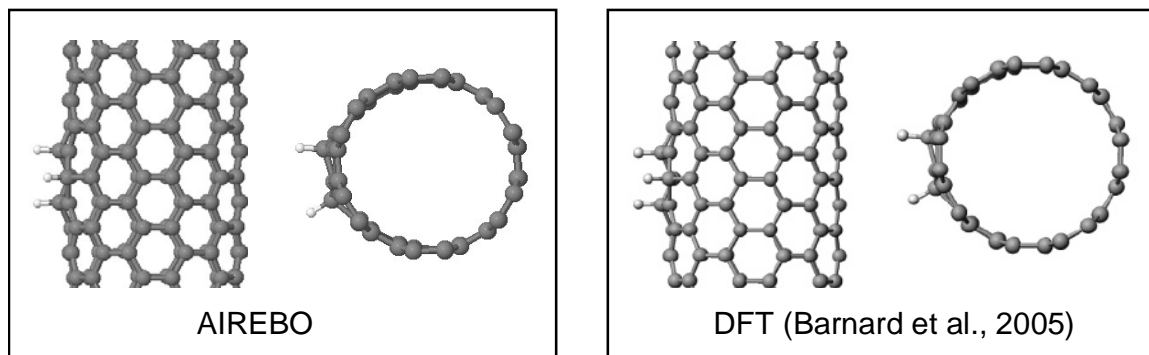


**Figure A.3.** Relaxed structures for a (6,6) CNT with three H atoms chemisorbed onto the CNT surface, obtained by AIREBO and DFT calculations (Barnard et al., 2005).

A detailed quantitative comparison between the AIREBO and DFT predictions for these structures and similar others has been made, in terms of the average bond lengths and bond angles. The results for (6,6) and (9,0) nanotubes with one, two and three chemisorbed H atoms onto the CNT walls, reported by Barnard and co-workers (Barnard et al., 2005) have been used in the comparison. A summary of the results is presented in Table A.2.

**Table A.2.** Average bond lengths and bond angles predicted by AIREBO and DFT calculations for (6,6) and (9,0) SWCNTs with different numbers of adsorbed H atoms onto the nanotube wall.

system	AIREBO	DFT	AIREBO	DFT	AIREBO	DFT
	C-C bond (Å)	C-C bond (Å)	C-H bond (Å)	C-H bond (Å)	angle (deg)	angle (deg)
(6,6) +1 H	1.53	1.51	1.09	1.11	108.9	111.6
(6,6) +2 H	1.53	1.50	1.09	1.11	109.0	112.1
(6,6) +3 H (r)	1.53	1.50	1.09	1.12	109.3	111.2
(6,6) +3 H (p)	1.53 - 1.52	1.49	1.09	1.12	109.2	112.1
(9,0) +1 H	1.54	1.51	1.09	1.11	108.9	111.7
(9,0) +2 H	1.53 - 1.54	1.50	1.09	1.12	109.0	112.5
(9,0) +3 H (r)	1.53 - 1.54	1.50	1.09	1.12	109.2	110.9
(9,0) +3 H (p)	1.53	1.50	1.09	1.12	109.1	110.7

The analysis of these results shows that the AIREBO potential gives a good description of the local changes in the structure of CNTs induced by hydrogen chemisorption. The agreement in the prediction of bond lengths and angles is not perfect; however, all the trends observed for the dependence of structural parameters on the number of atoms chemisorbed and on the nanotube chirality are the same for both the AIREBO and DFT predictions.

The binding energy,  $E_b$ , for the chemisorption of a single H atom also was calculated by the AIREBO potential for nanotubes of different diameters and chiralities, and the results are presented in Figure A.4. The binding energy is defined as

$$E_b = \frac{1}{N} (E_{CNT} + N \cdot E_H - E_{CNTH}), \quad (\text{A.2})$$

where  $E_{CNT}$  is the energy of the pristine nanotube,  $E_H$  is the energy of a single H atom (free and isolated) and  $E_{CNTH}$  is the energy of the CNT with  $N$  hydrogen atoms adsorbed onto its surface.

Figure A.4 shows that the predicted binding energy decreases with an increase in the diameter of the nanotube; the same behavior was reported by DFT calculations (Gulseren et al., 2001). This is an effect of the curvature of the CNTs; according to the

AIREBO results, this effect is present in CNTs with a radius up to approximately 8 nm, where  $E_b$  reaches practically the same level with that of H chemisorption onto a planar graphene sheet (depicted as the horizontal blue line in Figure A.4). A quantitative comparison for the prediction of this parameter has been made for CNTs of small diameters and the results are shown in Figure A.5. Again, the AIREBO predictions have captured the same trends exhibited by the DFT results. However, there are quantitative differences between the two types of predictions.

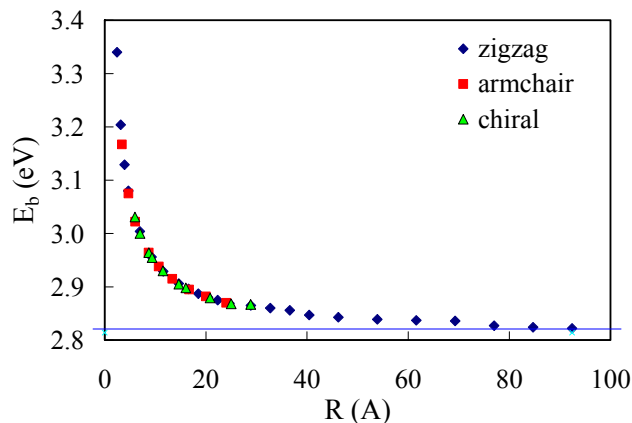


**Figure A.4.** Dependence on CNT radius,  $R$ , of the binding energies for the chemisorption of a single H atom onto the outer surface of SWCNTs of various diameters, as predicted by the AIREBO potential. The blue line marks the limit  $R \rightarrow \infty$ , corresponding to a planar graphene sheet.

Comparisons also were made in the predictions for hydrogenated CNTs at higher surface coverages. Two cases were considered, for surface coverage of 50% (regularly distributed H atoms), and 100%. The AIREBO results for the corresponding binding energies, Eq. (A2), are plotted as a function of the CNT radius in Figures A.6 and A.7, respectively. They exhibit the same trends observed in the DFT calculations (Yildirim et al., 2001; Gulseren et al., 2002b). Consistently with the DFT results, the AIREBO

predictions show that the binding energies for fully hydrogenated CNTs (100% of coverage) are higher than those for CNTs with regularly distributed chemisorbed H atoms at a coverage of 50%.

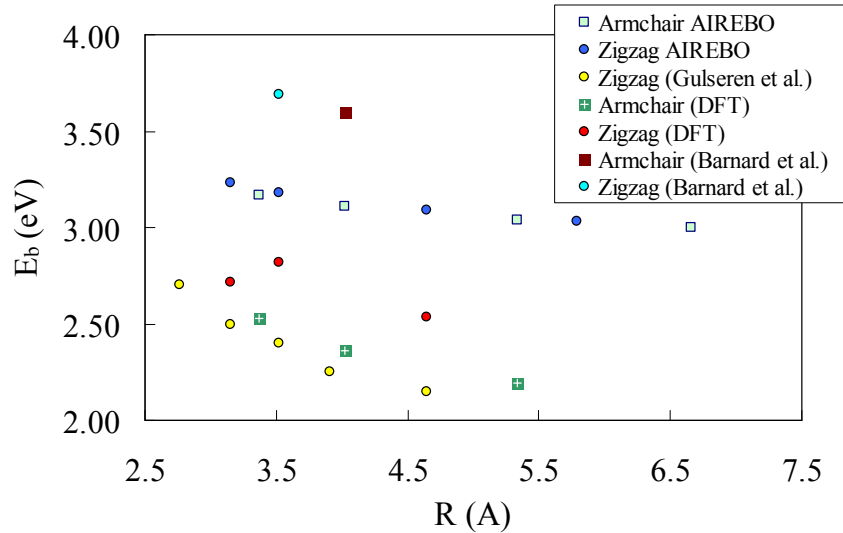


**Figure A.5.** Dependence on CNT radius,  $R$ , of binding energies for the chemisorption of a single H atom onto the outer surface of SWCNTs of various diameters. Comparison of AIREBO predictions with our DFT results and DFT results from the literature (Barnard et al., 2005; Gulseren et al., 2001).

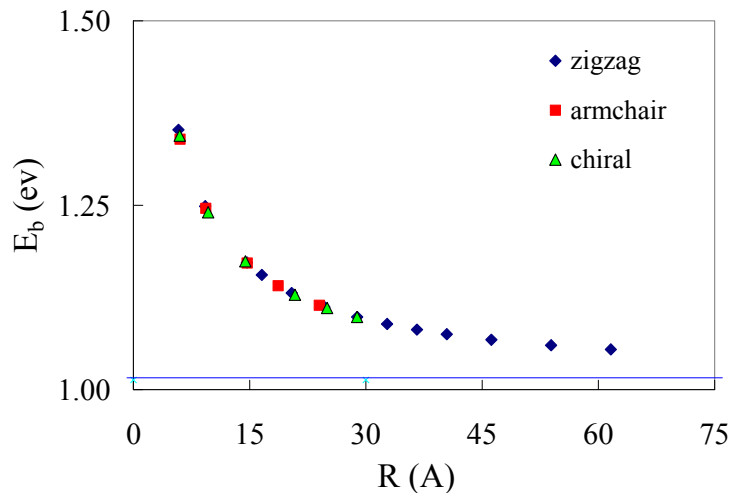


**Figure A.6.** Dependence on CNT radius,  $R$ , of binding energies for chemisorption of H atoms onto the surface of SWCNTs of different diameters and chiralities at a uniform coverage of 50%. The blue line marks the  $R \rightarrow \infty$  limit, corresponding to a planar graphene sheet.

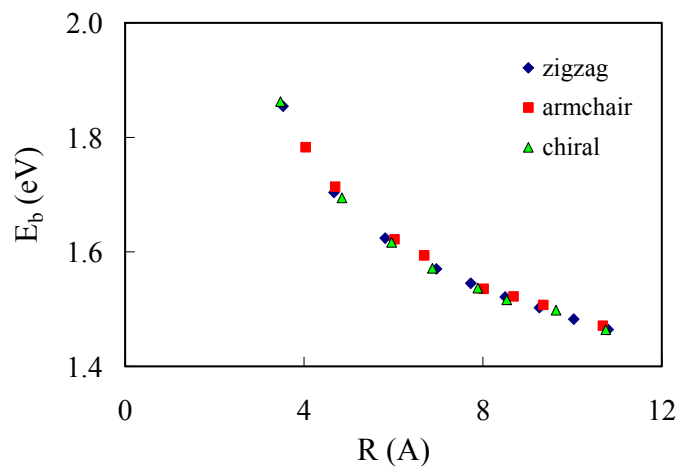


**Figure A.7.** Dependence on CNT radius,  $R$ , of binding energies for chemisorption of H atoms onto the surface of SWCNTs of different diameters and chiralities at a coverage of 100%.

Finally, we compare with DFT results, the AIREBO predictions for the radial strain in CNTs due to their hydrogenation, as discussed in Chapter 3 of the thesis. The comparisons for fully hydrogenated zigzag and armchair nanotubes of small diameters are shown in Fig A.8. The AIREBO predictions are in very good agreement with the DFT results: zigzag nanotubes exhibit a higher radial strain than the armchair ones in both cases. Also, both AIREBO and DFT predict a maximum in the radial strain for both zigzag and armchair CNTs at a diameter of  $\sim 0.9$  nm.

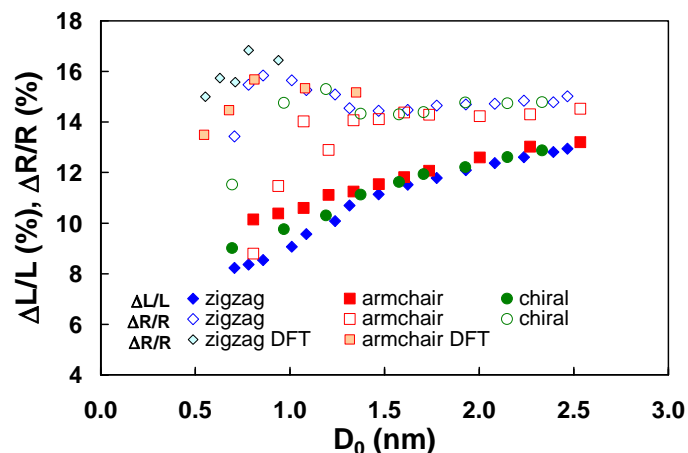


**Figure A.8.** Axial and radial strains resulting from chemisorption of H atoms onto SWCNTs of different diameters and chiralities at a surface coverage of 100%, as obtained by AIREBO-based relaxation simulations (see Chapter 3). Results from DFT calculations (Yildirim et al., 2001) also are included, and denoted by light-filled symbols.

In summary, the results and comparisons presented in this Appendix, show that the AIREBO predictions for the structure of pristine and hydrogenated CNTs and bulk crystalline carbon phases are in excellent qualitative agreement and in very good quantitative agreement with DFT calculations. Nevertheless, further validation is needed regarding the use of AIREBO in dynamical simulations involving the formation and dissociation of covalent bonds, in order to assess the potential's predictive capability of the corresponding activation energy barriers.

## BIBLIOGRAPHY

- M. P. Allen and D. J. Tildesley. *Computer simulation of liquids*. Clarendon Press, New York, NY, USA, 1989.
- M. J. Allen, V. C. Tung, and R. B. Kaner. Honeycomb Carbon: A Review of Graphene. *Chemical Reviews*, 110:132–145, 2010.
- A. Allouche, Y. Ferro, T. Angot, C. Thomas, and J.-M. Layet. Hydrogen adsorption on graphite (0001) surface: A combined spectroscopy–density-functional-theory study. *Journal of Chemical Physics*, 123:124701, 2005.
- A. Allouche, A. Jelea, F. Marinelli, and Y. Ferro. Hydrogenation and dehydrogenation of graphite (0001) surface: a density functional theory study. *Physica Scripta*, T124:91-95, 2006.
- A. Andree, M. L. Lay, T. Zecho, and J. Küpper. Pair formation and clustering of D on the basal plane of graphite, *Chemical Physics Letters*, 425:99-104, 2006.
- J. C. Angus and C. C. Hayman. Low-Pressure, Metastable Growth of Diamond and "Diamondlike" Phases. *Science*, 241:913-921, 1988.
- M. Aoki and H. Amawashi. Dependence of band structures on stacking and field in layered graphene. *Solid State Communications*, 142:123–127, 2007.
- P. Avouris, Z. Chen and V. Perebeinos. Carbon-based electronics. *Nature Nanotechnology*, 2:605-615, 2007.
- P. Badziag, W. S. Veowoerd, W. P. Ellis, and N. R. Greiner. Nanometre-sized diamonds are more stable than graphite. *Nature*, 343:244-245, 1990.
- A. A. Balandin, S. Ghosh, W. Bao, I. Calizo, D. Teweldebrhan, F. Miao, and C. N. Lau. Superior Thermal Conductivity of Single-Layer Graphene. *Nano Letters*, 8(3):902-907, 2008.
- R. Balog, B. Jørgensen, J. Wells, E. Lægsgaard, P. Hoffmann, F. Besenbacher, and L. Hornekær. Atomic Hydrogen Adsorbate Structures on Graphene. *Journal of the American Chemical Society*, 131(25):8744-8745, 2009.
- R. Balog, B. Jørgensen, L. Nilsson, M. Andersen, E. Rienks, M. Bianchi, M. Fanetti, E. Lægsgaard, A. Baraldi, S. Lizzit, Z. Sljivancanin, F. Besenbacher, B. Hammer, T. G. Pedersen, P. Hofmann, and L. Hornekær. Bandgap opening in graphene induced by patterned hydrogen adsorption. *Nature Materials*, 9, 315-319, 2010.
- F. Banhart and P. M. Ajayan. Carbon onions as nanoscopic pressure cells for diamond formation. *Nature*, 382:433-435, 1996.

- A. S. Barnard, S. P. Russo, and I. K. Snook. Size dependent phase stability of carbon nanoparticles: Nanodiamond versus fullerenes. *Journal of Chemical Physics*, 118(11):5094-5097, 2003.
- A. S. Barnard, S. P. Russo, and I. K. Snook. Ab Initio Modeling of Diamond Nanowire Structures. *Nano Letters*, 3(10):1323-1328, 2003.
- A. S. Barnard and I. K. Snook. Phase stability of nanocarbon in one dimension: Nanotubes versus diamond nanowires. *Journal of Chemical Physics*, 120(8):3817-3821, 2004.
- A. S. Barnard, M. L. Terranova, and M. Rossi. Density Functional Study of H-Induced Defects as Nucleation Sites in Hybrid Carbon Nanomaterials. *Chemistry of Materials*, 17:527-535, 2005.
- C. W. Bauschlicher, Jr. Hydrogen and fluorine binding to the sidewalls of a (10,0) carbon nanotube. *Chemical Physics Letters*, 322:237-241, 2000.
- C. W. Bauschlicher. High coverages of hydrogen on a (10,0) carbon nanotube. *Nano Letters*, 1(5):223-226, 2001.
- C. W. Bauschlicher and C. R. So. High Coverages of Hydrogen on (10,0), (9,0) and (5,5) Carbon Nanotubes. *Nano Letters*, 2(4):337-341, 2002.
- M. J. Behr and E. S. Aydil. Private communication. University of Minnesota, 2009.
- H. J. C. Berendsen, J. P. M. Postma, W. F. van Gunsteren, A. DiNola, and J. R. Haak. Molecular dynamics with coupling to an external bath. *Journal of Chemical Physics*, 81:3684-3690, 1984.
- D. S. Bethune, C. H. Klang, M. S. de Vries, G. Gorman, R. Savoy, J. Vazquez, and R. Beyers. Cobalt-catalysed growth of carbon nanotubes with single-atomic-layer walls. *Nature*, 363:605-607, 1993.
- D. W. Boukhvalov, M. I. Katsnelson, and A. I. Lichtenstein, Hydrogen on graphene: Electronic structure, total energy, structural distortions and magnetism from first-principles calculations. *Physical Review B*, 77:035427, 2008.
- D. W. Boukhvalov, and M. I. Katsnelson. Chemical functionalization of graphene. *Journal of Physics: Condensed Matter*, 21:344205, 2009.
- D. W. Boukhvalov and M. I. Katsnelson. Enhancement of Chemical Activity in Corrugated Graphene. *Journal of Physical Chemistry C*, 113:14176-14178, 2009.
- D.W. Brenner. Empirical potential for hydrocarbons for use in simulating the chemical vapor deposition of diamond films. *Physical Review B*, 42:9458-9471, 1990.

- D. W. Brenner, O. A. Shenderova, J. A. Harrison, S. J. Stuart, B. Ni, and S. B. Sinnott. A second-generation reactive empirical bond order (REBO) potential energy expression for hydrocarbons. *Journal of Physics: Condensed Matter*, 14:783–802, 2002.
- G. Buchs, A. V. Krasheninnikov, P. Ruffieux, P. Gröning, A. S. Foster, R. M. Nieminen, and O. Gröning. Creation of paired electron states in the gap of semiconducting carbon nanotubes by correlated hydrogen adsorption. *New Journal of Physics*, 9:275, 2007.
- G. Buchs, P. Ruffieux, P. Gröning, and O. Gröning. Scanning tunneling microscopy investigations of hydrogen plasma-induced electron scattering centers on single-walled carbon nanotubes. *Applied Physics Letters*, 90:013104, 2007.
- F. P. Bundy and J. S. Kasper. Hexagonal Diamond – A New Form of Carbon. *Journal of Chemical Physics*, 46(9):3437-3446, 1967.
- E. M. Byrne, M. A. McCarthy, Z. Xia, and W. A. Curtin. Multiwall Nanotubes Can Be Stronger than SingleWall Nanotubes and Implications for Nanocomposite Design. *Physical Review Letters*, 103:045502, 2009.
- J. M. Campanera, G. Savini, I. Suarez-Martinez, and M. I. Heggie. Density functional calculations on the intricacies of Moiré patterns on graphite. *Physical Review B*, 75:235449, 2007.
- R. Car and M. Parrinelo. Unified Approach for Molecular Dynamics and Density-Functional Theory. *Physical Review Letters*, 55:2471–2474, 1985.
- S. Casolo, O. M. Løvvik, R. Martinazzo, and G. F. Tantardini. Understanding adsorption of hydrogen atoms on graphene. *Journal of Chemical Physics*, 130:054704, 2009.
- S. Casolo, R. Martinazzo, and G. F. Tantardini. Band Engineering in Graphene with Superlattices of Substitutional Defects. *Journal of Physical Chemistry C*, 115(8):3250–3256, 2011.
- A. H. Castro Neto, F. Guinea, N. M. R. Peres, K. S. Novoselov and A. K. Geim. The electronic properties of graphene. *Reviews Of Modern Physics*, 81(1):109-162, 2009.
- D. Chandler. *Introduction to Modern Statistical Mechanics*. Oxford University Press, New York, 1987.
- K. Chang, S. Berber, and D. Tomanek. Transforming Carbon Nanotubes by Silylation: An Ab Initio Study. *Physical Review Letters*, 100:236102, 2008.
- S.-H. Cheng, K. Zou, F. Okino, H. R. Gutierrez, A. Gupta, N. Shen, P. C. Eklund, J. O. Sofo, and J. Zhu. Reversible fluorination of graphene: Evidence of a two-dimensional wide bandgap semiconductor. *Physical Review B*, 81:205435, 2010.

- L. A. Chernozatonskii, P. B. Sorokin, A. G. Kvashnin, and D. G. Kvashnin. Diamond-like C<sub>2</sub>H nanolayer, diamane: Simulation of the structure and properties. *JETP Letters*, 90(2):134-138, 2009.
- L. A. Chernozatonskii and P. B. Sorokin. Nanoengineering Structures on Graphene with Adsorbed Hydrogen “Lines”. *Journal of Physical Chemistry C*, 114:3225-3229, 2010.
- S. Ciraci, S. Dag, T. Yildirim, O. Gulseren, and R.T. Senger. Functionalized carbon nanotubes and device applications. *Journal of Physics: Condensed Matter*, 16:R901-R960, 2004.
- H. Cuppen and L. Hornekær. Kinetic Monte Carlo studies of hydrogen abstraction from graphite. *Journal of Chemical Physics*, 128:174707, 2008.
- H. Dai. Carbon nanotubes: opportunities and challenges. *Surface Science*, 500:218-241, 2002.
- A. C. Dillon, K. M. Jones, T. A. Bekkedahl, C. H. Kiang, D. S. Bethune, and M. J. Heben. Storage of hydrogen in single-walled carbon nanotubes. *Nature*, 386:377-379, 1997.
- M. S. Dresselhaus, G. Dresselhaus, and P. C. Eklund. *Science of Fullerenes and Carbon Nanotubes*. Academic Press, San Diego, CA, USA, 1996.
- M.S. Dresselhaus. Future Directions in Carbon Science. *Annual Review of Materials Science*, 27:1-34, 1997.
- M. S. Dresselhaus, G. Dresselhaus, and Ph. Avouris. *Carbon Nanotubes – Synthesis, Structure, properties, and Applications*. Springer-Verlag Berlin Heidelberg, Federal Republic of Germany, 2001.
- E. J. Duplock, M. Scheffler, and P. J. D. Lindan. Hallmark of Perfect Graphene. *Physical Review Letters*, 92:225502, 2004.
- D. C. Elias, R. R. Nair, T. M. G. Mohiuddin, S. V. Morozov, P. Blake, M. P. Halsall, A. C. Ferrari, D. W. Boukhvalov, M. I. Katsnelson, A. K. Geim, and K. S. Novoselov. Control of Graphene's Properties by Reversible Hydrogenation: Evidence for Graphane. *Science*, 323:610-613, 2009.
- S. Fahy, S.G. Louie, and M.L. Cohen. Pseudopotential total-energy study of the transition from rhombohedral graphite to diamond. *Physical Review B*, 34:1191-1199, 1986.
- S. Fahy and S.G. Louie. High-pressure structural and electronic properties of carbon. *Physical Review B*, 36, 3373-3385, 1987.

- Y. Ferro, F. Marinelli, and A. Allouche. Density functional theory investigation of H adsorption and H<sub>2</sub> recombination on the basal plane and in the bulk of graphite: Connection between slab and cluster model. *Journal of Chemical Physics*, 116(18):8124-8131, 2002.
- Y. Ferro, D. Teillet-Billy, N. Rougeau, V. Sidis, S. Morisset, and A. Allouche. Stability and magnetism of hydrogen dimers on graphene. *Physical Review B*, 78:085417, 2008.
- Y. Ferro, S. Morisset, and A. Allouche. Evidence of hydrogenated hexamers on graphite. *Chemical Physics Letters*, 478:42-44, 2009.
- D. Frenkel and B. Smit. *Understanding Molecular Simulation: From Algorithms to Applications (Computational Science Series, Vol 1)*, Academic Press, San Diego, CA, USA, 2002.
- C. Frondel and U. B. Marvin. Lonsdaleite, a hexagonal polymorph of diamond. *Nature*, 214:587-589, 1967.
- J. Furthmüller, J. Hafner, and G. Kresse. Ab initio calculation of the structural and electronic properties of carbon and boron nitride using ultrasoft pseudopotentials. *Physical Review B*, 50:15606-15622, 1994.
- J. M. García-Lastra Strong dependence of band-gap opening at the Dirac point of graphene upon hydrogen adsorption periodicity. *Physical Review B*, 82:235418, 2010.
- A. K. Geim and K. S. Novoselov. The rise of graphene. *Nature Materials*, 6:183-191, 2007.
- A. K. Geim. Graphene: Status and Prospects. *Science*, 324:1530-1534, 2009.
- P. Giannozzi, S. Baroni, N. Bonini, M. Calandra, R. Car, C. Cavazzoni, D. Ceresoli, G.L. Chiarotti, M. Cococcioni, I. Dabo, A. Dal Corso, S. de Gironcoli, S. Fabris, G. Fratesi, R. Gebauer, U. Gerstmann, C. Gougoussis, A. Kokalj, M. Lazzeri, L. Martin-Samos, N. Marzari, F. Mauri, R. Mazzarello, S. Paolini, A. Pasquarello, L. Paulatto, C. Sbraccia, S. Scandolo, G. Sclauzero, A. P. Seitsonen, A. Smogunov, P. Umari and R. M. Wentzcovitch. QUANTUM ESPRESSO: a modular and open-source software project for quantum simulations of materials. *Journal of Physics: Condensed Matter*, 21:395502, 2009.
- N. Grobert. Carbon nanotubes – becoming clean. *Materials Today*, 10:28-35, 2007.
- N. P. Guisinger, G. M. Rutter, J. N. Crain, P. N. First, and J. A. Stroscio. Exposure of epitaxial graphene on SiC(0001) to Atomic Hydrogen. *Nano Letters*, 9(4):1462-1466, 2009.
- O. Gülseren, T. Yildirim, and S. Ciraci. Tunable Adsorption on Carbon Nanotubes. *Physical Review Letters*, 87(11):116802, 2001.

- O. Gülseren, T. Yildirim, and S. Ciraci. Effects of hydrogen adsorption on single-wall carbon nanotubes: Metallic hydrogen decoration. *Physical Review B*, 66:121401, 2002.
- O. Gülseren, T. Yildirim, and S. Ciraci. Systematic ab initio study of curvature effects in carbon nanotubes. *Physical Review B*, 65:153405, 2002.
- R. E. Hanneman, H. M. Strong, and F. P. Bundy. Hexagonal Diamonds in Meteorites: Implications. *Science*, 155:995-997, 1967.
- A. Hashimoto, K. Suenaga, K. Urita, T. Shimada, T. Sugai, S. Bandow, H. Shinohara, and S. Iijima. Atomic correlation between adjacent graphene layers in double-wall carbon nanotubes. *Physical Review Letters*, 94:045504, 2005.
- J. Hass, R. Feng, J. E. Millán-Otoya, X. Li, M. Sprinkle, P. N. First, W. A. de Heer, E. H. Conrad, and C. Berger. Structural properties of the multilayer graphene/4H-SiC(000 $\bar{1}$ ) system as determined by surface x-ray diffraction. *Physical Review B*, 75:214109, 2007.
- J. Hass, F. Varchon, J. E. Millan-Otoya, M. Sprinkle, N. Sharma, W. A. de Heer, C. Berger, P. N. First, L. Magaud, and E. H. Conrad. Why Multilayer Graphene on 4H-SiC(000 $\bar{1}$ ) Behaves Like a Single Sheet of Graphene. *Physical Review Letters*, 100:125504, 2008.
- G. Henkelman, B. P. Uberuaga, and H. Jonsson. A climbing image nudged elastic band method for finding saddle points and minimum energy paths. *Journal of Chemical Physics*, 113(22):9901-9904, 2000.
- H. Hirai and K. Kondo. Modified Phases of Diamond Formed Under Shock Compression and Rapid Quenching. *Science*, 253:772-774, 1991.
- A. Hirsch and O. Vostrowsky. Functionalization of Carbon Nanotubes. *Topics in Current Chemistry*, 245:193-237, 2005.
- A. Hirsch. The era of carbon allotropes. *Nature Materials*, 9:868-871, 2010.
- P. Hohenberg and W. Kohn. Inhomogeneous Electron Gas. *Physical Review*, 136(3B), B864-B871, 1964.
- L. Hornekær, Ž. Šljivančanin, W. Xu, R. Otero, E. Rauls, I. Stensgaard, E. Lægsgaard, B. Hammer, and F. Besenbacher. Metastable Structures and Recombination Pathways for Atomic Hydrogen on the Graphite (0001) Surface. *Physical Review Letters*, 96:156104, 2006.
- L. Hornekær, E. Rauls, W. Xu, Ž. Šljivančanin, R. Otero, I. Steensgaard, E. Lægsgaard, B. Hammer, and F. Besenbacher. Clustering of Chemisorbed H(D) Atoms on the Graphite (0001) Surface due to Preferential Sticking. *Physical Review Letters*, 97:186102, 2006.

- L. Hornekær, W. Xu, R. Otero, E. Laegsgaard, and F. Besenbacher. Long range orientation of meta-stable atomic hydrogen adsorbate clusters on the graphite (0001) surface. *Chemical Physics Letters*, 446:237-242, 2007.
- N. M. Hwang, J. H. Hahn, and D. Y. Yoon. Chemical potential of carbon in the low pressure synthesis of diamond. *Journal of Crystal Growth*, 160:87-97, 1996.
- S. Iijima. Helical microtubules of graphitic carbon. *Nature*, 354:56-58, 1991.
- S. Iijima and T. Ichihashi. Single-shell carbon nanotubes of 1-nm diameter. *Nature*, 363:603-605, 1993.
- V. V. Ivanovskaya and A. L. Ivanovskii. Atomic Structure, Electronic Properties, and Thermal Stability of Diamond-like Nanowires and Nanotubes. *Inorganic Materials*, 43(4):349-357, 2007.
- A. Janotti, S.-H. Wei, and D.J. Singh. First-principles study of the stability of BN and C. *Physical Review B*, 64:174107, 2001.
- H.J.F. Jansen and A. J. Freeman. Structural and electronic properties of graphite via an all-electron total-energy local-density approach. *Physical Review B*, 35:8207-8214, 1987.
- L. Jeloica and V. Sidis. DFT investigation of the adsorption of atomic hydrogen on a cluster-model graphite surface. *Chemical Physics Letters*, 300:157-162, 1999.
- Q. Jiang, J. C. Li, and G. Wilde. The size dependence of the diamond-graphite transition. *Journal of Physics: Condensed Matter*, 12:5623-5627, 2000.
- H. Jonsson, G. Mills, and K. W. Jacobsen. Nudged elastic band method for finding minimum energy paths of transitions. In *Classical and Quantum Dynamics in Condensed Phase Simulations*, B. J. Berne, G. Ciccotti, and D. F. Coker, World Scientific, Singapore, 1998.
- V.I Kasatochkin, V.V Korshak, Yu.P Kudryavtsev, A.M Sladkov and I.E Sterenberg. On crystalline structure of carbene. *Carbon*, 11(1):70-72, 1973.
- J. Kerwin and B. Jackson. The sticking of H and D atoms on a graphite (0001) surface: The effects of coverage and energy dissipation. *Journal of Chemical Physics*, 128:084702, 2008.
- B. N. Khare, M. Meyyappan, A. M. Cassell, C. V. Nguyen, and J. Han. Functionalization of carbon nanotubes using atomic hydrogen from a glow discharge. *Nano Letters*, 2(1):73-77, 2002.
- B. N. Khare, M. Meyyappan, J. Kralj, P. Wihite, M. Sisay, H. Imanaka, J. Koehne, and C. W. Baushchlicher, Jr. A glow-discharge approach for functionalization of carbon nanotubes. *Applied Physics Letters*, 81(27):5237-5239, 2002.

- M. Khazaei, M. S. Bahramy, A. Ranjbar, H. Mizuseki, and Y. Kawazoe. Geometrical indications of adsorbed hydrogen atoms on graphite producing star and ellipsoidal like features in scanning tunneling microscopy images: Ab initio study. *Carbon*, 47:3306-3312, 2009.
- E. Kim and C. Chen. Calculation of bulk modulus for highly anisotropic materials. *Physics Letters A*, 326:442-448, 2004.
- W. Koch and M. C. Holthausen. *A Chemist's Guide to Density Functional Theory*. Wiley-VCH Verlag GmbH, Weinheim, Federal Republic of Germany, 2001.
- W. Kohn and L. J. Sham. Self-Consistent Equations Including Exchange and Correlation Effects. *Physical Review*, 140(4A):A1133-A1138, 1965.
- W. Kohn. Nobel Lecture: Electronic structure of matter - wave functions and density functionals. *Reviews of Modern Physics*, 71(5):1253-1266, 1999.
- A. N. Kolmogorov and V. H. Crespi. Registry-dependent interlayer potential for graphitic systems. *Physical Review B*, 71:235415, 2005.
- A. V. Krasheninnikov and F. Banhart. Engineering of nanostructured carbon materials with electron or ion beams. *Nature Materials*, 6:723-733, 2007.
- G. Kresse and J. Furthmuller. Efficient iterative schemes for ab initio total-energy calculations using a plane-wave basis set. *Physical Review B*, 54(16):11169-11186, 1996.
- H. W. Kroto, J. R. Heath, S. C. O'Brien, R. F. Curl, and R. E. Smalley. C<sub>60</sub>: Buckminsterfullerene. *Nature*, 318:162-163, 1985.
- A. V. Kurdyumov, V. F. Britun, V. B. Zelyavskii, A. I. Danilenko, N. I. Borimchuk, V. V. Yarosh, V. Yu. Kulikovskii, and A. A. Mikhailik. Structure of Intermediate Carbon Phase Formed Under Shock Compression of Ultradispersed Graphite Materials. *Powder Metallurgy and Metal Ceramics*, 45(1-2):86-92, 2006.
- M. Kuwabara, D. R. Clarke, and D. A. Smith. Anomalous superperiodicity in scanning tunneling microscope images of graphite. *Applied Physics Letters*, 56(24):2396-2398, 1990.
- N. Layadi, P. R. I. Cabarrocas, B. Drevillon, and I. Solomon. Real-time spectroscopic ellipsometry study of the growth of amorphous and microcrystalline silicon thin films prepared by alternating silicon deposition and hydrogen plasma treatment. *Physical Review B*, 52:5136-5143, 1995.
- W. R. L. Lambrecht, C. H. Lee, B. Segall, J. C. Angus, Z. D. Li, and M. Sunkara. Diamond nucleation by hydrogenation of the edges of graphitic precursors. *Nature*, 364:607-610, 1993.

- L. D. Landau. Zur Theorie der Phasenumwandlungen. II. *Phys. Z. Sowjetunion*, 11:26–35, 1937.
- S. Latil and L. Henrard. Charge Carriers in Few-Layer Graphene Films. *Physical Review Letters*, 97:036803, 2006.
- S. Latil, V. Meunier, and L. Henrard. Massless fermions in multilayer graphitic systems with misoriented layers: Ab initio calculations and experimental fingerprints. *Physical Review B*, 76:201402(R), 2007.
- A. R. Leach. *Molecular Modelling: Principles and Applications*. Second edition, Pearson Education Limited, England, 2001.
- C. Lee, X. Wei, J. W. Kysar, and J. Hone. Measurement of the Elastic Properties and Intrinsic Strength of Monolayer Graphene. *Science*, 321:385-388, 2008
- B. Lee, S. Han, and Y. Kim. First-principles study of preferential sites of hydrogen incorporated in epitaxial graphene on 6H-SiC(0001). *Physical Review B*, 81:075432, 2010.
- O. Leenaerts, B. Partoens, and F. M. Peeters. Hydrogenation of bilayer graphene and the formation of bilayer graphane from first principles. *Physical Review B*, 80:245422, 2009.
- Q. Li, Y. Ma, A. R. Oganov, H. Wang, H. Wang, Y. Xu, T. Cui, H.-K. Mao, and G. Zou. Superhard Monoclinic Polymorph of Carbon. *Physical Review Letters*, 102:175506, 2009.
- J. M. B. Lopes dos Santos, N. M. R. Peres, and A. H. Castro Neto. Graphene Bilayer with a Twist: Electronic Structure. *Physical Review Letters*, 99:256802, 2007.
- S. Luo, O. Tschauner, T. E. Tierney, D. C. Swift, S. J. Chipera, and P. D. Asimow. Novel crystalline carbon-cage structure synthesized from laser-driven shock wave loading of graphite. *Journal of Chemical Physics*, 123:024703, 2005.
- Z. Luo, T. Yu, K. Kim, Z. Ni, Y. You, S. Lim, Z. Shen, S. Wang, and J. Lin. Thickness-Dependent Reversible Hydrogenation of Graphene Layers. *ACS Nano*, 3(7):1781-1788, 2009.
- W. L. Mao, H. Mao, P. J. Eng, T. P. Trainor, M. Newville, C. Kao, D. L. Heinz, J. Shu, Y. Meng, and R. J. Hemley. Bonding Changes in Compressed Superhard Graphite. *Science*, 302:425-427, 2003.
- R. M. Martin. *Electronic Structure: Basic Theory and Practical Methods*. Cambridge University Press, Cambridge, UK, 2004.
- R. Martinazzo, S. Casolo, and G. F. Tantardini. Symmetry-induced band-gap opening in graphene superlattices. *Physical Review B*, 81:245420, 2010.

- N. Marzari, D. Vanderbilt, A. De Vita, and M. C. Payne. Thermal Contraction and Disorder of the Al(110) Surface. *Physical Review Letters*, 82(16):3296–3299, 1999.
- P. W. May. Diamond thin films: a 21st-century material. *Philosophical Transactions of the Royal Society A: Physical, Mathematical and Engineering Sciences*, 358:473–495, 2000.
- E. J. Mele. Commensuration and interlayer coherence in twisted bilayer graphene. *Physical Review B*, 81:161405(R), 2010.
- M. Menon, E. Richter, P. Raghavan, and K. Teranishi. Large-scale quantum mechanical simulations of carbon nanowires. *Superlattices and Microstructures*, 27(5/6):577–581, 2000.
- N. D. Mermin. Crystalline order in two dimensions. *Physical Review*, 176:250–254, 1968.
- N. Metropolis, A.W. Rosenbluth, M.N. Rosenbluth, A.H. Teller, and E. Teller. Equation of State Calculations by Fast Computing Machines. *Journal of Chemical Physics*, 21(6):1087–1092, 1953.
- M. Meyyappan, L. Delzeit, A. Cassell, and D. Hash. Carbon nanotube growth by PECVD: a review. *Plasma Sources Science and Technology*, 12:205–216, 2003.
- H. J. Monkhorst and J. D. Pack. Special points for Brillouin-zone integrations. *Physical Review B*, 13(12):5188–5192, 1976.
- A. R. Muniz, T. Singh, and D. Maroudas. Effects of Hydrogen Chemisorption on the Structure and Deformation of Single-walled Carbon Nanotubes. *Applied Physics Letters*, 94:103108, 2009.
- A. R. Muniz, M. Meyyappan, and D. Maroudas. On the Hydrogen Storage Capacity of Carbon Nanotube Bundles. *Applied Physics Letters*, 95:163111, 2009.
- A. R. Muniz, T. Singh, E. S. Aydil, and D. Maroudas. Analysis of Diamond Nanocrystal Formation from Multiwalled Carbon Nanotubes. *Physical Review B*, 80:144105, 2009.
- A. R. Muniz and D. Maroudas. Hydrogenation effects on the structure and morphology of graphene and single-walled carbon nanotubes. *Journal of Applied Physics*, 108:113532, 2010.
- F. D. Murnaghan. The Compressibility of Media under Extreme Pressures. *Proceedings of the National Academy of Sciences of the USA*, 30(9):244–247, 1944.

- R. R. Nair, W. Ren, R. Jalil, I. Riaz, V. G. Kravets, L. Britnell, P. Blake, F. Schedin, A. S. Mayorov, S. Yuan, M. I. Katsnelson, H.-M. Cheng, W. Strupinski, L. G. Bulusheva, A. V. Okotrub, I. V. Grigorieva, A. N. Grigorenko, K. S. Novoselov, and A. K. Geim. Fluorographene: A Two-Dimensional Counterpart of Teflon. *Small*, 6(24):2877-2884, 2010.
- A. Nikitin, H. Ogasawara, D. Mann, R. Denecke, Z. Zhang, H. Dai, K. Cho, and A. Nilsson. Hydrogenation of single-walled carbon nanotubes. *Physical Review Letters*, 95:225507, 2005.
- A. Nikitin, X. Li, Z. Zhang, H. Ogasawara, H. Dai, and A. Nilsson. Hydrogen storage in carbon nanotubes through the formation of stable C-H bonds. *Nano Letters*, 8(1):162-167, 2008.
- A. Nikitin, Z. Zhang, and A. Nilsson. Energetics of C-H Bonds Formed at Single-Walled Carbon Nanotubes. *Nano Letters*, 9(4):1301-1306, 2009.
- F. Nogueira, A. Castro, and M. A. L. Marques. *A Tutorial on Density Functional Theory*. In: C. Fiolhais, F. Nogueira, and M. Marques (Eds.), *A Primer in Density Functional Theory*, Springer-Verlag Berlin Heidelberg, Federal Republic of Germany, 2003.
- K. S. Novoselov, A. K. Geim, S. V. Morozov, D. Jiang, Y. Zhang, S. V. Dubonos, I. V. Grigorieva, and A. A. Firsov. Electric Field Effect in Atomically Thin Carbon Films. *Science*, 306: 666-669, 2004.
- K. S. Novoselov, D. Jiang, F. Schedin, T. J. Booth, V. V. Khotkevich, S. V. Morozov, and A. K. Geim. Two-dimensional atomic crystals. *Proceedings of the National Academy of Sciences of the USA*, 102(30):10451–10453, 2005
- M. C. Payne, M. P. Teter, D. C. Allan, T. A. Arias, and J. D. Joannopoulos. Iterative minimization techniques for *ab initio* total-energy calculations: molecular dynamics and conjugate gradients. *Reviews of Modern Physics*, 64:1045-1097, 1992.
- K. A. Park, K. Seo, and Y. H. Lee. Adsorption of atomic hydrogen on single-walled carbon nanotubes. *Journal of Physical Chemistry B*, 109(18):8967-8972, 2005.
- Q. X. Pei, Y. W. Zhang, and V. B. Shenoy. A molecular dynamics study of the mechanical properties of hydrogen functionalized graphene. *Carbon*, 48:898-904, 2010.
- R. E. Peierls. Quelques proprietes typiques des corps solides. *Ann. I. H. Poincare*, 5:177–222, 1935.
- B. Peng, M. Locascio, P. Zapol, S. Y. Li, S. L. Mielke, G. C. Schatz, and H. D. Espinosa. Measurements of near-ultimate strength for multiwalled carbon nanotubes and irradiation-induced crosslinking improvements. *Nature Nanotechnology*. 3(10):626-631, 2008.

- J. Perdew and A. Zunger. Self-interaction correction to density-functional approximations for many-electron systems. *Physical Review B*, 23(10):5048-5079, 1981.
- J. P. Perdew, K. Burke, and M. Ernzerhof. Generalized Gradient Approximation Made Simple. *Physical Review Letters*, 77(18):3865-3868, 1996.
- R. Petersen, T. G. Pedersen, and A.-P. Jauho. Clar Sextet Analysis of Triangular, Rectangular, and Honeycomb Graphene Antidot Lattices. *ACS Nano*, 5(1):523-529, 2011.
- W.-T. Pong and C. Durkan. A review and outlook for an anomaly of scanning tunnelling microscopy (STM): superlattices on graphite. *Journal of Physics D: Applied Physics*, 38:R329-R355, 2005.
- D. C. Rapaport. *The Art of Molecular Dynamics Simulation*, Cambridge University Press, Cambridge, UK, 2004.
- F. J. Ribeiro, P. Tangney, S. G. Louie, and M. L. Cohen. Structural and electronic properties of carbon in hybrid diamond-graphite structures. *Physical Review B*, 72:214109, 2005.
- T. Roman, W. A. Dino, H. Nakanishi, H. Kasai, T. Sugimoto, and K. Tange. Hydrogen pairing on graphene. *Carbon*, 45:218-220, 2007.
- T. Roman, W. A. Dino, H. Nakanishi, and H. Kasai. High-uptake graphene hydrogenation: a computational perspective. *Journal of Physics: Condensed Matter*, 21:474219, 2009.
- T. Roman, H. Nakanishi, H. Kasai, K. Nobuhara, T. Sugimoto, and K. Tange. Stability of Three-Hydrogen Clusters on Graphene. *Journal of the Physical Society of Japan*, 78:035002, 2009.
- Z. Y. Rong and P. Kuiper. Electronic effects in scanning tunneling microscopy: Moire pattern on a graphite surface. *Physical Review B*, 48(23):17427-17431, 1993.
- N. Rougeau, D. Teillet-Billy, and V. Sidis. Double H atom adsorption on a cluster model of a graphite surface. *Chemical Physics Letters*, 431:135-138, 2006.
- P. Ruffieux, O. Gröning, M. Biemann, P. Mauron, L. Schlapbach, and P. Gröning. Hydrogen adsorption on  $sp^2$ -bonded carbon: Influence of the local curvature. *Physical Review B*, 66:245416, 2002.
- P. Ruffieux, O. Gröning, M. Biemann, and P. Gröning. Hydrogen chemisorption on  $sp^2$ -bonded carbon: Influence of the local curvature and local curvature effects. *Applied Physics A – Materials Science & Processing*, 78:975-980, 2004.

- S. Ryu, M. Y. Han, J. Maultzsch, T. F. Heinz, P. Kim, M. L. Steigerwald, and L. E. Brus. Reversible basal plane hydrogenation of graphene. *Nano Letters*, 8(12):4597-4602, 2008.
- S. Scandolo, M. Bernasconi, G. L. Chiarotti, P. Focher, and E. Tosatti. Pressure-Induced Transformation Path of Graphite to Diamond. *Physical Review Letters*, 74:4015-4018, 1995.
- P. A. Schultz, K. Leung, and E. B. Stechel. Small rings and amorphous tetrahedral carbon. *Physical Review B*, 59(2):733-741, 1999.
- F. Schwier. Graphene transistors. *Nature Nanotechnology*, 5:487-496, 2010.
- P. Sessi, J. R. Guest, M. Bode, and N. P. Guisinger. Patterning Graphene at the Nanometer Scale via Hydrogen Desorption. *Nano Letters*, 9(12):4343-4347, 2009.
- X. Sha and B. Jackson. First-principles study of the structural and energetic properties of H atoms on a graphite (0001) surface. *Surface Science*, 496:318-330, 2002.
- X. Sha, B. Jackson, and D. Lemoine. Quantum studies of Eley-Rideal reactions between H atoms on a graphite surface. *Journal of Chemical Physics*, 116(16):7158-7169, 2002.
- S. Shallcross, S. Sharma, and O. A. Pankratov. Quantum interference at the twist boundary in graphene. *Physical Review Letters*, 101:056803, 2008.
- S. Shallcross, S. Sharma, and O. A. Pankratov. Twist boundary in graphene: energetics and electric field effect. *Journal of Physics: Condensed Matter*, 20:454224, 2008.
- S. Shallcross, S. Sharma, E. Kandelaki, and O. A. Pankratov. Electronic structure of turbostratic graphene. *Physical Review B*, 81:165105, 2010.
- O. Shenderova, D. Brenner, and R. S. Ruoff. Would Diamond Nanorods Be Stronger than Fullerene Nanotubes? *Nano Letters*, 3(6):805-809, 2003.
- Ž. Šljivančanin, E. Rauls, L. Hornekær, W. Xu, F. Besenbacher, and B. Hammer. Extended atomic hydrogen dimer configurations on the graphite (0001) surface. *Journal of Chemical Physics*, 131:084706, 2009.
- J. O. Sofo, A. S. Chaudhari, and G. D. Barber. Graphane: A two-dimensional hydrocarbon. *Physical Review B*, 75:153401, 2007.
- M. Sprinkle, D. Siegel, Y. Hu, J. Hicks, A. Tejada, A. Taleb-Ibrahimi, P. Le Fevre, F. Bertran, S. Vizzini, H. Enriquez, S. Chiang, P. Soukiassian, C. Berger, W. A. de Heer, A. Lanzara, and E. H. Conrad. First Direct Observation of a Nearly Ideal Graphene Band Structure. *Physical Review Letters*, 103:226803, 2009.
- S. Sriraman, S. Agarwal, E. S. Aydil, and D. Maroudas. Mechanism of hydrogen-induced crystallization of amorphous silicon. *Nature*, 418:62-65, 2002.

- V. N. Staroverov, G. E. Scuseria, J. Tao, and J. P. Perdew. Tests of a ladder of density functionals for bulk solids and surfaces. *Physical Review B*, 69:075102, 2004.
- S.J. Stuart, A. B. Tutein, and J. A. Harrison. A reactive potential for hydrocarbons with intermolecular interactions. *Journal of Chemical Physics*, 112:6472-6486, 2000.
- L. T. Sun, J. L. Gong, Z. Y. Zhu, D. Z. Zhu, S. X. He, Z. X. Wang, Y. Chen, and G. Hu. Nanocrystalline diamond from carbon nanotubes. *Applied Physics Letters*, 84(15):2901-2903, 2004.
- L. Sun, J. Gong, Z. Zhu, D. Zhu, and S. He. Diamond Nanorods from Carbon Nanotubes. *Advanced Materials*, 16(20):1849-1853, 2004.
- R. H. Telling, C. P. Ewels, A. A. El-Barbary, and M. I. Heggie. Wigner defects bridge the graphite gap. *Nature Materials*, 2:333-337, 2003.
- J. Tersoff. New empirical approach for the structure and energy of covalent systems. *Physical Review B*, 37:6991-7000, 1988.
- A. Tokura, F. Maeda, Y. Teraoka, A. Yoshigoe, D. Takagi, Y. Homma, Y. Watanabe, and Y. Kobayashi. Hydrogen adsorption on single-walled carbon nanotubes studied by core-level photoelectron spectroscopy and Raman spectroscopy. *Carbon*, 46:1903-1908, 2008.
- K. Umemoto, R. M. Wentzcovitch, S. Saito, and T. Miyake. Body-Centered Tetragonal C<sub>4</sub>: A Viable sp<sup>3</sup> Carbon Allotrope. *Physical Review Letters*, 104:125504, 2010.
- D. Vanderbilt. Soft self-consistent pseudopotentials in a generalized eigenvalue formalism. *Physical Review B*, 41(11):7892-7895, 1990.
- R. Van Noorden. The trials of new carbon. *Nature*, 469:14-16, 2011.
- F. Varchon, P. Mallet, L. Magaud, and J.-Y. Veuillen. Rotational disorder in few-layer graphene films on 6H-SiC(000 $\bar{1}$ ): A scanning tunneling microscopy study. *Physical Review B*, 77:165415, 2008.
- M. Volpe and F. Cleri. Chemisorption of atomic hydrogen in graphite and carbon nanotubes, *Surface Science*, 544:24-34, 2003.
- H. Vora and T. J. Moravec. Structural investigation of thin films of diamondlike carbon. *Journal of Applied Physics*, 52(10):6151-6157, 1981.
- Z. Waqar, E. A. Denisov, T. N. Kompaniets, I. V. Makarenko, and A. N. Titkov. Modification of Graphite Surface in the Course of Atomic Hydrogen Sorption STM and AFM Study. *Physica Scripta*, T94:132-136, 2001.

- J. H. Warner, M. H. Rummeli, T. Gemming, B. Buchner, and G. Andrew D. Briggs. Direct Imaging of Rotational Stacking Faults in Few Layer Graphene. *Nano Letters*, 9(1):102-106, 2009.
- B. Wen, J. J. Zhao, T. J. Li, C. Dong, and J. Z. Jin. n-diamond from catalysed carbon nanotubes: synthesis and crystal structure. *Journal of Physics: Condensed Matter*, 17(48): L513-L519, 2005.
- A. G. Whittaker, E. J. Watts, R. S. Lewis, and E. Anders. Carbynes: Carriers of Primordial Noble Gases in Meteorites. *Science*, 209:1512-1514, 1980.
- M. Wu, X. Wu, Y. Gao, and X. C. Zeng. Patterned Hydrogenation of Graphene: Magnetic Quantum Dot Array. *Journal of Physical Chemistry C*, 114:139-142, 2010.
- J. Xhie, K. Sattler, M. Ge, and N. Venkateswaran. Giant and supergiant lattices on graphite. *Physical Review B*, 47(23):15835-15841, 1993.
- Y. Xu, X. Li and J. Dong. Infrared and Raman spectra of AA-stacking bilayer graphene. *Nanotechnology*, 21: 065711, 2010.
- T. Yagi, W. Utsumi, M. A. Yamakata, T. Kikegawa, and O. Shimomura. High-pressure in situ x-ray-diffraction study of the phase transformation from graphite to hexagonal diamond at room temperature. *Physical Review B*, 46:6031-6039, 1992.
- Q. Yang, S. Yang, C. Xiao, and A. Hirose. Transformation of carbon nanotubes to diamond in microwave hydrogen plasma. *Materials Letters*, 61:2208-2211, 2007.
- T. Yildirim, O. Gulseren, and S. Ciraci. Exohydrogenated single-wall carbon nanotubes. *Physical Review B*, 64:075404, 2001.
- M.T. Yin and M.L. Cohen. Structural theory of graphite and graphitic silicon. *Physical Review B*, 29:6996-6998, 1984.
- M. T. Yin. Si-III (BC-8) crystal phase of Si and C: Structural properties, phase stabilities, and phase transitions. *Physical Review B*, 30:1773-1776, 1984.
- Y. Yürüm, A. Taralp, and T. N. Veziroglu. Storage of hydrogen in nanostructured carbon materials. *International Journal of Hydrogen Energy*, 34:3784-3798, 2009.
- H. Yusa. Nanocrystalline diamond directly transformed from carbon nanotubes under high pressure. *Diamond and Related Materials*, 11:87-91, 2002.
- T. Zecho, A. Güttler, X. Sha, B. Jackson, and J. Küppers. Adsorption of hydrogen and deuterium atoms on the (0001) graphite surface. *Journal of Chemical Physics*, 117(18):8486-8492, 2002.

- G. Zhang, P. Qi, X. Wang, Y. Lu, D. Mann, X. Li, and H. Dai. Hydrogenation and hydrocarbonation and etching of single-walled carbon nanotubes. *Journal of the American Chemical Society*, 128(18):6026-6027, 2006.
- G. Zheng, Q. Li, K. Jiang, X. Zhang, J. Chen, Z. Ren, and S. Fan. Transition of single-walled carbon nanotubes from metallic to semiconducting in field-effect transistors by hydrogen plasma treatment. *Nano Letters*, 7(6):1622-1625, 2007.
- Y. Zhu, S. Murali, W. Cai, X. Li, J. W. Suk, J. R. Potts, and R. S. Ruoff. Graphene and Graphene Oxide: Synthesis, Properties, and Applications. *Advanced Materials*, 22(35):3906-3924, 2010.